RADIO INTERFEROMETRIC INVESTIGATIONS OF SATURN'S RINGS AT 3.71- AND 1.30-CM WAVELENGTHS

Thesis by

Frederic Peter Schloerb

In Partial Fulfillment of the Requirements

For the Degree of

Doctor of Philosophy

California Institute of Technology

Pasadena, California

1978

(Submitted December 14, 1977)

to my wife, Holly,

and to the memory of our son, Michael

ACKNOWLEDGEMENTS

I am grateful to a number of people for their contributions to this thesis, and I am glad to have this opportunity to thank them.

Duane Muhleman, my thesis advisor, has supported me throughout my graduate career with his friendship and advice. My work on Saturn and the rings began at his suggestion, and I have been aided by his almost daily counsel considerably.

I have profited from Glenn Berge's advice and, in particular, his considerable understanding of radio interferometry. In addition, I wish to thank him for his careful reading of a preliminary manuscript of this thesis and many helpful suggestions.

The Hat Creek observations could not have been made without the full cooperation of the University of California, Berkeley. I appreciate being able to use the facility and wish to thank Jack Welch, Mel Wright, Rick Forster, and John Dreher for their help with the observations and data reduction.

At wavelengths as short as those used in this work, it is difficult to find calibrators which are not suspected to be variable. It was valuable, therefore, to use Bill Dent's observations of the Saturn calibrators to confirm my own, and I thank him for making them available to me.

I appreciate discussions about Saturn's rings and my results that I have had with a number of other persons. In particular, I wish to thank Jeff Cuzzi, Peter Goldreich, Bill Irvine, Mike Janssen,

Ed Olsen, and Jim Pollack for their interest in my work and contributions to my understanding of Saturn's rings.

The observations made at the Hat Creek and Owens Valley observatories would not have gotten very far if it were not for the observatories' staffs. I am grateful to them for their cheerful assistance.

I appreciated the help of Scott Mittman with many of the computer programs used to analyze the data.

This manuscript would never have been completed if it were not for the special assistance of Kay Campbell. In addition, Melissa Magdaleno and Brenda Parson helped by typing portions of the manuscript and I am grateful to them for this.

I thank my fellow graduate students for lending moral support in times of crisis. In particular, I have been helped by the friendship of Dave Diner and Rich Terrile (les chwas), and Tony Dobrovolskis.

Finally, my wife, Holly, has made graduate school bearable through her love and understanding.

ABSTRACT

Interferometric observations of Saturn and the rings have been obtained at 3.71 and 1.30 cm wavelengths. The observations have been analyzed by both model fitting and aperture synthesis techniques. They show that the rings have a very low brightness temperature, but attenuate the thermal emission from the planet significantly where they cross in front of it. The latter effect, when combined with the estimate of the ring brightness temperature, permits the optical depths of the rings to be estimated. The fits of the interferometric data to Saturn models in which the A and B rings are combined into a single ring are given in Table (i). The 3.71 cm observations were made at two

TABLE (i)- SUMMARY OF COMBINED A AND B RING RESULTS

λ(cm)	Year Observed	B	T_BRing/T_BPlanet	Optical Depth
3.71	1973-1974	-26.5	0.031 ± 0.007	0.97 ± 0.16[+]
3.71	1976	-20.8	0.043 ± 0.007	0.59 ± 0.10
1.30	1976	-15.3	0.040 ± 0.008	0.54 ± 0.10[*]

+ only the B ring blocked the planet
* includes effect of offset in planetary position from AENA value

epochs and the relative areas of the A and B rings that obscured the planet were different. The apparently inconsistent optical depth results of the two 3.71 cm data sets, then, indicate that the A ring optical depth is significantly less than that of the B ring. The relative areas of the A and B rings are the same for the 1976 1.30 cm and 3.71 cm observations and their optical depth results may be

directly compared. They indicate that the ring optical depths are the same at the two wavelengths. These optical depths are quite similar to those estimated at visible wavelengths. The ring brightness temperatures, which are shown in the table normalized by the brightness temperature of the planet to remove any errors in the absolute calibration of the data, are also the same at the two wavelengths. No variation in the brightness temperature of the rings with tilt angle (B) was detected. A significant amount of radiation from the C ring was detected by the 3.71 cm observations, and the ring was also found to attenuate the planetary emission significantly. Unfortunately, the 1.30 cm observations were not sensitive enough to detect the C ring. The brightness temperature and optical depth results for the individual rings that are implied by all of the 3.71 cm observations are given in Table (ii). Limb-darkening of the planetary emission was simulated by solving for the best fitting planetary radius. No limb-darkening was detected at 3.71 cm, but an apparently significant amount was detected at 1.30 cm. The results at the two wavelengths are significantly different and indicate that the planet is more limb-dark at 1.30 cm

TABLE (ii)- SUMMARY OF 3.71 CM RESULTS FOR INDIVIDUAL RINGS

Ring	T_BRing/T_BPlanet	Optical Depth
A	0.030 ± 0.012	0.2 ± 0.2
B	0.050 ± 0.010	0.9 ± 0.2
C	0.040 ± 0.014	0.1 ± 0.1

than at 3.71 cm. This finding is interesting since it is contrary to what was predicted by atmospheric models which fit the Saturn microwave spectrum. The aperture synthesis analysis is independent of the model fitting and can be used to confirm its results and search for new features not included in the models. The aperture synthesis maps confirm the model fitting results and require no new brightness structures. In particular, no azimuthal variations of the brightness temperature of the rings were detected. The aperture synthesis maps also indicated that the true position of Saturn may be offset from the values given in the American Ephemeris and Nautical Almanac by about 0.3 arcsec. Consideration of simple physical models of the rings has shown that the radiation from the rings at centimeter wavelengths is almost entirely thermal emission from the planet that is scattered to the Earth by the ring particles. The models indicate that the ring particles are very good scatterers and very poor emitters at microwave wavelengths, and this conclusion sets constraints upon the size and composition of the ring particles. The similarity between the optical depths of the rings at visible and centimeter wavelengths probably indicates that the particles are much larger ($\geq$ 1 meter) than the centimeter wavelengths. The large sizes and excellent scattering properties of the particles indicate that they are composed of either a highly reflective or transparent material. At this time water ice is the most likely candidate, since it has been detected in the rings spectroscopically and is known to be highly transparent to microwaves at the low temperatures found at Saturn's rings.

TABLE OF CONTENTS

TABLE OF CONTENTS

TABLE OF CONTENTS

FIGURES

TABLE OF CONTENTS

TABLE OF CONTENTS

TABLE OF CONTENTS

I. INTRODUCTION

> I do not know what to say in a case so surprising, so unlooked for, and so novel. The shortness of time, the unexpected nature of the event, the weakness of my understanding, and the fear of being mistaken, have greatly confounded me.[1]
>
> Galileo Galilei, 1612

The rings of Saturn have been known to astronomers since 1610, when Galileo made his first telescopic observation of the planet and discovered "two lesser stars" surrounding it. However, it took nearly 50 years of careful observation before their true form as a "thin flat ring" surrounding the planet was realized by Huygens. Since that time, the rings have been studied extensively at visible wavelengths by observers with better and better telescopes. The powerful techniques of radar and radio astronomy have been applied to the rings only recently, but they have done a great deal to shape the modern impression of them.

The detection of a substantial radar echo from the rings (Goldstein and Morris, 1973) was as great a surprise to astronomers as Galileo's first observation of them. It was all the more surprising since the radio brightness temperature of the rings was known to be far below their expected physical temperature. The combination of a high radar cross section and a very low

---

[1]Quoted in Alexander, A.F.O'D., The Planet Saturn (London, Faber and Faber, 1962), p. 86.

ring brightness temperature was very puzzling and considered to be something of a paradox. It was soon realized, however, that both the high radar cross section and the low radio brightness temperatures could probably be explained if the ring particles were very good scatterers of microwave radiation and, consequently, very poor absorbers. The excellent scattering properties were clearly needed to explain the radar cross section, and the poor absorption properties meant that the ring particles could not emit thermal radiation efficiently. Thus, the basic solution of the radar and radio observations was understood. However, the full physical mechanism of the high radar cross section has yet to be explained.

The realization that the ring particles were very good scatterers had an interesting consequence for the radio observations; in the limit in which the particles absorbed no radiation, the brightness temperature of the rings would be entirely due to radiation that was thermally emitted by Saturn and scattered to the Earth by the ring particles. When the first detections and low upper limits were set on the brightness temperature of the rings, it became apparent that most, if not all, of the radiation received was scattered planetary emission. The rings of Saturn, then, present radio astronomers with a unique natural scattering experiment to determine the nature of the ring particles.

In order to exploit this natural scattering experiment, the rings must be observed with an instrument that is able to separate their small amount of radiation from the larger amount

of radiation emitted by the planet itself. This separation requires the high resolution that only an interferometer can provide at radio wavelengths. One of the many difficulties of the use of an interferometer is that the data that are obtained are removed from the true appearance of the source by a Fourier transform. One method which is used to interpret the data is to fit models of the source's brightness structure to them. This method has been used to great advantage in the study of planets since, for the most part, the geometrical structure of the planet is known. The method has also been used in the study of Saturn's rings since it does not require an extensive amount of data and the geometrical structure of the rings is known. However, since the rings have been surprising in the past, it would not be too difficult to imagine a situation in which the models that were fit to the planet and rings were incorrect. This is particularly true of models which are fit in an attempt to find new brightness structures on the rings, such as an azimuthal variation in their brightness. Since the radiation from the rings is primarily diffusely scattered planetary emission, an azimuthal variation of it would have important implications for the scattering phase function of the particles as well as for any variations in the density of the particles in the ring. Thus, it is important to investigate the radiation from the rings in a manner that is as free from assumptions concerning the ring brightness structure as possible.

The Fourier transform relation between an interferometer's response to a source and the source's brightness structure can be utilized to produce a map of the source which contains very few assumptions. The technique used to make this map is known as aperture synthesis, and it consists of making many observations of the source with an interferometer and Fourier transforming the data to make the map. This technique and the model fitting technique are complementary in many ways and, when used together, are an effective way to gain information concerning the brightness structure of a radio source. In this work, the two techniques are used to study the brightness structure of the Saturn system.

It is clear that the ring particles possess some unusual scattering properties which will one day yield much information about their size and composition. At the present time, however, too little is known about the rings and their microwave properties to exploit what is known to its full advantage. This work, then, is an attempt to extend the knowledge of the microwave properties of the rings by making detailed interferometric observations of them at two wavelengths. Some qualitative conclusions about the ring particles are possible based on this work and the work of others. However, the lesson of Galileo and Huygens is that more careful observations of the rings may be necessary before the full, elegant solution is known.

II. INTERFEROMETRIC OBSERVATIONS OF SATURN AT A WAVELENGTH OF 3.71 CM

a) Introduction

Interferometric observations of Saturn were made at the Owens Valley Radio Observatory at a frequency of 8085 MHz (3.71 cm wavelength) in 1973, 1974 and 1976. In all, about 200 hours were spent observing the planet. The observations were made in two separate campaigns and represent two independent sets of interferometric data. The stronger of the two data sets was obtained in May and June of 1976, when the saturnocentric declination of the Earth (B) averaged -20.8 degrees. The other data set was obtained in August of 1973 and January of 1974. The 1973 and 1974 runs may be considered together, since B was -26.5 degrees for both runs.

The 1976 data set is stronger than the 1973-1974 data set, because, in general, the signal to noise ratio is better and the observations were made on many more interferometer baselines. In particular, more short baselines, which are the most sensitive to large features like the rings, were employed. In addition to these considerations, greater care was taken in the phase calibration of the 1976 observations after efforts to make an aperture synthesis map out of the 1973-1974 data demonstrated that such care was necessary. In general, the analysis performed on the 1973-1974 data set before the 1976 data set was obtained was a great help in the design of the 1976 experiment and largely accounts for the improved results.

Although the data obtained in 1976 are superior, they do not make careful consideration of the 1973-1974 data set unnecessary. The 1973-1974 data set can add two important features to the final results obtained in this study of the 3.71 cm radiation from Saturn. First of all, the 1973-1974 data are a completely independent data set, and therefore, results obtained from them may be used to check the consistency of results obtained from the 1976 data set. Secondly, since the appearance of Saturn was different in 1973-1974 than it was in 1976, the two independent data sets can be used to extract information about how the brightness of the rings and the planet change with ring tilt angle. Thus, the two data sets are each important to a full understanding of all aspects of the 3.71 cm radiation from the Saturn system.

b) The 1976 Observations

The 1976 Owens Valley Radio Observatory observations were made on 13 interferometer baselines and resulted in the u-v coverage shown in Figure 1. Observations on the shortest baseline were made during 21-23 May 1976, using only the two 90' antennas. All other observations were made during 16-29 June 1976, using the two 90' antennas and the 130' antenna as a three element interferometer. The receivers were degenerate parametric amplifiers, and the overall system temperature was measured to be about 140°K. All observations were made with parallel, linearly polarized feeds oriented either parallel to the central meridian of Saturn (PA = -7°) or perpendicular

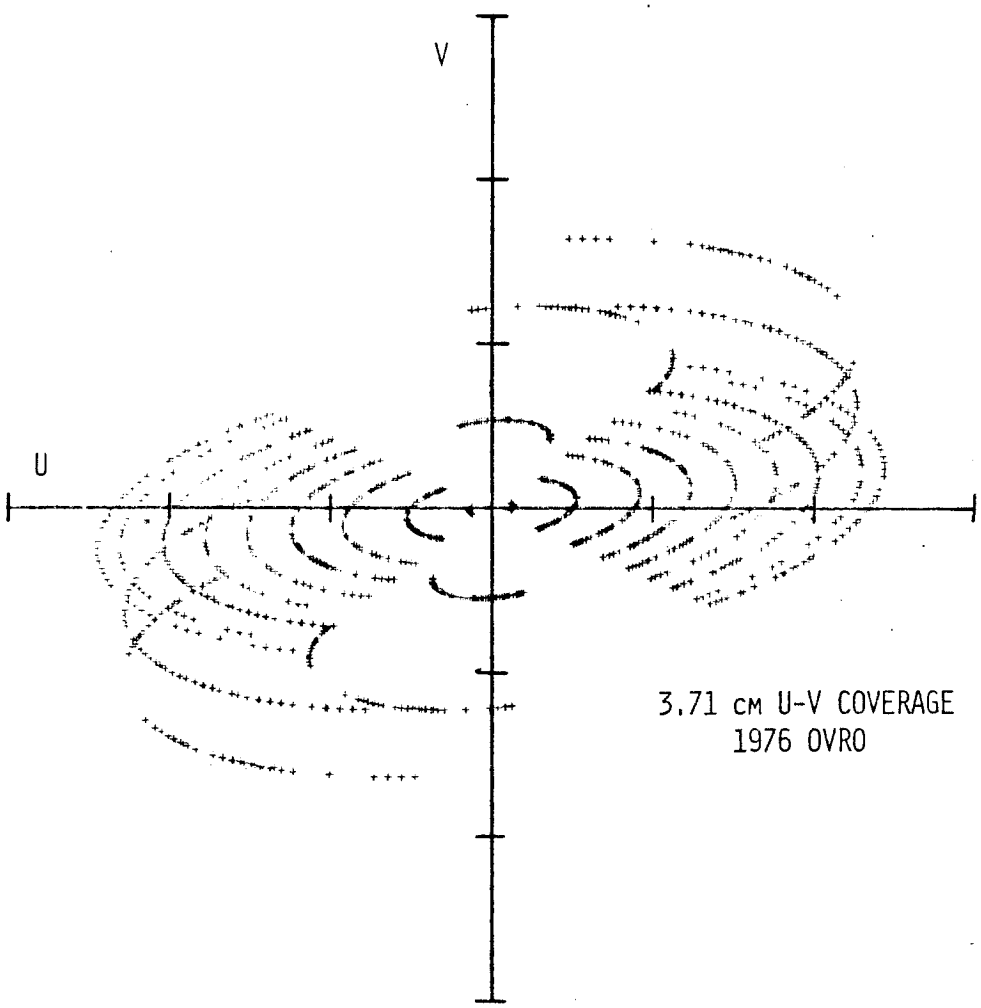

Figure 1 - u-v coverage of 1976 OVRO observations. u and v are the interferometer spacings, expressed in wavelengths, projected onto the planet Saturn. The v axis is at a position angle of -7^{o} so that it coincides with the central meridian of Saturn. The intersection of the axes is the point u = 0, v = 0. The u axis increases to the left in increments of 10,000 wavelengths for Saturn as seen at the standard distance of 8 AU. The v axis increases to the top of the figure and is at the same scale. The visibility function at a point u,v is equal to its complex conjugate at -u,-v. Therefore, both values are plotted in the figure since there is information about the source at both locations.

to it (PA = 83°). Antenna pointing was under the control of the observatory's computer, and it was found to be better than 0.5 arcmin. Typically, four 7-minute Saturn integrations (two in each polarization) were followed by two 5-minute integrations on a calibrator (one in each polarization). Thus, the instrumental gain and phase were calibrated about once every 50 minutes. The interferometer baselines were determined by observing a group of point sources scattered about the sky and comparing their phases. The same group of calibrators was used for all baselines to minimize any possible systematic differences. The baseline which gave the smallest residual phase changes between sources was the one adopted for the final data reduction. After the data were reduced to fringe amplitudes and phases, a correction was applied to the amplitudes to compensate for the change in antenna gain with increasing zenith angle.

OJ287 was chosen as the principle calibrator for the Saturn data. This choice was made because it was less than 50 minutes of right ascension east of Saturn and at almost exactly the same declination. It was hoped that this proximity would minimize any systematic errors having to do with the position of the sources in the sky, such as pointing errors or residual baseline errors. In addition, this proximity meant that little time was wasted in moving the antennas from the source to the calibrator. A principal drawback of the use of OJ287 as a calibrator is its well known and widely studied variability. The variability of OJ287 meant that its

flux density had to be determined and monitored in the course of the observing run.

The flux density of OJ287 was measured relative to the flux density scale shown in Table 1. This scale is based upon CTA21, a non-variable source which is assumed to have a flux of 1.75 Jansky. This value was derived by interpolation of the values of Pauliny-Toth and Kellermann (1968) at 5000 MHz and Kellermann and Pauliny-Toth (1973) at 10700 MHz. The flux densities of the other sources, 3C48 and 3C138, were determined by comparison to CTA21. Although many observations were made of these sources, only those adjacent to an observation of CTA21 which were taken in winds less than 10 mph were used to determine their flux densities. In addition, because the receiver gain of the 130' antenna was subject to large drifts during the day, only the observations made on the baseline between the 90' antennas were included. The resulting flux density scale is compared to other interpolated values of Kellermann and Pauliny-Toth (1973) and Pauliny-Toth and Kellermann (1968) and to the measurements of Altschuler and Wardle (1976) in Table 1.

OJ287 was monitored during the observing run by comparing its flux density to one of the calibrators (most often 3C138). As in the case of the other sources, only observations of OJ287 made on the 90' antennas' baseline adjacent to another calibrator, and in less than 10 mph winds were used in its flux determination. The individual OJ287 observations are shown in Figure 2 along with observations made by Dent (private communication) during the same time period at 7875 MHz. Both

TABLE 1

FLUX SCALE USED FOR 8085 MHz SATURN OBSERVATIONS

COMPARED WITH OTHER MEASUREMENTS

Source	Flux Density (Jansky)*		
	This Study	Interpolation Between 5 GHz[§] and 10.7 GHz[†]	Altschuler and Wardle (1976)
3C48	3.6	3.41	3.30
CTA21	1.75	1.75	1.73
3C138	2.7	2.86	2.48

[§] 5 GHz flux density from Pauliny-Toth and Kellermann (1968).

[†] 10.7 GHz flux density from Kellermann and Pauliny-Toth (1973).

* 1 Jansky = 10^{-26} W M^{-2} Hz^{-1}.

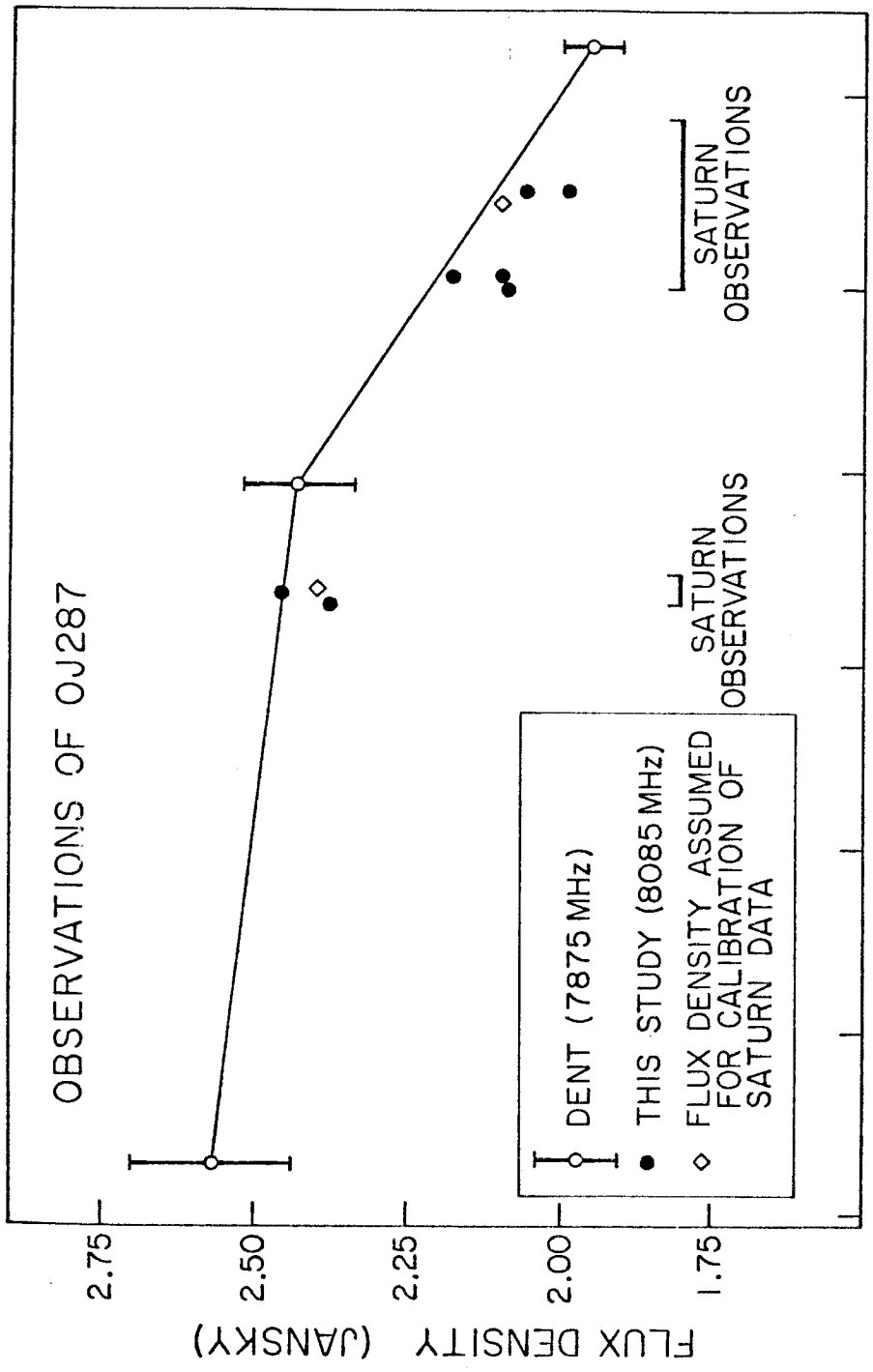

Figure 2 - Flux density measurements of the principal Saturn calibrator, OJ287, made during the 1976 Owens Valley Saturn observations. The values of W.A. Dent (private communication) at 7875 MHz are shown for comparison. The lines connecting Dent's measurements are only illustrative.

the Owens Valley observations and the observations of Dent show a significant decrease in the flux density of 0J287 between the May and June portions of the observing run. It is possible that 0J287 changed during the June run as well, although the change indicated by the June data is probably not significant. Therefore, it is assumed that the flux density of 0J287 remained constant during each portion of the observing run. A value of 2.4 Jansky is adopted for the May portion and a value of 2.1 Jansky is adopted for the June portion. These values are the only ones used to determine the instrumental gain. The absolute calibration of the Saturn data is, therefore, only dependent upon the determination of the flux density of 0J287. The instrumental phase is determined principally by observations of 0J287, although it has been supplemented by observations of other calibrators each day before and after 0J287 was available.

It is important to determine whether the flux density of 0J287 varied during the time that the Saturn observations were made, since a variation in the flux density of the calibrator will affect the relative calibration of the observations on different baselines. In the case of the relative calibration of the May and June portions of the observing run, an undetected variation in the flux density of the calibrator would have had serious consequences since it would have raised or lowered the observations that resolved the source the least relative to all of the other observations. This would have caused the contribution to the visibility function attributed to large components of the Saturn system, such as the rings, to be estimated incorrectly,

since they are the most affected by the shape of the visibility function at short spacings. Thus, careful monitoring of 0J287 is important not only for the absolute calibration of the data, but for the relative calibration and subsequent analysis as well.

c) The 1973-1974 Observations

The 1973-1974 observations were made at the Owens Valley on five interferometer baselines and resulted in the u-v coverage shown in Figure 3. Observations on the three east-west baselines were made during 26 July-5 August 1973, using the two 90' antennas and the 130' antenna as a three element interferometer. The observations on the two north-south baselines were made during 17-22 January 1974, using the two 90' antennas.

The receivers and observing procedures were the same as those used in 1976. The observations were made using parallel, linearly polarized feeds oriented either parallel (PA = -6°) or perpendicular (PA = 84°) to the central meridian of Saturn. Ten-minute records were taken on Saturn and the system was calibrated approximately once each hour. The principal calibrator used for these observations was 3C138, and it was assumed to have a flux density of 2.7 Jansky to make it consistent with the 1976 observations. The data were reduced and calibrated using the standard reduction programs of the Owens Valley Radio Observatory.

Two principal differences exist between the 1973-1974 observations and the 1976 observations in addition to those already mentioned. First, the 1973-1974 observations were made before the 90' telescopes

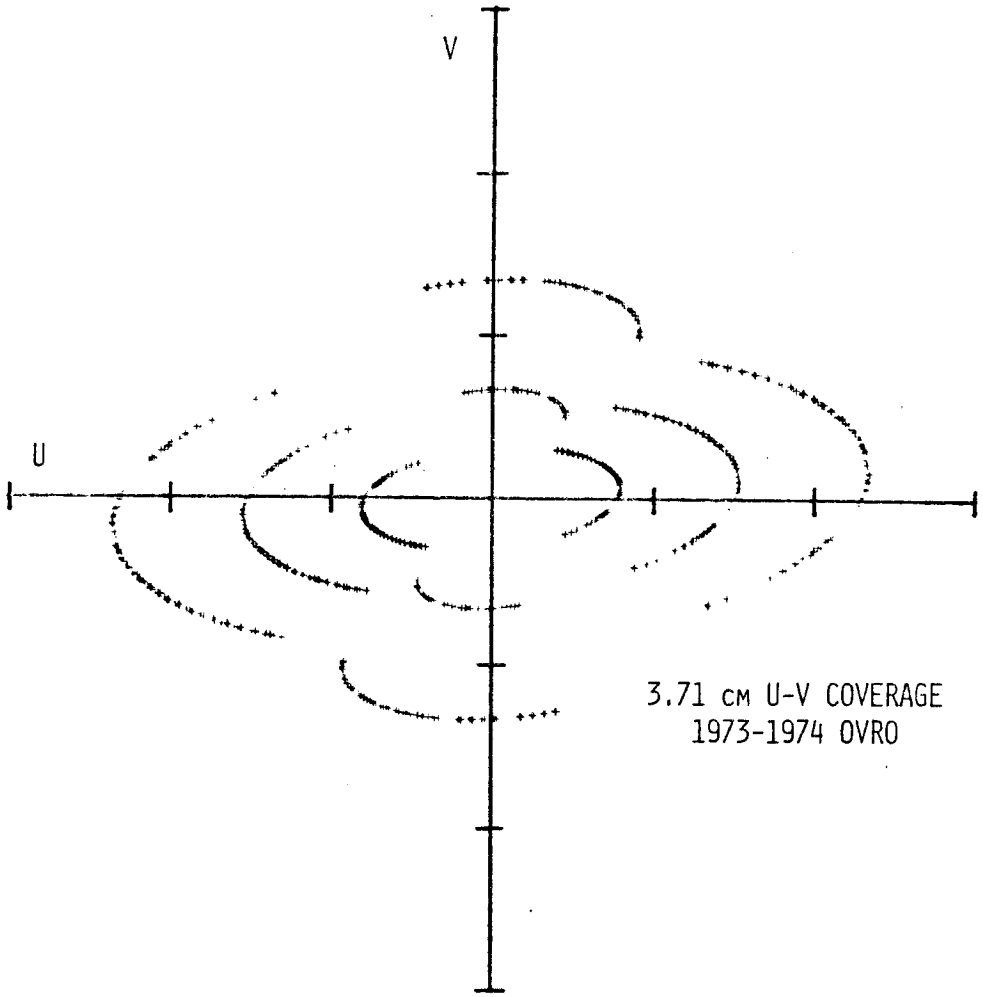

Figure 3 - u-v coverage of 1973-1974 OVRO observations. u and v are the interferometer spacings, expressed in wavelengths, projected onto the planet Saturn. The v axis is at a position angle of -6° so that it coincides with the central meridian of Saturn. The intersection of the axes is the point u = 0, v = 0. The u axis increases to the left in increments of 10,000 wavelengths for Saturn as seen at the standard distance of 8 AU. The v axis increases to the top of the figure and is at the same scale. The visibility function at a point u,v is equal to its complex conjugate at -u,-v. Therefore, both values are plotted in the figure since there is information about the source at both locations.

were put under computer control. This meant that the pointing corrections for the 90' antennas had to be put in manually before each record, and they are expected to be inferior to the computer controlled pointing of the 1976 observations. Second, the corrections for the zenith angle dependence on antenna gain were not the same as those used for the 1976 data set. Again, although they are adequate for this work and not grossly different from the corrections applied to the 1976 data, they are expected to be inferior. Because of these two differences in the reduction of the 1973-1974 data, it is expected that this data set is more prone to systematic errors in fringe amplitude than the 1976 data set.

III. ANALYSIS OF THE OWENS VALLEY 3.71 CM OBSERVATIONS BY MODEL FITTING TECHNIQUES

a) Introduction

Observations of a radio source with an interferometer sample the complex, two-dimensional Fourier transform of the source's brightness distribution. In cases where the source's geometrical structure is known, the source may be modeled, and the observations can be used to determine the relative brightness temperatures of the model components. In this study, model fitting is used to determine the brightness temperatures of the planet, the A and B rings and the portion of the planet which is blocked by the rings. The brightness temperature of the region of the planet that is blocked by the rings is determined separately, since it is essentially due to planetary emission that is attenuated by the rings. These features have all been shown to be necessary to reproduce the measured visibility function at this wavelength by previous workers (Muhleman et al. 1976; Briggs, 1974; Cuzzi and Dent, 1975). In addition, the effects of a hypothetical C ring and limb-darkening of the planet have been included in subsequent models in order to test whether they are present. In all cases, the planet, rings and region of blockage have been modeled as uniformly bright, and limb-darkening has been approximated by changing the size of the uniformly bright planet.

b) Model Fitting Procedures

In order to fit models of the Saturn system brightness structure to the data, it is necessary to know the absolute sizes and positions of each of the regions as they appeared on the sky at the time of the observations. The dimensions of the regions have been mostly taken from the review of Cook et al. (1973), and they are summarized in Table 2. The distance to the planet and its geocentric position were taken from the American Ephemeris and Nautical Almanac. The dimensions of the planet and rings that are given in the AENA are also shown in Table 2.

A principal difference between the dimensions of Cook et al. (1973) and those used in the model is the correction of the true polar radius of Saturn to the apparent polar radius at the time of the observations. The apparent polar radius is given by

$$R_{P_A} = \sqrt{\cos^2 B \, R_P^2 + \sin^2 B \, R_E^2}$$

which is the apparent polar radius for a planet of true polar and equatorial radii, R_p and R_E, as viewed from a planetocentric declination, B, This effect significantly changes the size of the planet and the blocked region and affects estimates of their relative brightness. The other difference between the model and the dimensions of Cook et al. (1973) is that the Cassini division between the A and B rings has been ignored. The boundary between the rings in the model has been placed in the middle of the division, which has been ignored

TABLE 2

MODEL DISK AND RING DIMENSIONS

(IN ARCSEC AT 8 A.U.)

		Cook et.al. (1973) (adopted for models)	American Ephemeris and Nautical Almanac
PLANET RADII			
True Equatorial		10.31	10.42
True Polar		9.25	9.32
Apparent Polar:			
OVRO 1973-1974	B= -26.5	9.47	
OVRO 1976	B= -20.8	9.39	
HCRO 1976	B= -15.3	9.33	
RING RADII			
Inner C Ring		12.52	12.87
Inner B Ring		15.75	15.60
Outer B Ring		20.11	20.17
Outer B and Inner A adopted for models		20.53	
Inner A Ring		20.95	20.65
Outer A Ring		23.63	23.46

because the observations lack the spatial resolution necessary to make meaningful statements about it.

The ultimate goal of the model fitting procedure is to find a model which fits all of the data to their accuracy. This implies that the data which go into a least squares model fit should be weighted by their errors. In this study, the data errors have been estimated from the scatter of the data. It was felt that this method would come the closest to estimating the true errors because it includes systematic errors that vary from day to day as well as the normal statistical errors. A flat portion of the visibility vs. hour angle curve was chosen and the error (1σ) of the data was taken to be 1/3 of the peak-to-peak scatter of points. These errors have been tabulated in Table 3. All of the data points on a given baseline were taken to have the same error.

The errors on the amplitude and phase of the visibility function have been estimated independently since they are separately calibrated and should be mostly independent. This independence implies that the amplitudes and phases of the visibility function, rather than its real and imaginary parts, should be fit to the data since the errors on the real and imaginary parts are correlated. Unfortunately, a fit to the data amplitudes and phases is not linear in the parameters that are to be determined. Therefore, instead of using a non-linear least squares procedure to fit amplitudes and phases, the real and imaginary parts have been fit and the data weighting has been modified to include the

TABLE 3

ERRORS USED IN MODEL FITTING TO OWENS VALLEY DATA

Baseline	Amplitude Error (Jy)	Phase Error (lobes)	Average Amplitude† (Jy)	Number of Points
		1973-1974		
1200'EW	0.060	0.07	0.963	150
2300'EW	0.044	0.07	0.241	146
3500'EW	0.021	0.08	0.137	132
800'N-400'E	0.060	0.02	1.457	36
1600'N-800'E	0.016	0.04	0.090	76
		1976		
200'EW	0.047	0.03	2.282	18
1400'EW	0.030	0.03	0.890	47
800'EW	0.047	0.03	1.728	66
800'N-400'E	0.047	0.03	1.772	65
1600'N-1600'E	0.030	0.03	0.226	51
2300'EW	0.030	0.03	0.251	48
2900'EW	0.023	0.04	0.233	31
3100'EW	0.030	0.04	0.196	65
1900'EW	0.030	0.04	0.407	54
3700'EW	0.023	0.04	0.160	47
3500'EW	0.023	0.04	0.141	30
800'N-3500'E	0.023	0.04	0.184	63
1600'N-1600'E	0.023	0.04	0.142	50

† Flux density at standard distance of 8 AU.

effects of the correlations between them. This procedure is equivalent to rotating the real and imaginary axes by the phase of each data point and writing the equations of condition in this new rotated space. Now, the errors on the new "real" and new "imaginary" parts are taken to be the amplitude error and the phase error times the average amplitude on the particular baseline. Since these errors are uncorrelated, the model fitting procedure has achieved the desired result of fitting uncorrelated data with a linear least squares scheme.

A further consideration has been applied to the weighting of the 1973-1974 data set. In this case, the three baselines of 1973 data have far more individual data points to be fit than do the 1974 baselines. If the weighting were done only on the basis of the individual data point errors, then the 1973 east-west baselines would dominate the model fit and the crucial north-south baselines of 1974 would be largely ignored. It would not be correct to force the model to neglect some baselines simply because others contain an overwhelming number of data points. The observations made on each baseline sample a separate region of the u-v plane and contain unique information about the source's brightness structure. Thus, upweighting heavily sampled baselines has the effect of downweighting the information contained in the less well sampled baselines and the brightness structure will not be as well determined as it would have been if all information had been considered equally. To correct this effect the observations on a given baseline have been downweighted by the number of observations

on that baseline. This correction makes each baseline equally important in determining the best fit models. The 1976 data set has not had this factor applied since each baseline has an approximately equal number of observations.

c) Results of Model Fitting

The results of the model fitting to the 1973-1974 and 1976 Saturn data sets are presented in three parts. In part one, only models with the planet, the blocked region and the A and B rings are considered. These are the principal features of the brightness structure of the microwave emission from Saturn. In part two, the C ring is examined to see whether it has a detectable brightness or blocks the planetary emission to any degree. In part three, the effect of limb-darkening of the planetary emission is considered by solving for the best planetary radius. Since limb-darkening changes the apparent size of the planet, a solution for the radius of the planet allows an estimate of the degree to which limb-darkening is present.

(i) Models Consisting of the Planet, the Blocked Region and the A & B Rings

The results of the A and B ring models are shown in Table 4. In Model 1 the A and B rings are considered to be a single, uniformily bright ring and the data are used to solve for its brightness temperature and the brightness temperatures of the unblocked planet and the blocked region. The brightness temperatures of the

TABLE 4

RESULTS OF A AND B RING MODELS (3.71 cm)

Model	T_B Planet	T_B Planet Blocked by A + B Ring	T_B B Ring	T_B A Ring	T_{DISK}[+]	Improvement in Residuals Relative to Model 1 (percent)
			1973-1974			
1	168.3 ± 1.7 (1.000 ± 0.010)	25.8 ± 5.2 (0.153 ± 0.031)	5.3 ± 1.2 (0.031 ± 0.007)	5.3 ± 1.2* (0.031 ± 0.007)	163 K	-
2	168.4 ± 1.7 (1.000 ± 0.010)	26.3 ± 5.2 (0.156 ± 0.031)	10.8 ± 2.5 (0.064 ± 0.015)	0.6 ± 2.2 (0.004 ± 0.013)	164 K	1.2
			1976			
1	182.3 ± 1.4 (1.000 ± 0.008)	41.7 ± 7.5 (0.229 ± 0.041)	7.9 ± 1.2 (0.043 ± 0.007)	7.9 ± 1.2* (0.043 ± 0.007)	169 K	-
2	182.4 ± 1.4 (1.000 ± 0.008)	42.1 ± 7.5 (0.231 ± 0.041)	11.3 ± 2.2 (0.062 ± 0.012)	3.2 ± 2.7 (0.018 ± 0.015)	169 K	0.6

* A and B rings combined into single ring.

+ $T_{DISK} = \frac{\lambda^2}{2k} \times \frac{\text{Model Flux Density}}{\text{Solid Angle of Elliptical Disk with AENA Radii}}$

A and B rings are solved for separately in Model 2. In order to make the results as free as possible from errors in the absolute calibration of the data, the model parameters are also shown in Table 4 normalized by the brightness temperature of the unblocked planet. Absolute calibration errors should affect all of the brightness temperatures by the same factor so that the relative values should be unaffected.

As can be seen in Table 4, both models are consistent with what has been found previously at 3.71 cm (Muhleman et al., 1976; Cuzzi and Dent, 1975; Briggs, 1974). The unblocked portion of Saturn is the brightest feature in the models, and the blocked region has only about one-fifth of its brightness temperature. The rings are dimmer still and have a brightness temperature which is only a few percent of that of the planet.

When the results of the fits to the 1973-1974 and 1976 data sets are considered more quantitatively and compared, some interesting similarities and differences are found. A rather disturbing difference between the two solutions is that the 1976 planet brightness temperature is about 8% higher than the 1973-1974 solution. If this difference were due only to some residual absolute calibration error between the two data sets, then that calibration error should show up in the unresolved fluxes of the models as well. Since the difference in the unresolved flux is only 3%, the planet brightness temperature difference may be due to errors in the relative calibration

of the observations within a single data set, correlations with other parameters in the models or other, unmodeled, structures, or a true variation in the brightness temperature of Saturn.

The possibility that the brightness temperature of the planet changed by 8% with a change in sub-Earth latitude of only 6° can only be explained if Saturn is considerably pole dark. Although such a possibility is unlikely, these data are not able to exclude it. The extent to which the other possibilities occur is difficult to evaluate. In any event, they are expected to have similar effects on the results. These possibilities would introduce errors into the other parameters in the model and make comparisons between the results of the two data sets difficult. Therefore, since it is unlikely that the full 8% difference is real, some caution should be used when comparisons between the results of the two data sets are made.

The normalized brightness temperature of the blocked region seems to change significantly from 0.153 ± 0.031 in 1973-1974 to 0.229 ± 0.041 in 1976. This difference should be viewed with special caution since it is expected to be affected more by uncertainties in the planet brightness temperature than in the ring brightness temperature. This is because the correlation coefficient between the blocked and unblocked planet brightness temperatures in the 1976 model fit is -0.66 and is more than twice the size of any other correlation.

There are good reasons to expect that the normalized brightness temperature of the blocked region will change as the tilt of the rings

changes. First, if the A and B rings had the same optical thickness and only served to attenuate the emission from the planet, then the amount of attenuation would be a function of tilt angle (B, the complement of the angle of incidence) since the optical depth along the line-of-sight through a plane-parallel slab is

$$\tau_{\text{line of sight}} = \tau_o/\sin B \quad ,$$

where τ_o is the normal incidence optical depth. Second, the region blocked by the A and B rings is about 30% covered by the A ring in 1976, while in 1973-1974 the blockage is almost completely caused by the B ring. If the A ring is less opaque than the B ring, as expected, then the blocked region should appear relatively brighter in 1976.

In order to determine whether the change in the line-of-sight optical depth is responsible for the change in the normalized brightness temperature of the blocked region, it is necessary to estimate the optical depth implied by the brightness temperature observed. The simplest way to do this is to assume that the rings contribute no flux of their own and that the brightness temperature of the blocked region is due only to attenuation of the emission from the disk. In this way, the optical depth may be estimated from

$$\frac{T_{BLOCKED}}{T_{PLANET}} = e^{-\tau_R/\sin B}$$

where $T_{BLOCKED}$ and T_{PLANET} are the brightness temperatures of the blocked

and unblocked portions of the planet (i.e. columns 2 and 3 in Table 4) and τ_R is the normal optical depth of the rings. The optical depths estimated this way, given in Table 5, are 0.84 ± 0.09 in 1973-1974 and 0.52 ± 0.05 in 1976. Thus, this simple estimate of the optical depths indicates that the brightness temperature change is not simply due to a change in the line-of-sight optical depth.

Unfortunately, it is not possible to solve for the brightness temperatures of the regions blocked by the A and the B ring separately. These regions appear almost the same to the model fit because of their similar position and shape, and the high degree of correlation between them makes physically plausible solutions impossible. Therefore, an indirect approach is necessary to determine whether the A and B rings block the planetary emission by different amounts.

The change in normalized brightness temperature of the blocked region may be explained if the A ring is much less optically thick than the B ring. If the blocked region brightness temperature is taken to be the average brightness temperature of the portion blocked by the B ring and that blocked by the A ring weighted by their relative areas, then it is given by

$$\frac{T_{BLOCKED}}{T_{PLANET}} = f_A e^{-\tau_A/\sin B} + f_B e^{-\tau_B/\sin B} \qquad (1)$$

where f_A and f_B are the fractions of the blocked area covered by the A and B rings and τ_A and τ_B are the normal optical depths of the A and B rings. Since the 1973-1974 data were taken when the B ring

TABLE 5

3.71 cm RING OPTICAL DEPTHS FROM A AND B RING MODELS

	Normal Optical Depth	
	$\frac{T_B \text{ Rings}}{T_B \text{ Planet}} = 0.00$	$\frac{T_B \text{ Rings}}{T_B \text{ Planet}} = 0.04 \pm 0.01$
A + B Ring		
1973-1974	0.84 ± 0.09	0.97 ± 0.16
1976	0.52 ± 0.05	0.59 ± 0.10
A and B Separated		
B Ring	0.84 ± 0.09	0.97 ± 0.16
A Ring	0.24 ± 0.09*	0.29 ± 0.13*

* Uncertainty does not include uncertainty on B ring optical depth.

did practically all of the blocking, the 1973-1974 optical depth can be taken to be that of the B ring and used to find the A ring optical thickness from the 1976 value. Thus, adopting the estimate of 0.84 ± 0.09 for the B ring optical depth, the A ring optical depth can be found from equation (1). This gives an estimate of 0.24 ± 0.09 for the optical depth of the A ring. Thus, it appears that the A ring is less optically thick than the B ring, as might have been expected from their relative optical thicknesses at visible wavelengths. It is apparent, though, that the planet brightness temperature difference between the 1973-1974 and 1976 data sets may have some effect on this optical depth determination and therefore, the results should be viewed cautiously.

The optical thicknesses derived so far are almost certainly underestimates. This is because they neglect the contribution of the rings to the brightness temperature of the blocked region. The brightness temperature of the blocked region is properly given by the sum of the attenuated planet brightness temperature and the brightness temperature of the rings so that

$$\frac{T_{BLOCKED}}{T_{PLANET}} = e^{-\tau_R/\sin B} + \frac{T_{RINGS}}{T_{PLANET}}$$

should be used to compute the ring optical depth. If the rings are taken to have the same brightness temperature where they cross the planet that they have away from the planet, then, adopting a normalized ring brightness of 0.04 ± 0.01, the optical depths can be cor-

rected for this effect. These corrected optical depths, which are also shown in Table 5, are higher than the optical depths with no ring brightness temperature correction and are likely to be closer to the true values. They do, however, carry the uncertainty in the assumption that the rings have the same brightness temperature in front of the planet that they do away from it. The final results for the optical depths of the combined A and B rings are 0.97 ± 0.16 for the 1973-1974 data set and 0.59 ± 0.10 in 1976. Since these, again, are not consistent with a single optical thickness, the rings are allowed to have different optical thicknesses to fit the observed brightness temperature change. The B ring optical depth is found from the 1973-1974 data to be 0.97 ± 0.16 and this value is used with the 1976 results to derive a value for the A ring of 0.29 ± 0.13. Thus, the correction for ring brightness temperature does not change the essential conclusion that the A ring is significantly less optically thick than the B ring at centimeter wavelengths.

The normalized brightness temperature of the combined A and B ring does not appear to change significantly since the results, 0.031 ± 0.007 for the 1973-1974 data and 0.043 ± 0.007 for the 1976 data, overlap. These results formally mean that there is no change in the ring brightness temperature as the ring tilt changes. Unlike the blocked region, it is possible to solve for the brightness temperatures of the A and B rings independently and this has been done in Model 2. The results for the brightness temperatures of the

planet and the blocked region are almost exactly the same as those of Model 1 and therefore, they require no further discussion. The ring results are different from those of Model 1 and suggest that the B ring has a significantly higher brightness temperature than the A ring. The 1973-1974 solutions are very nearly the same as those of 1976, and this is a strong indication that there is no change in the brightness temperature of the rings between the tilts of 26.5 and 20.8. Thus, the conclusion drawn from Model 1 is supported by the results of Model 2.

The models which contain the A and B rings, the region where the rings block the planet, and the unblocked planet have shown all of the major features of the microwave emission from Saturn and probably provide an adequate fit to the data. The rings have a very low brightness temperature which is, on the average, only 4 ± 1% of the brightness temperature of the unblocked planet. This brightness temperature did not change by more than about 1% of the planet brightness temperature with the change of ring tilt that occurred between 1973 and 1976. In addition, Model 2 suggests that the B ring brightness temperature is greater than the A ring's by a factor of about 3 (based on the 1976 model results). The blocked region changes brightness temperature between 1973-1974 and 1976 in a manner that cannot be explained by a single optical thickness for the rings. This brightness temperature change is best explained by allowing the A ring to be less optically thick than the B ring. If a ring brightness temperature of 4 ± 1% of the planet brightness temperature is

allowed for, then the optical thicknesses required by all of the data are 0.97 ± 0.16 for the B ring and 0.29 ± 0.13 for the A ring.

Although all of these results are consistent with the measurements of previous observers and the results expected on theoretical grounds, they should be viewed with some caution because of the difference in the planet brightness temperature between the 1973-1974 and 1976 data sets. It is possible that correlations between this parameter and the various ring-related parameters will adversely affect the ring results, although the consistency of the results would seem to refute this claim. It is also possible that unmodeled parameters, some of which are to be considered in the following sections, may affect the ring results or cause the difference in the planet brightness temperature. All of these possibilities must be kept in mind when interpreting the results and comparing them to the work of others.

(ii) Models Including the C Ring

In this section, models including the C ring are fit to the 1973-1974 and 1976 data sets in order to determine whether the C ring has a detectable brightness temperature or blocks the emission from the planet in a significant way. The results of the C ring model fits are given in Table 6 in terms of brightness temperatures and brightness temperatures normalized by the brightness temperature of the unblocked planet. The brightness temperature of the C ring, the region of the planet blocked by the C ring and the regions defined in Model 1 are solved for in Model 3. The brightness temperatures of the C ring, the region of the planet blocked by the C ring and the regions defined

TABLE 6

RESULTS OF MODELS INCLUDING THE C RING (3.71 cm)

Model	T_B Planet	T_B Planet Blocked by C Ring	T_B Planet Blocked By A + B Ring	T_B C Ring	T_B B Ring	T_B A Ring	T_{DISK} †	Improvement in Residuals Relative to Model 1 (percent)
				1973-1974				
3	169.9 ± 1.8 (1.000 ± 0.011)	154.3 ± 9.5 (0.908 ± 0.056)	32.5 ± 7.7 (0.191 ± 0.045)	8.4 ± 3.1 (0.049 ± 0.018)	6.9 ± 1.3 (0.041 ± 0.008)	6.9 ± 1.3* (0.041 ± 0.008)	168 K	1.9
4	169.7 ± 1.8 (1.000 ± 0.011)	154.4 ± 9.5 (0.910 ± 0.056)	33.1 ± 7.7 (0.195 ± 0.045)	6.1 ± 3.9 (0.036 ± 0.023)	9.2 ± 2.7 (0.054 ± 0.016)	4.4 ± 3.0 (0.026 ± 0.018)	167 K	2.1
				1976				
3	186.0 ± 1.7 (1.000 ± 0.009)	106.9 ± 21.2 (0.575 ± 0.114)	65.2 ± 9.8 (0.351 ± 0.053)	8.9 ± 3.0 (0.048 ± 0.016)	7.6 ± 1.3 (0.041 ± 0.007)	7.6 ± 1.3* (0.041 ± 0.007)	171 K	3.4
4	186.0 ± 1.7 (1.000 ± 0.009)	107.2 ± 21.2 (0.576 ± 0.114)	65.2 ± 9.8 (0.351 ± 0.053)	7.9 ± 3.3 (0.042 ± 0.018)	9.0 ± 2.4 (0.048 ± 0.013)	5.9 ± 2.7 (0.032 ± 0.015)	172 K	3.5

* A and B rings combined into a single ring.

† $$T_{DISK} = \frac{\lambda^2}{2k} \times \frac{\text{Model Flux Density}}{\text{Solid Angle of Elliptical Disk with AENA Radii}}$$

in Model 2 are solved for in Model 4. Both Model 3 and Model 4 when fit to both the 1973-1974 and 1976 data sets show that the C ring has a significant brightness temperature which is comparable to that of the other rings. They also show that the C ring attenuates the planetary emission by a significant amount where the rings cross the planet.

Since the C ring has not been examined previously, it is necessary to take care to show that the C ring results are truly significant and improve the fit of the models to the data. An examination of the results and their errors shows that the estimated C ring brightness temperature is 2 to 3 times its error. Similarly, the brightness of the blocked region is about one sigma different from the unblocked region in 1973-1974 and about three sigma different in 1976. In most cases, these would be sufficient grounds to believe that the C ring results are real. However, it was felt that the correlations between the C ring regions and the other regions in the model fit might cause the C ring regions to take on a falsely significant brightness temperature. Therefore, some Monte Carlo calculations were done in order to determine whether the other parameters in the model fit could come together and produce an erroneous result. It was found, assuming that the noise on the amplitudes and phases of the visibility function was normally distributed, that no ficticious values for the C ring parameters in excess of one sigma were produced. Further, by comparing the results of the models with and without the C ring, it can be seen that the values of the other parameters, with

the possible exception of the brightness temperature of the portion of the planet blocked by the A and B rings, do not change greatly. These parameters would be expected to change if the C ring results were erroneous and due only to correlations with them. Finally, the presence of the C ring improves the sum of the squares of the residuals of the model fit, as seen in column 9 of Table 6. This improvement should be viewed somewhat skeptically since even the introduction of irrelevant parameters is expected to improve the residuals. However, in view of the sizes of the C ring parameters relative to their errors, the consistency of the model results for the 1973-1974 and 1976 data sets and the consistency of the C ring model results with those of the models without the C ring, this improvement in the residuals is most likely significant and the C ring results are probably real.

The ring brightness temperature results of Models 3 and 4 are consistent with the results of Models 1 and 2. These results are all consistent with the ring brightness temperature being constant with changing ring tilt and indicate that this brightness temperature cannot change more than about 1% of the planet brightness temperature between the tilt angles of 20.8 and 26.5 degrees. All of the rings have approximately the same brightness temperature, although an interesting, but formally insignificant, difference between the individual rings is seen in Model 4. In both the 1973-1974 and 1976 models, the B ring has the largest brightness temperature at about 5% of the planet brightness temperature, and is followed by the C and the A rings, at about 4% and 3%. The difference in brightness temperature

between the A and B rings in this model is no longer as great as it was when the C ring was not included, although the new results are still within one sigma of the old ones. This difference in results may reflect some correlation with the unmodeled C ring in Models 1 and 2. At any rate, the results of Model 4 are expected to be closer to the true answer since the C ring is a significant feature of the microwave radiation from Saturn.

The model results for the regions blocked by the C ring and by the A and B rings are not as nicely consistent as the ring results. When the C ring is added in Models 3 and 4, the brightness temperature of the region blocked by the A and B rings changes significantly in 1976 and substantially in 1973-1974. This is not too surprising since the two blocked regions are highly correlated in the model fit. The correlation coefficients are -0.72 for the 1973-1974 data set and -0.69 for the 1976 data set, and they are the largest correlations in the model fit. The correlations are in the sense that if one brightness temperature is overestimated, then the other will be underestimated. Thus, the inconsistency between the two data sets is disconcerting because it suggests that these correlations have been active and that, therefore, comparisons between the two data sets are somewhat risky. These potential dangers must be kept in mind when interpreting the brightness temperatures of the blocked regions in terms of optical depths.

The optical depths implied by the results of Model 3 are summarized in Table 7. The calculations which led to these numbers are the same as those used to calculate the optical depths in Table 5 and

TABLE 7

3.71 cm OPTICAL DEPTH OF MODELS INCLUDING C RING

	$\frac{T_B Rings}{T_B Planet} = 0.00$	$\frac{T_B Rings}{T_B Planet} = 0.04 \pm 0.01$
C Ring		
1973-1974	0.04 ± 0.02	0.06 ± 0.03
1976	0.20 ± 0.07	0.22 ± 0.08
A + B Ring		
1973-1974	0.74 ± 0.11	0.84 ± 0.17
1976	0.37 ± 0.05	0.41 ± 0.07
A and B Separated		
B Ring	0.74 ± 0.11	0.84 ± 0.17
A Ring	0.07 ± 0.07*	0.10 ± 0.09*

* Uncertainty does not include uncertainty in B ring optical depth.

the ring brightness temperature corrections have used the same result of 0.04 ± 0.01 for the normalized ring brightness temperature. It is interesting to compare the optical depths in Tables 5 and 7 since they reflect the degree to which the opacity results are affected by the introduction of the C ring. The estimates of the optical depths of the A and B rings are lowered when the C ring is added, and a larger difference between the A and B ring optical depths is required to explain the difference in the combined ring optical depth. The latter effect may not be a real one and might be caused by the correlation between the brightness temperature of the region of the planet blocked by the C ring and that of the region of the planet blocked by the A and B rings. The C ring optical depths in 1973-1974 and 1976 are formally different. However, this difference may not be all that significant in view of the correlations that appear to be taking place. If the results are interpreted literally, they indicate that a single optical thickness C ring will not account for the observed blockage. But if they are taken in the light of the possible correlations, the best that can be said is that it significantly blocks the planetary emission and has an optical thickness of about one-tenth.

Models 3 and 4 show that the C ring is a significant feature in the brightness structure of the microwave radiation from Saturn. The C ring has a brightness temperature that is comparable to that of the A and B rings and may lie somewhere between them. The addition

of the C ring to the Saturn models has caused the A ring to appear brighter relative to the B ring than it did in the previous models that did not include the C ring. This result is expected to be closer to the truth than the previous one since correlations with the unmodeled C ring might have caused the large difference in brightness temperature between the A and B rings. None of the rings show any significant change in brightness temperature as the ring tilt changes. The C ring significantly attenuates the emission from the planet. Although it is difficult to get an accurate figure for its optical depth, because of the correlations with the region blocked by the A and B rings, it is fair to say that the microwave optical depth is consistent with the visible value of about one-tenth. The optical depth estimates for the A and B rings change when the C ring is included in the model fit. Some of this change is in the sense expected when the C ring is included. However, the inconsistent optical depths for the C ring may make the difference between the optical depths of the A and B rings larger than it is. If both model fits with and without the C ring are considered in the estimation of the optical depths and if a normalized ring brightness temperature of 0.04 ± 0.01 is assumed, then the most probable values of the ring optical depths are 0.9 ± 0.2 for the B ring and 0.2 ± 0.2 for the A ring.

(iii) Models to Test for the Presence of Limb-Darkening

In this section a detection of the limb-darkening of the planet is attempted, and its effects upon the other parameters in the models are considered. Briggs (1974) and others have pointed out previously that correlations between unmodeled limb-darkening and the other parameters in the model could produce erroneous results, particularly where the blocked region of the planet is concerned. It is, therefore, important to ascertain whether limb-darkening seriously affects the results relating to the rings. A measurement of limb-darkening also has important implications for the atmosphere of Saturn since limb-darkening contains information about the temperature structure of the atmosphere and the distribution of opacity sources, particularly ammonia. For these reasons, models including the effects of limb-darkening have been fit to the data sets.

Limb-darkening has been approximated by changing the size of the planet in the model fits. This approximation is easily done and has the important effect of moving the zeros of the visibility function in the manner expected from limb-darkening. The limb-darkening that best describes different sized disks is shown in Figure 4. To define this curve, a disk that was limb-darkened according to the equation

$$\frac{I(\mu)}{I(1)} = 1 + D - D\mu \quad ,$$

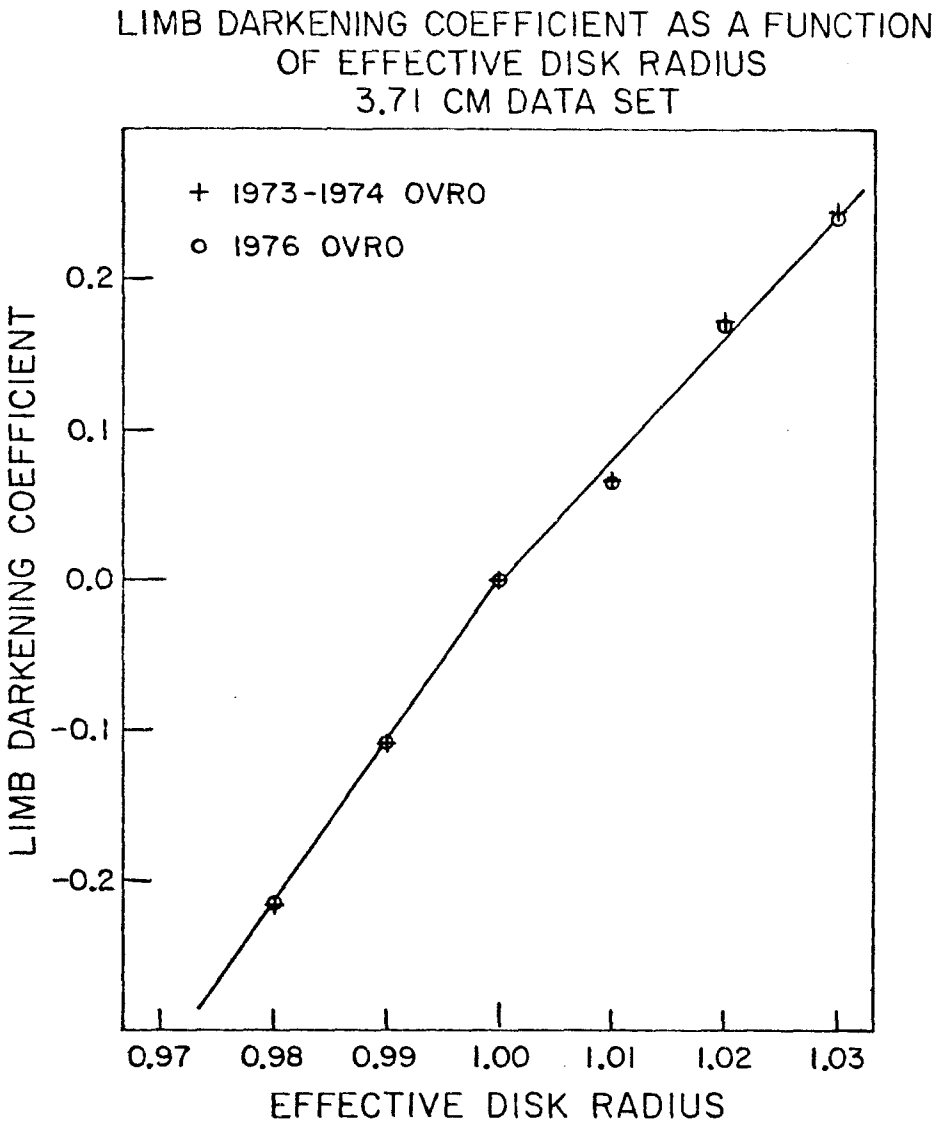

Figure 4 - Results of least squares fit of effective disk radius to limb-darkened disks for the 3.71 cm data sets. The lines shown on the figure only represent an approximation of the measured values and are not a best fit to them in any sense.

where μ is the cosine of the angle of incidence and D is the limb-darkening coefficient, was fit by least squares to a different sized, uniformly bright, disk of the same flux. It was found that the use of either the 1973-1974 or 1976 data sets produced the same dependence, although this is not necessarily true of all possible sets of interferometric data. As can be seen from the figure, limb-dark disks, with $D < 0$, map into slightly smaller disks and limb-bright disks, with $D > 0$, map into larger disks. No limb-darkening at all gives a disk of the proper size. Thus, if limb-darkening is present, it should be detectable by solving for the disk radius that produces the lowest residuals.

Since the radius of Saturn is known imperfectly, there is a range of values of the best fitting disk radius, which shall be called the effective disk radius, that will be consistent with the estimated errors in the determination of the disk radii. This might seen to be a weakness of the method chosen to approximate limb-darkening, but since limb-darkening and planet size appear to be similar, it is a weakness that would be present in any limb-darkening determination. Cook et al. (1973) estimate that the error on the value for the equatorial radius of Saturn is about 0.3% and state that the error on the polar radius is probably greater. Thus, any effective disk radius that is different from the nominal value by on the order of 0.5% or less is within the errors on the nominal value of the disk radius and cannot be used to infer the presence of limb-darkening.

The effective disk radius has been estimated from the 1973-1974 and 1976 data sets by the method known as brute force least squares. This is a convenient way to do least squares model fits which contain one non-linear parameter. In this case, the non-linear parameter is the effective disk radius. The Saturn data were fit to models with different disk radii and the residuals to the model fits were determined. These residuals are then fit to a parabola of the form:

$$S = C_o + C_1 X_R + C_2 X_R^2$$

where S is the sum of the squares of the residuals, X_R is the effective disk radius and the C's are constants to be determined. It follows, by finding the minimum of this curve, that $\hat{X}_R$, the best estimate of X_R, is

$$\hat{X}_R = \frac{-C_1}{2C_2} \quad .$$

It can also be shown that the variance of $\hat{X}_R$, $\sigma^2_{X_R}$ is given by

$$\sigma^2_{X_R} = \sigma^2_{DATA} \quad \frac{1}{C_2} \quad ,$$

where σ^2_{DATA} is the variance of the data set. The variance of the data set is usually taken to be the mean square residuals to the model fit, although this probably leads to an underestimate of the errors.

As the effective disk radius is varied, the other parameters in the model fit are allowed to vary so that the minimum residuals for a

particular effective disk radius are found. The other parameters vary linearly with effective disk radius near the minimum, and this variation is used to correct their errors and correlations for the effect of the effective disk radius parameter. The correction applied to the covariance matrix, P, of the model fit without the variation of disk radius to find the new covariance matrix, P', is given by

$$P'_{ij} = P_{ij} + \frac{dX_i}{dX_R} \frac{dX_j}{dX_R} \sigma^2_{X_R} ,$$

where X_i and X_j are the i^{th} and j^{th} parameters in the model. These corrections are the same as those determined in consider covariance calculations and as in the case of consider covariance, they increase the errors on the parameters since the effect of an error in the disk radius is considered in their estimation.

This method was applied to the 1973-1974 and 1976 data sets and the sum of the squares of the residuals are shown in Figure 5 as a function of the effective disk radius. As can be seen immediately from the residuals, the minimum occurs at about 1.01 for the 1973-1974 data set and 1.00 for the 1976 data set. For the parameters of Model 4, the effective disk radius results are 1.010 ± 0.005 for 1973-1974 and 1.000 ± 0.004 for the 1976 data set. These numbers are formally significantly different and the 1973-1974 results, if taken literally, indicate that the planet is significantly limb-bright. However, in view of the 1976 result, which comes from a stronger data set that is expected to have fewer systematic errors, the 1973-1974

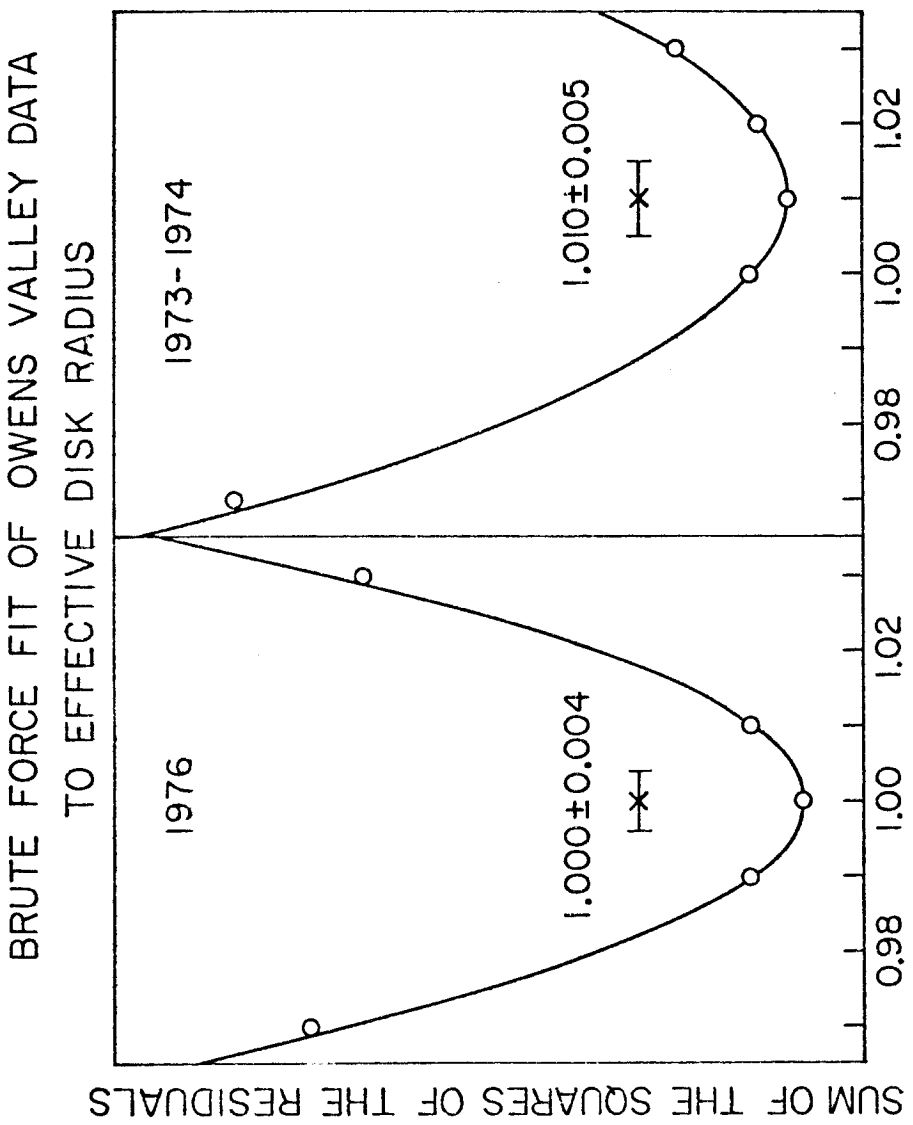

Figure 5 - Sum of the squares of the residuals to the model fits to the 1973-1974 and 1976 Owens Valley data sets plotted as a function of the effective disk radius. The brute force least squares procedure fits a parabola to the lowest three points shown in the figure and uses it to determine the best fitting value of the effective disk radius. The best fitting values are 1.000 ± 0.004 for the 1976 data set and 1.010 ± 0.005 for the 1973-1974 data set.

result is probably not significant. Thus, the best estimate of the effective disk radius, which comes from the 1976 data set, indicates that the planet is not significantly limb-dark. If Figure 4 is used to estimate the limb-darkening coefficient, D, and a conservative value of 1.00 ± 0.01 is assumed for the effective disk radius, then the best estimate of D is 0.0 ± 0.1.

The results of the model fits including the effective disk radius parameter are given in Table 8. Models 5 and 6 contain the same parameters as Models 3 and 4 and a comparison of these models for the 1976 data set shows, as expected, that the brightness temperatures of the various regions do not change. The 1973-1974 data set shows a slight, but less than one sigma, change in the brightness temperature values which is due to the different effective disk radius. This small change indicates that the brightness temperatures are not too dependent upon the effective disk radius since a radius that is two sigma different from the nominal value has caused changes in them that are less than one sigma. This is expected since the correlation coefficients between the effective disk radius and the model brightness temperatures are always less than 0.4 and are far from the largest in the model fits. Thus, the results of the previous model fits are not seriously affected by errors in the effective disk radius and therefore, are not sensitive to limb-darkening on the planet. That no significant limb-darkening was detected also indicates that it does not seriously affect the other parameters.

TABLE 8

RESULTS OF MODELS INCLUDING EFFECTIVE RADIUS (3.71 cm)

	1973-1974		1976	
	Model 5	Model 6	Model 5	Model 6
T_B Planet	168.9 ±1.8 (1.000±0.011)	168.8 ±1.8 (1.000±0.011)	186.0 ± 1.7 (1.000± 0.009)	186.0 ± 1.7 (1.000± 0.009)
Effective Radius	1.010±0.005	1.010±0.005	0.999± 0.004	1.000± 0.004
T_B Planet Blocked by C Ring	150.6 ±9.4 (0.892±0.056)	150.8 ±9.4 (0.893±0.056)	108.0 ±22.1 (0.581± 0.119)	107.5 ±22.2 (0.578± 0.119)
T_B Planet Blocked by A + B Ring	25.5 ±7.7 (0.151±0.046)	26.2 ±7.8 (0.155±0.046)	65.2 ± 9.8 (0.351± 0.053)	65.2 ± 9.8 (0.351± 0.053)
T_B C Ring	6.6 ± 3.2 (0.039± 0.019)	4.9 ±3.9 (0.029±0.023)	9.1 ± 3.3 (0.049 ± 0.018)	8.0 ± 3.7 (0.043 ± 0.020)
T_B B Ring	6.9 ±1.3 (0.041±0.008)	8.7 ±2.8 (0.052±0.017)	7.6 ± 1.3 (0.041 ± 0.007)	9.0 ± 2.5 (0.048 ± 0.013)
T_B A Ring	6.9 ±1.3* (0.041±0.008)	4.9 ±3.0 (0.029±0.018)	7.6 ± 1.3* (0.041 ± 0.007)	5.9 ± 2.8 (0.032 ± 0.015)
T_{DISK}†	168 K	167 K	171 K	170 K
Improvement in Residuals Relative to Model 1 (percent)	2.8	2.9	3.4	3.5

* A and B rings combine into a single ring.

† $T_{DISK} = \frac{\lambda^2}{2k} \times \frac{\text{Model Flux Density}}{\text{Solid Angle of Elliptical Disk with AENA Radii}}$

The addition of limb-darkening to the models does not significantly affect the previous model fitting results and a solution for limb-darkening shows that it is not significantly present. The conclusion that limb-darkening does not affect the ring results is only strictly true for these data sets. It can be imagined that models fit to the data from only one or two interferometric baselines might be significantly affected by limb-darkening. The lack of a significant change in the size of the effective disk from the nominal size in the 1976 data set places interesting limits upon the amount of limb-darkening of Saturn at 3.71 cm and also indicates that the ring results are probably not affected by planetary limb-darkening.

IV. ANALYSIS OF THE 1976 OWENS VALLEY 3.71 cm OBSERVATIONS BY APERTURE SYNTHESIS TECHNIQUES

a) Introduction

In the previous section, models of the radio brightness structure of Saturn and the ring system were discussed. This model fitting analysis is possible since the major features of the brightness structure of Saturn are known and can be specified by a few parameters which may be fit to the observations. Unfortunately, in order to fit such a model to the data, it is necessary to make assumptions about some aspects of the brightness structure which are important to determine.

In the model fitting analysis, the principal assumptions made were the sizes of the model components and their uniform brightness. Of these, the most important to test is the assumption of uniform brightness, since it is unknown if the brightness of the planet or the the rings is uniform. Any non-uniformity would have important implications for the atmosphere and rings of Saturn. Since the nature of any non-uniform brightness is unknown, it is difficult to model satisfactorily and know if any detection by the model fitting process is real. Thus, it is of great importance to determine the brightness structure of the Saturn system in a way that is independent of any model.

In this section, the interferometric observations obtained at the Owens Valley Radio Observatory in 1976 are used to produce a map of the radio emission from Saturn. The technique used to make the map is

known as aperture synthesis, and it produces a map of a radio source that is free from any assumptions about the source's brightness distribution. Unfortunately, the observations made in 1973 and 1974 were not designed for use in an aperture synthesis experiment and therefore, only the 1976 observations have been used in the aperture synthesis analysis.

Aperture synthesis makes use of the Fourier transform relation between the radio brightness structure of a source and the response of a radio interferometer to it. Each observation of a source with an interferometer is a sample of the complex, two dimensional, Fourier transform of the source's brightness distribution. If this Fourier transform is sufficiently well sampled, by making observations on many interferometer baselines, it may be inverted to produce a map of the radio source. This map will have a spatial resolution on the order of 1/D, where D is the longest interferometer baseline measured in wavelengths, which makes it similar to a map made with a single radio telescope that is D wavelengths across. It will also contain no assumptions about the source's brightness structure. Therefore, since aperture synthesis is independent of any model of the brightness structure of the Saturn system, it offers a means to search for unrecognized structures as well as a means to confirm the results of the model fitting analysis.

b) Aperture Synthesis Procedures

(i) The Principal Aperture Synthesis Formulas

Since some readers may be unfamiliar with interferometry and,

in particular, aperture synthesis mapping of radio sources, this section will be devoted to a discussion of the production and handling of aperture synthesis maps. Very extensive recent reviews of the subject are given by Brouw (1975) and Fomalont and Wright (1974). For the present purposes, however, it is necessary only to review the principal aperture synthesis formulas and the steps involved in producing an aperture synthesis map.

An interferometer responds to the Fourier transform of the source's brightness structure. This Fourier transform is called the visibility function, V, and it is given by

$$V(u,v) = \int_{-\infty}^{\infty}\int_{-\infty}^{\infty} I(x,y)\, e^{+i2\pi(ux+vy)}\, dx\, dy \quad . \qquad (1)$$

In equation (1), the x and y variables are in units of radians and make up a left-handed cartesian coordinate system on the sky relative to an arbitrary position which is often taken to be the centroid of the emission from the source. In the case of Saturn, the map center has been defined to be the position of the center of mass of the planet given by the American Ephemeris and Nautical Almanac. The x and y axes are usually taken to be in the direction of increasing right ascension and declination. However, for the Saturn maps these axes have been rotated by 7 degrees so that they correspond with the major and minor axes of the ring system. The variables u and v are the projection of the interferometer baseline, in units of wavelengths, onto the x-y coordinate system at the time of a given observation. For a given separation of the antennas, u and v change

continuously during the day as the baseline-source geometry changes. $I(x,y)$ is the intensity of the source at the position x,y, but it is not the true intensity since, in general, it is modified by the antenna pattern of the primary elements of the interferometer. However, in the maps to be discussed here, this modification is not important since Saturn is much smaller than the primary element beam.

It is clear from equation (1) that the brightness structure, $I(x,y)$, may be obtained by Fourier transforming the interferometer's measurements of $V(u,v)$:

$$I(x,y) = \int_{-\infty}^{\infty} \int_{-\infty}^{\infty} V(u,v)\ e^{-i2\pi(ux+vy)}\ du\ dv \quad , \tag{2}$$

Unfortunately, it is not possible to perform the transformation of equation (2) since it is not possible to obtain measurements of the visibility function at all points u,v. All practical interferometers sample only pieces of the u-v plane and the resulting maps of the source are affected by this sampling. If a sampling function, $S(u,v)$, is defined such that S is equal to 1 where an observation is made and equal to 0 elsewhere, then the map obtained by the interferometer sampling according to S is $I'(x,y)$ and given by

$$I'(x,y) = \int_{-\infty}^{\infty} \int_{-\infty}^{\infty} S(u,v)\ V(u,v)\ e^{-i2\pi(ux+vy)}\ du\ dy \ . \tag{3}$$

A different way to view the effect of S upon the map is to use the convolution theorem which states:

$$\mathcal{F}(f \cdot g) = \mathcal{F}(f) * \mathcal{F}(g) \quad ,$$

where $\mathcal{F}$ represents the operation of taking a Fourier transform, $*$ represents a convolution and f and g are two functions. Application of this theorem to (3) leads to

$$I'(x,y) = \left[\int_{-\infty}^{\infty} \int_{-\infty}^{\infty} S(u,v)\ e^{-i2\pi(ux+vy)} du\ dv \right] * I(x,y) \quad .$$

If $B(x,y)$ is defined according to

$$B(x,y) = \int_{-\infty}^{\infty} \int_{-\infty}^{\infty} S(u,v)\ e^{-i2\pi(ux+vy)}\ du\ dv \quad ,$$

then (3) may be written as

$$I'(x,y) = B(x,y) * I(x,y) \qquad (4)$$

and it is seen that the map obtained by an interferometer sampling according to $S(u,v)$ is given by a convolution of the true map, I, with the Fourier transform of the sampling function, S. This is an exact analogy to a map produced by a conventional radio telescope where the map made is just the true brightness convolved by the antenna beam pattern. Thus, the function B fills the role of the beam pattern of a conventional, filled aperture, telescope and is, therefore, referred to as the synthesized beam of the aperture synthesis telescope.

The synthesized beam is often characterized by high sidelobe levels that accompany the uneven sampling of the u-v plane by an interferometer. This is particularly true for sources at low declinations, such as planets, since a single interferometer does not sample a very large portion of the u-v plane of a source at a low

declination. In the case of the 1976 Owens Valley data, the u-v coverage of Saturn obtained by the 13 interferometer spacings is shown in Figure 1. Figure 6 shows the synthesized beam which is a Fourier transform of the sampling. The synthesized beam contains a pair of negative sidelobes at a level of about 35% of the peak response as well as a number of smaller sidelobes at about the 15% level. A number of the sidelobes to the north and south of the main response are sufficiently far removed from the center of the beam that they do not interfere with the map produced. Even so, the sidelobes that do exist in the vicinity of the main beam cause a good deal of distortion of the brightness structure of Saturn and the rings. This distortion may be seen in Figure 7 which is the result of Fourier transforming the Owens Valley observations. This map represents the true brightness distribution of Saturn convolved by the synthesized beam. The deflection at a point in the map is in units of Jansky per beam area and represents the flux density that a point source at that position requires to produce the observed deflection.

(ii) The Procedure CLEAN

In order to search for low level brightness structures, such as those expected for Saturn's rings, in a map like Figure 7, it is necessary to devise a scheme for minimizing the effects of the sidelobes of the synthesized beam. Schemes for achieving this goal are discussed by Högbom (1974) who describes the widely accepted method known as CLEAN. CLEAN is a procedure which uses certain a priori

Figure 6.- Contour map of the synthesized beam of the 1976 OVRO aperture synthesis experiment. The contour levels are 90%, 70%, 50% 30%, 10%, -10%, and -30% of the peak response. The interval between the tick marks at the edge of the map is 10 arcsec for Saturn at the standard distance of 8 AU.

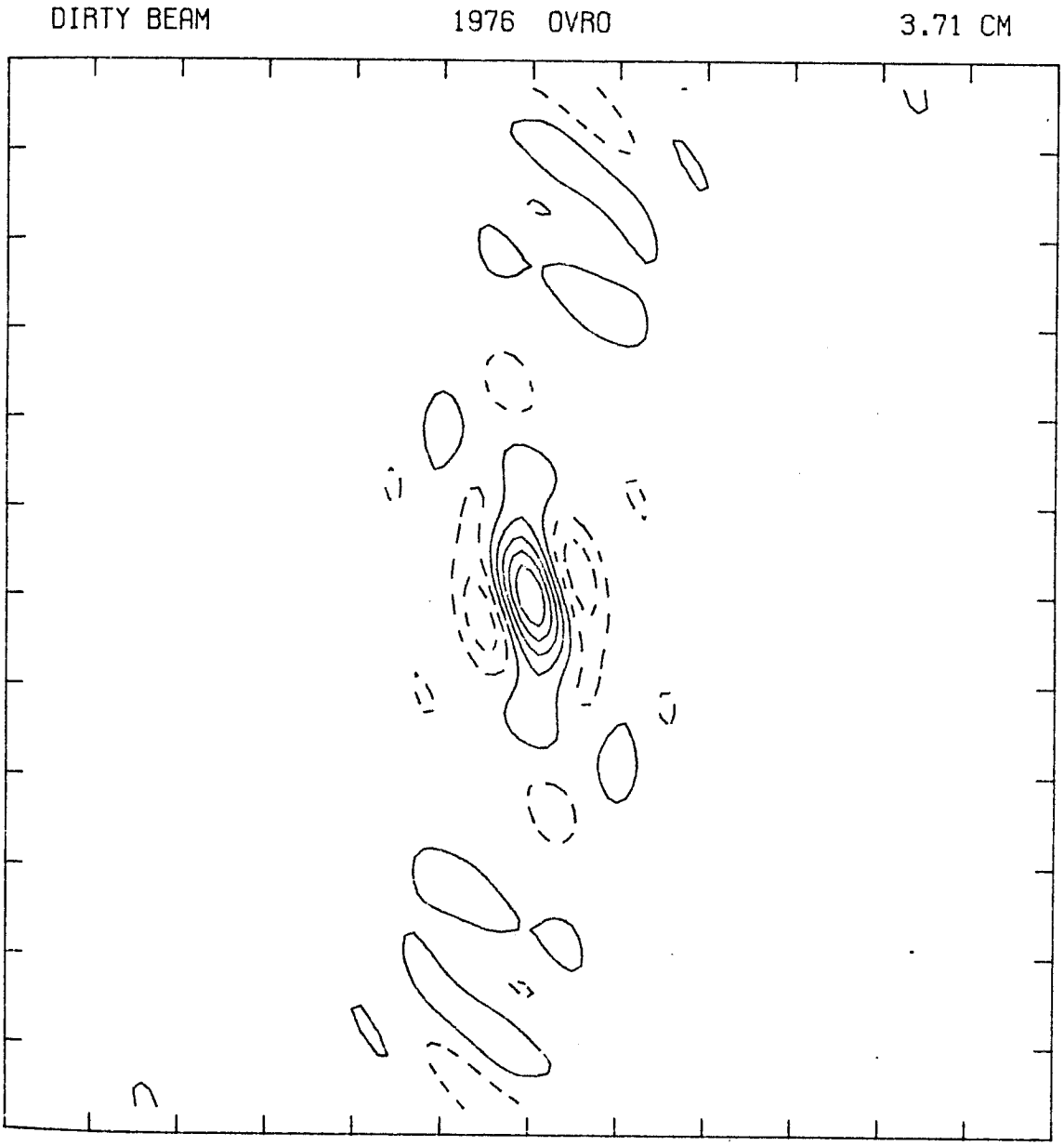

Figure 6

Figure 7.- 1976 OVRO aperture synthesis map of Saturn. The map represents the convolution of the true brightness structure of Saturn with the synthesized beam shown in Figure 6. The peak response in the map is 0.29 Jy, and the contour levels are 90%, 70%, 50%, 30%, 10%, -10%, and -30% of the peak response. Saturn is at the center of the map and the horizontal (x) and vertical (y) axes of the map are aligned with the major and minor ring axes, respectively. x increases to the left and is toward Saturn's east limb, and y increases to the top and is toward its north limb. The interval between the tick marks at the edge of the map is 10 arcsec for Saturn at the standard distance of 8 AU.

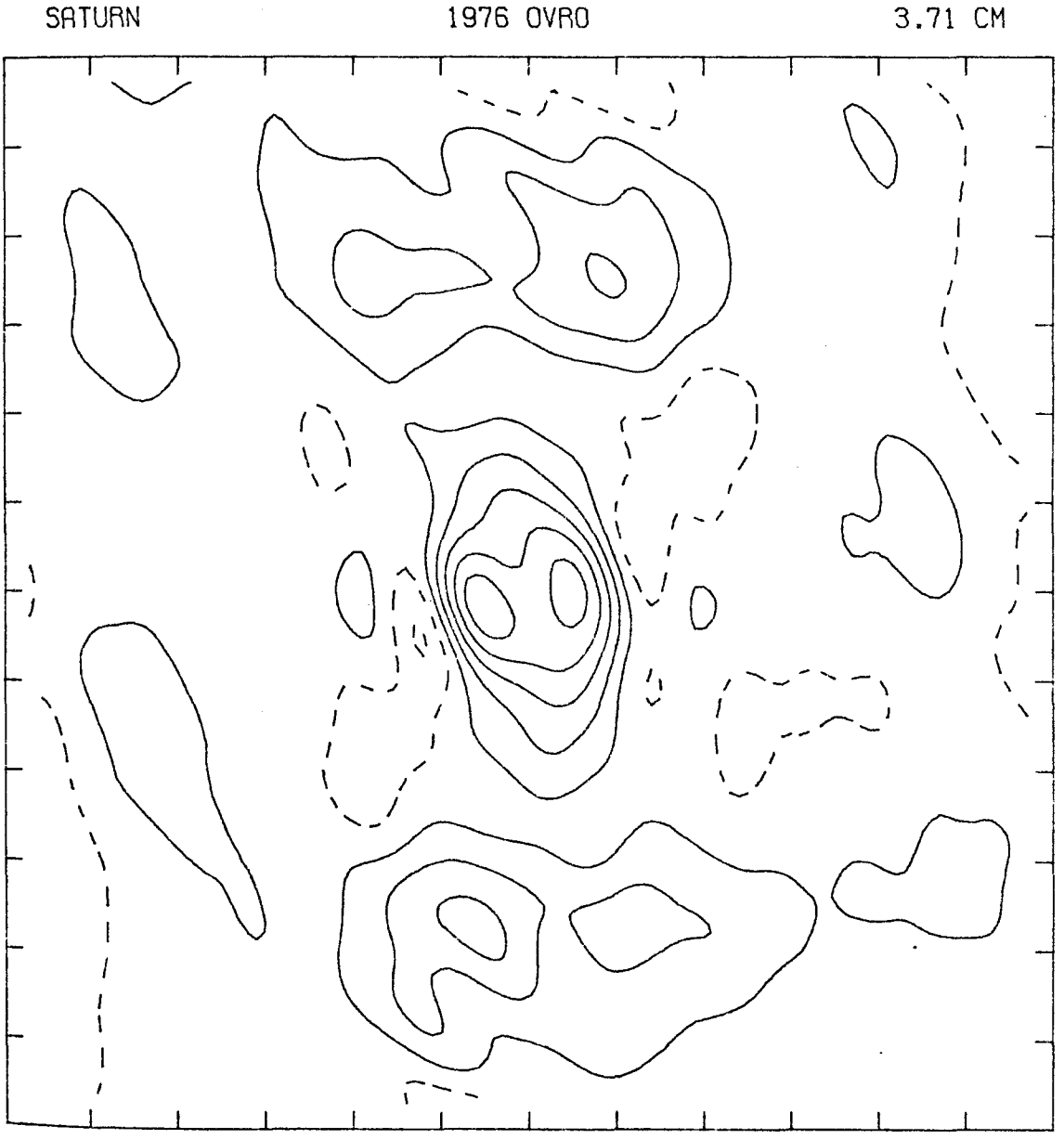

Figure 7

information about the aperture synthesis experiment, such as the size of the source and the known shape of the synthesized (DIRTY) beam, to discriminate between those deflections in the (DIRTY) map caused by sidelobes of the DIRTY beam and those deflections caused by actual structures in the source. CLEAN attempts to find a collection of point sources which, when convolved with the DIRTY beam, will give the DIRTY map. The positions of the point sources may be constrained to lie within a certain region of the overall map. This constraint is particularly useful for sources, such as planets, where it is fairly certain which region of the sky contains all of the source's emission. The point sources are chosen by CLEAN in an iterative fashion. The DIRTY map is scanned to find the peak deflection, and since some fraction of this deflection is almost certain to be real, the response of the DIRTY beam to a fraction of the deflection is removed from the map. The DIRTY map is then scanned again and the process is repeated many times until some number of iterations is exceeded or the size of the component removed becomes less than some value. Practically, it has been found that there is a point past which further cleaning makes no difference to the map. After the iteration cycle has been performed a sufficient number of times, the point sources which have been removed from the map are returned to it in the form of the response of a clean, sidelobe free, beam to the point source. The CLEAN beam is typically a gaussian of the size and shape of the main lobe of the DIRTY beam.

In this study, CLEAN has been used to deconvolve the DIRTY Saturn maps and produce clean, sidelobe-free maps. The CLEAN map, shown in Figure 8, was produced by removing 500 point sources from an area the size of the Saturn system. The deflections in the CLEAN map are given in units of degrees Kelvin since they represent the convolution of the true brightness temperature structure of Saturn with the CLEAN beam. This value is not, in general, the true brightness temperature of a source component, but it is closely related to the antenna temperature in a conventional, filled-aperture map of a radio source. Therefore, the quantity represented in the CLEAN maps shall be called the synthesized beam antenna temperature, or beam temperature, to distinguish it from the brightness temperatures of the source components.

The cleaning area was a 50 x 20 arcsec box centered on the geometric center of Saturn. These dimensions and all of the dimensions quoted in this section refer to Saturn at a distance of 8 AU. At each iteration, 30% of the peak deflection was removed from the map and then, after all iterations were completed, returned as the response of a gaussian CLEAN beam. The half power beam width of the gaussian CLEAN beam was 8 arcsec by 15 arcsec and the major axis of the beam was aligned with the central meridian of Saturn. This special orientation of the CLEAN beam makes the interpretation of the resulting maps easier. As can be seen from the map in Figure 8, the CLEAN map presents a much more satisfactory appearance and is essentially free of the false deflections due to sidelobes of the

Figure 8 - CLEAN 1976 OVRO aperture synthesis map of Saturn. The map of Figure 7 has been deconvolved with the synthesized beam of Figure 6 and the result is reconvolved with a gaussian beam. The dimensions (HPBW) of the gaussian, CLEAN beam are 8 arcsec in the horizontal (x) direction and 15 arcsec in the vertical (y) direction. The deflections in the map are given in the units of brightness temperature and represent the brightness temperature of the source averaged over the CLEAN beam. The contour values are 5 K, 10 K, 25 K, 50 K, 75 K, 100 K, and 125 K. Dashed contours represent negative values. Saturn is at the center of the map and the x and y map axes are aligned with the major and minor ring axes, respectively. x increases to the left and is toward Saturn's east limb, and y increases to the top and is toward its north limb. The interval between the tick marks at the edge of the map is 10 arcsec for Saturn at the standard distance of 8 AU.

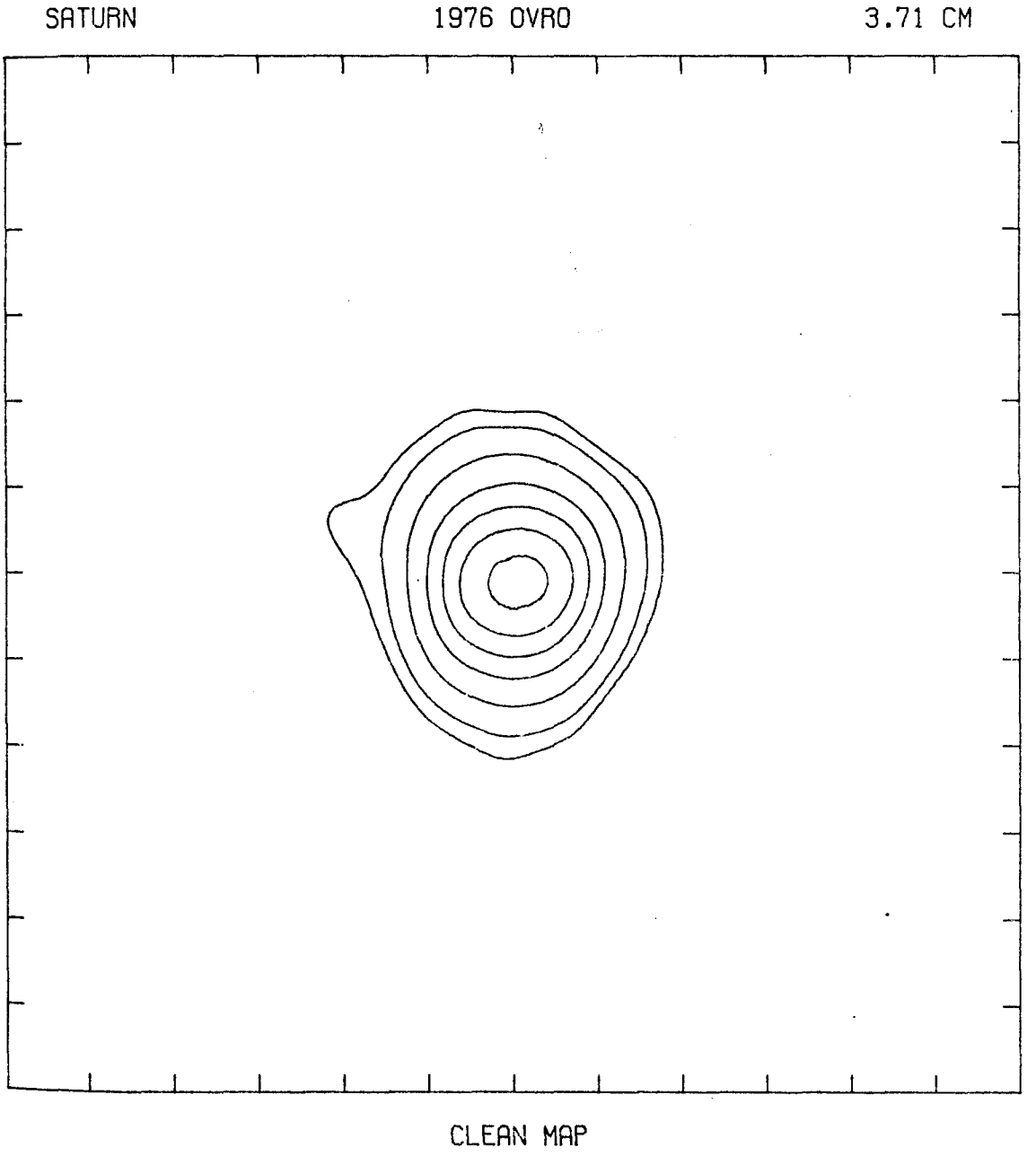

Figure 8

DIRTY beam. However, the map is probably not totally free of such false deflections and therefore, some caution must be observed in the interpretation of the cleaned maps.

(iii) Sensitivity of an Aperture Synthesis Map

In addition to false deflections in the maps due to sidelobes of the DIRTY beam, there will also be false deflections due to noise on the measured visibility function. This noise may be considered to be of two types. The first type is random, statistical noise due to the measurement of the signal from Saturn in the presence of the receiver noise. The second kind is non-random noise due to imperfect calibration and errors in the path length between the two elements of the interferometer due to irregularities in the atmosphere. The random noise due to receiver noise is given, in terms of beam temperature in the aperture synthesis map, by Fomalont and Wright (1974) to be

$$\Delta T_{B_{RMS}} = 2 \frac{T_s}{\sqrt{\Delta\nu t}} \frac{1}{A} \frac{\lambda^2}{\Omega_{syn}} \quad , \tag{5}$$

where T_s is the system temperature, $\Delta\nu$ the bandwidth, t the integration time, A the effective area of a primary element, λ the wavelength and Ω_{syn} the solid angle of the synthesized beam. With the parameters appropriate to the observations at the Owens Valley, the RMS deflection should be about 1 K for the 8 x 15 arcsec (at the standard distance of 8 AU) CLEAN beam. If a larger CLEAN beam is used, say a circular 15 arcsec beam, then the RMS deflection is reduced to about 0.5 K. Thus, extra sensitivity may be achieved by sacrificing some of

the resolution available. In this study, both high resolution maps using the 8 x 15 arcsec CLEAN beam and high sensitivity maps using the 15 arcsec circular CLEAN beam have been produced since they perform complementary functions.

The non-random component of the noise in an aperture synthesis map cannot be easily computed from simple formulas since it depends upon the phase stability of the interferometer and the characteristics of the atmosphere at the observing site. The best method for estimating the noise due to these errors is to look at the level of the deflections in the map away from the source and estimate the RMS deflection. This parameter has been found to be a good estimate of the noise level due to atmospheric effects (Hinder and Ryle, 1971) and, to the extent that the phase instabilities of the interferometer are random, should be a good estimate of their noise level as well. A principal difference between the atmospheric noise in the map and the noise due to systematic phase drifts is that the phase drift noise will tend to produce a pair of antisymmetric deflections in the map (Brouw, 1975) whereas the atmospheric noise produces deflections that are randomly positioned (Hinder and Ryle, 1971). Thus, the level and arrangement of the deflections in the map away from the source are the best means to judge the noise level in the aperture synthesis map.

(iv) Removal of the Response to the Planet

It is evident from Figure 8 that the weak features in the map that are due to the rings are difficult to see in the presence of the strong emission from the planet. For this reason, the response to

the planetary emission must be removed from the map. This was accomplished by removing the response of a uniformly bright elliptical disk from the measured visibility function and Fourier transforming and cleaning the result in the manner of Figure 8 using a 8 x 15 arcsec CLEAN beam. The resulting map, which is shown in Figure 9, was produced by removing a 20.62 x 18.78 arcsec disk whose brightness temperature was 175 K. These dimensions are the same as those used in the model fitting analysis of Part III. The uniform disk brightness temperature was chosen to be 175 K in order to make it roughly consistent with the values obtained in this work and by other interferometric observations at 3.71 cm (Briggs, 1974; Cuzzi and Dent, 1975). This brightness temperature is much less than the value of 186 K found in Part III by model fitting to this data set. However, since the main purpose of the disk subtraction map is to make the features due to the rings more visible and since the maps are produced in order to be independent of the model fitting process, the value of 175 K is appropriate.

The map shown in Figure 9 contains features which are likely to be caused by the presence of the rings. These features will be discussed in greater detail in the next section. Although the procedures used to produce this map are extensive, they maintain the important feature that they are free from any model of the radio emission from the rings. The principle assumptions that have gone into the disk subtraction map are:

Figure 9 - CLEAN 1976 OVRO aperture synthesis map of Saturn with the response to a uniformly bright, 175 K disk removed from the center of the map. The dimensions of the disk are the same as those used in the model fitting analysis. The HPBW of the CLEAN beam is 8 arcsec in the horizontal (x) map direction and 15 arcsec in the vertical (y) direction. The deflections in the map are in units of brightness temperature and represent the brightness temperature of the source averaged over the CLEAN beam. The contour values are 5 K, 2 K, -2 K, -5 K, -10 K, -15 K, -20 K. Dashed contours represent negative values. Saturn is at the center of the map and the x and y map axes are aligned with the major and minor ring axes, respectively. x increases to the left and is toward Saturn's east limb, and y increases to the top and is toward its north limb. The interval between the tick marks at the edge of the map is 10 arcsec for Saturn at the standard distance of 8 AU.

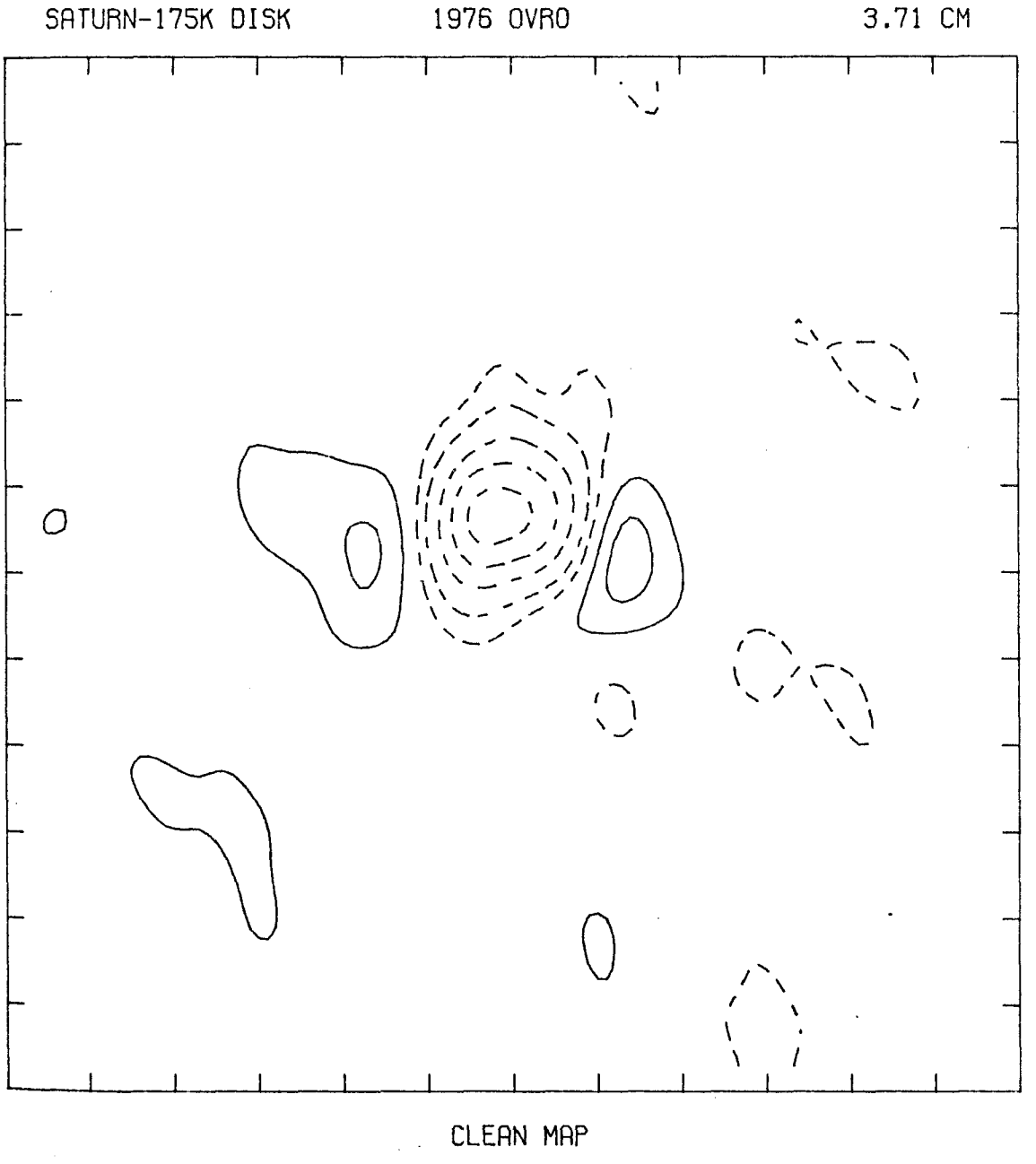

Figure 9

1) The map is centered on the position of the center of mass of Saturn.

2) The emission from the Saturn system comes from an area which includes the visible disk and rings.

3) The subtracted disk is of the correct size and brightness.

Of these assumptions, (1) is potentially the most dangerous, since, if the map is not centered upon Saturn, the removal of a uniform disk from the map will leave behind features in the map due to the offset that may be confused with features due to the rings. The position of Saturn is determined from the geocentric ephemeris of the American Ephemeris and Nautical Almanac , and this position is thought to be accurate to better than one-half arcsec.

An additional source of error in the position of the map center is an error in the position of the calibrator used for the 1976 3.71 cm observations, OJ287. The map center is determined by observations of a radio source whose position is known. These observations assumed a position for OJ287 of:

$$\alpha\ (1950) = 8^h\ 51^m\ 57\overset{s}{.}258$$

$$\delta\ (1950) = 20^\circ\ 17'\ 58\overset{''}{.}68$$

which is in good agreement with the measurements of several observers (Blake, 1970; Smith, 1970; Couper, 1972; Cohen, 1972).

It should be noted, however, that errors in the range of one or two tenths of a second of arc are possible. All things considered, errors in the position of the map center of one-half arcsec or less are quite plausible and these would have the greatest consequences

of all of the assumptions used in the production of Figure 9. These consequences will be considered in great detail in the next section.

The other two assumptions have far less serious consequences for the disk subtraction map. The assumption that all of the emission is coming from the CLEAN box around the visible planet and rings is not a strong one since no emission is expected from outside the ring system. Even if significant emission were coming from outside the cleaning box, it would not be removed by the cleaning process and would appear in the CLEAN maps. This is because, in general, the unexpected emission would not be at a position where it would be removed by subtraction of the DIRTY beam response to features inside of the cleaning box. Finally, the shape and brightness of the disk subtracted from the map do not appear to be critical assumptions. The disk size and shape are accurate to about one percent and errors in these parameters do not strongly alter the appearance of the maps, as do the position errors discussed previously. The effects of limb-darkening have been investigated by the model fitting process and have been found to be undetectable. Thus, limb-darkening should not affect the disk subtraction maps seriously. The brightness temperature of the subtracted disk does alter the absolute level of the contours in the map, but such an error does not strongly affect the deflections due to the rings. In any event, the effects of errors in the disk brightness temperature are fairly easily discovered and corrected, as will be seen in the next section.

It is unfortunate that any assumptions have to be made in order to produce an aperture synthesis map of the radio radiation from the rings. The goal of this study, however, is to produce a map which is as free as possible from the effects of such assumptions, and this goal has been realized, since the assumptions contained in these maps do not affect them strongly and their accuracy is fairly easily checked. Thus, the aperture synthesis analysis allows a search for new brightness features in the radio emission from Saturn as well as a confirmation of the features included in the model fitting analysis.

c) Results and Discussion of the Aperture Synthesis Analysis

(i) Disk Subtraction Maps

The principal result of this aperture synthesis study of the Saturn system is the map shown in Figure 9. This map is reproduced in Figure 10A along with an outline of the planet and the combined A and B rings as seen from earth at the time of the observations. This map has been cleaned with an 8 x 15 arcsec beam (dimensions refer to Saturn at the standard distance of 8 AU) which provides the maximum amount of resolution available in the 1976 Owens Valley data set. The map's strongest feature is a negative one approximately centered upon the position where the rings cross in front of the planet. The negative feature appears because the rings have a significant optical thickness and a very low intrinsic brightness. Thus, the intensity of the emission from the region where the rings block the planet is essentially due to planetary emission that is

Figure 10A - CLEAN 1976 OVRO aperture synthesis map of Saturn with the response to a uniformly bright, 175 K disk removed from the center of the map. The dimensions of the disk are the same as those used in the model fitting analysis. An outline of the planet and the combined A and B ring as seen at the time of the observations is shown for comparison. The HPBW of the CLEAN beam is 8 arcsec in the horizontal (x) map direction and 15 arcsec in the vertical (y) direction. The deflections in the map are in units of brightness temperature and represent the brightness temperature of the source averaged over the CLEAN beam. The contour values are: 6K, 4K, 2K, -2K, -4K, -6K, -10K, -15K, and -20K. Dashed contours represent negative values. The interval between tick marks at the edge of the map is 10 arcsec for Saturn at the standard distance of 8 AU.

Figure 10B - CLEAN 1976 OVRO aperture synthesis map of Model 3, which is described in Part III. This map of the best fitting model was produced in exactly the same way as the map of the data, shown in Figure 10A. The beam, contour levels, and scale of the map are identical to those in Figure 10A.

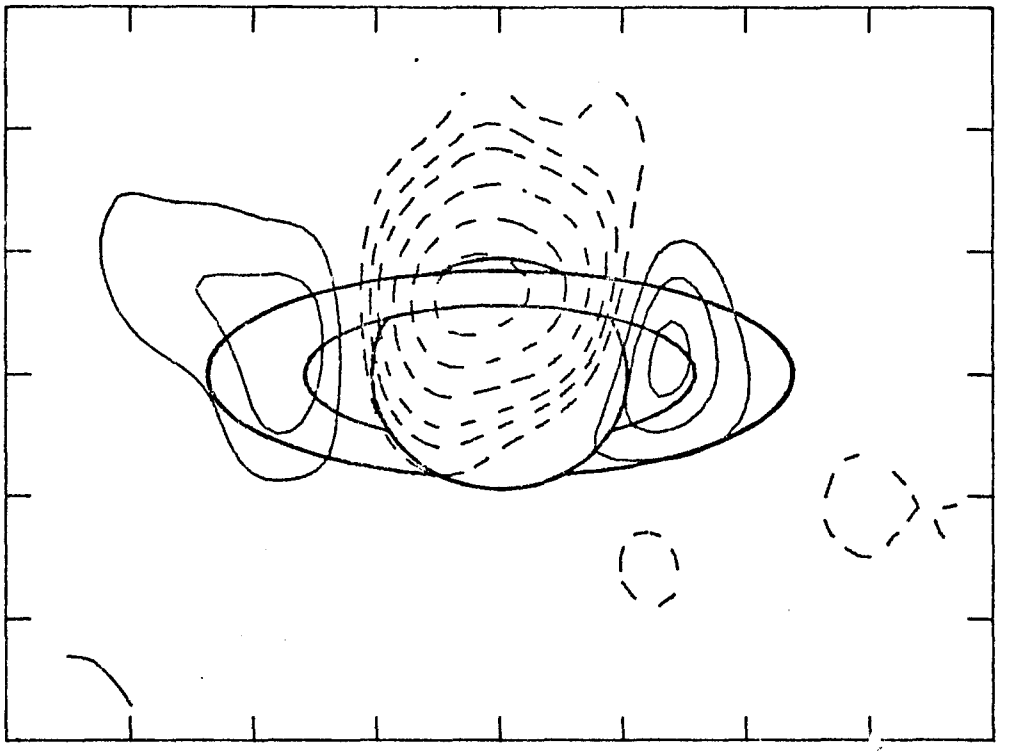

Figure 10A

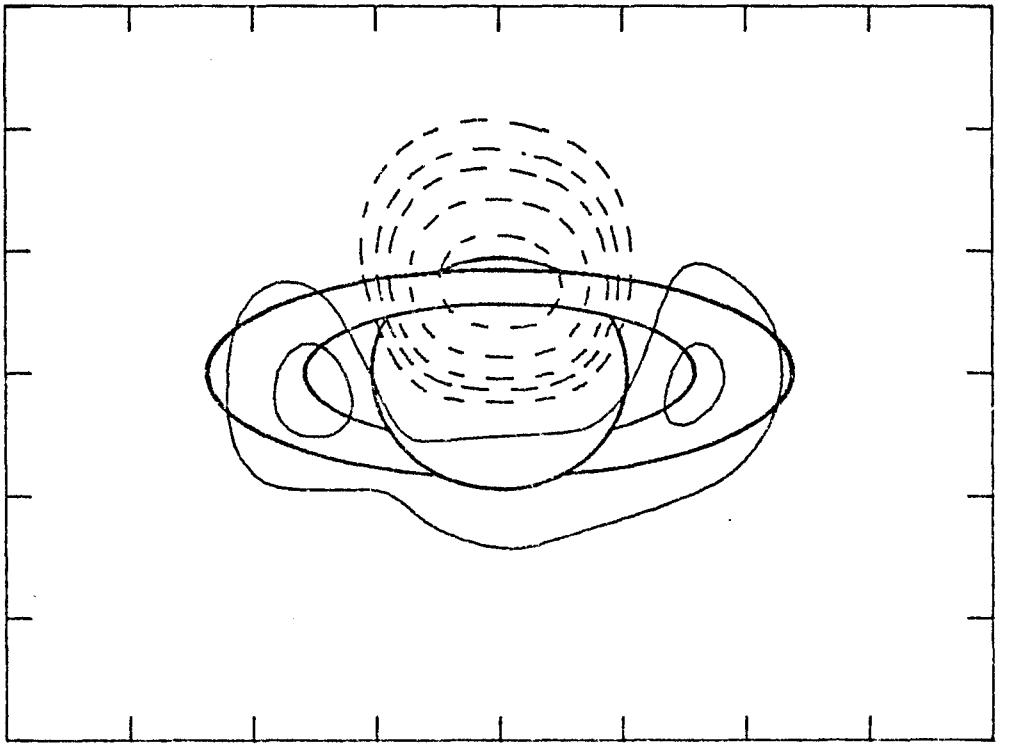

Figure 10B

attenuated by the rings. Since a uniformly bright disk was removed from the map, too much flux was removed from the blocked region, and it appears as a negative feature. The other features in the map that appear to be real are positive deflections of about the same size that appear on either side of the large negative deflection. These deflections are at the position expected for radiation from the rings, and they are of approximately the size expected based on the model fitting results of this study and others. Thus, their presence indicates a small but significant amount of radio radiation from the rings.

The map in Figure 10A agrees quite well with what might have been predicted from the model fitting results of this study and others and is a strong indication of their basic soundness. There are, however, some ways in which the results of model fitting and aperture synthesis do not quantitatively agree. It is these aspects of the maps that should be most carefully examined since they promise to extend the knowledge gained from model fitting to encompass yet unknown aspects of the radio emission from Saturn and the rings.

In order to compare the results of the model fitting analysis to the aperture synthesis maps, a map of one of the models fit to the data in Part III, Model 3, is shown in Figure 10B. Model 3 consists of all of the features which have been found by the model fitting analysis to be significant features of the radio brightness structure of Saturn. It consists of the combined A and B ring, the C ring, the region of the planet blocked by the combined A and B ring, the

region of the planet blocked by the C ring and the region of the planet that is not blocked by any ring. The best fit brightness temperatures of these regions are given in Table 6. The model map of Figure 10B has been produced in exactly the same manner as the map of the data in Figure 10A. The visibility function of Model 3 at the points of observation has been Fourier transformed and cleaned by the same programs used to produce Figure 10A, and its clean appearance is a fine example of the effectiveness of CLEAN. The model map is quite similar to the data map. However, there are some obvious descrepancies particularly in the region of the unobscured planet. A data and model map produced with the larger 15 arcsec circular CLEAN beam and shown in Figures 11A and B show essentially the same results.

It is often difficult to appreciate an aperture synthesis map on the basis of contour maps alone. For this reason, Figure 12 shows plots of horizontal cross sections of the map in Figure 10A. The positions of the cross sections are shown in Figure 13A. The cross section plots allow for a better appreciation of what features in the map are real than do the contour maps. The negative feature, which is due to the blockage of the planetary emission by the rings, and the positive features to either side that are due to the rings are clearly above the surrounding noise level. The negative feature is not symmetric about the center of the map, as is expected from models of it, and it appears to be shifted to the east (in the direction of increasing right ascension). The deflections due to the rings are

Figure 11A - CLEAN 1976 OVRO aperture synthesis map of Saturn with the response to a uniformly bright, 175 K disk removed from the center of the map. The dimensions of the disk are the same as those used in model fitting analysis. An outline of the planet and the combined A and B ring as seen at the time of the observations is shown for comparison. The HPBW of the CLEAN beam 15 arcsec in the horizontal (x) map direction and 15 arcsec in the vertical (y) direction. The deflections in the map are in units of brightness temperature and represent the brightness temperature of the source averaged over the CLEAN beam. The coutour values are: 2K, -2K, -4K, -6K, -10K, and -15K. Dashed contours represent negative values. The interval between tick marks at the edge of the map is 10 arcsec for Saturn at the standard distance of 8 AU.

Figure 11B - CLEAN 1976 OVRO aperture synthesis map of Model 3, which is described in Part III. This map of the best fitting model was produced in exactly the same way as the map of the data, shown in Figure 11A. The beam, contour levels, and scale of the map are identical to those in Figure 11A.

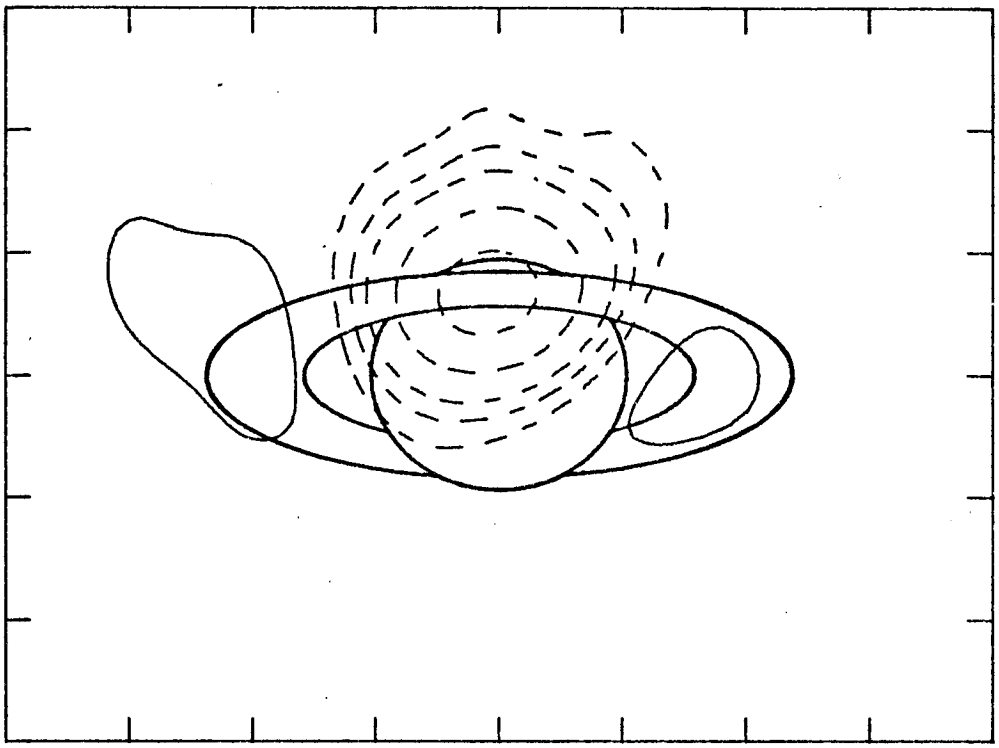

Figure 11A

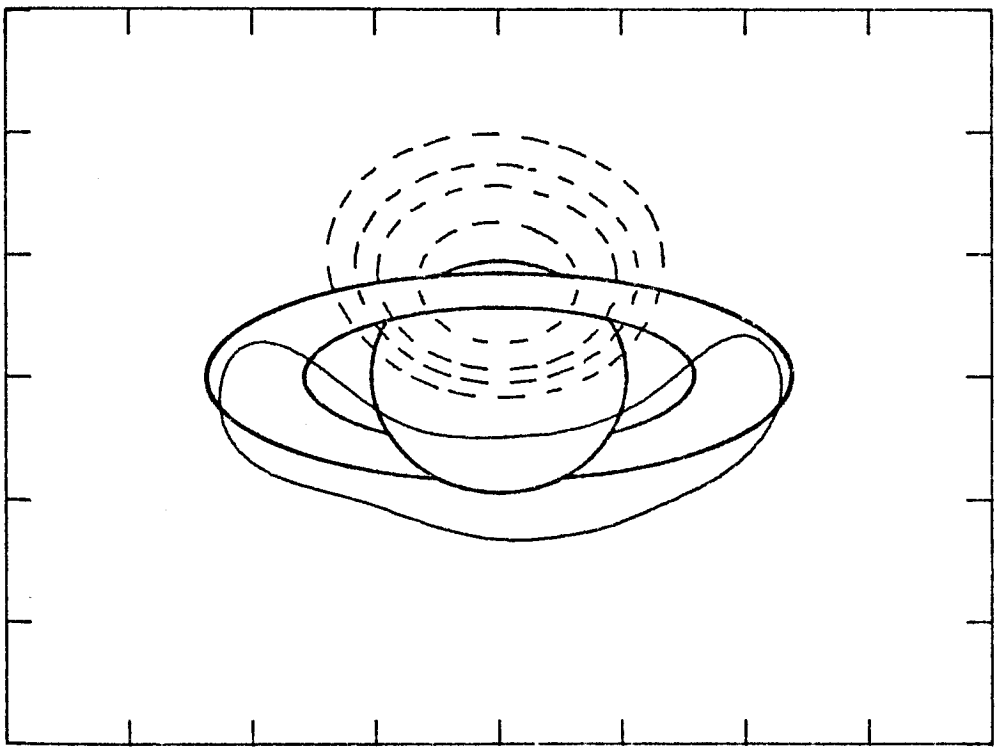

Figure 11B

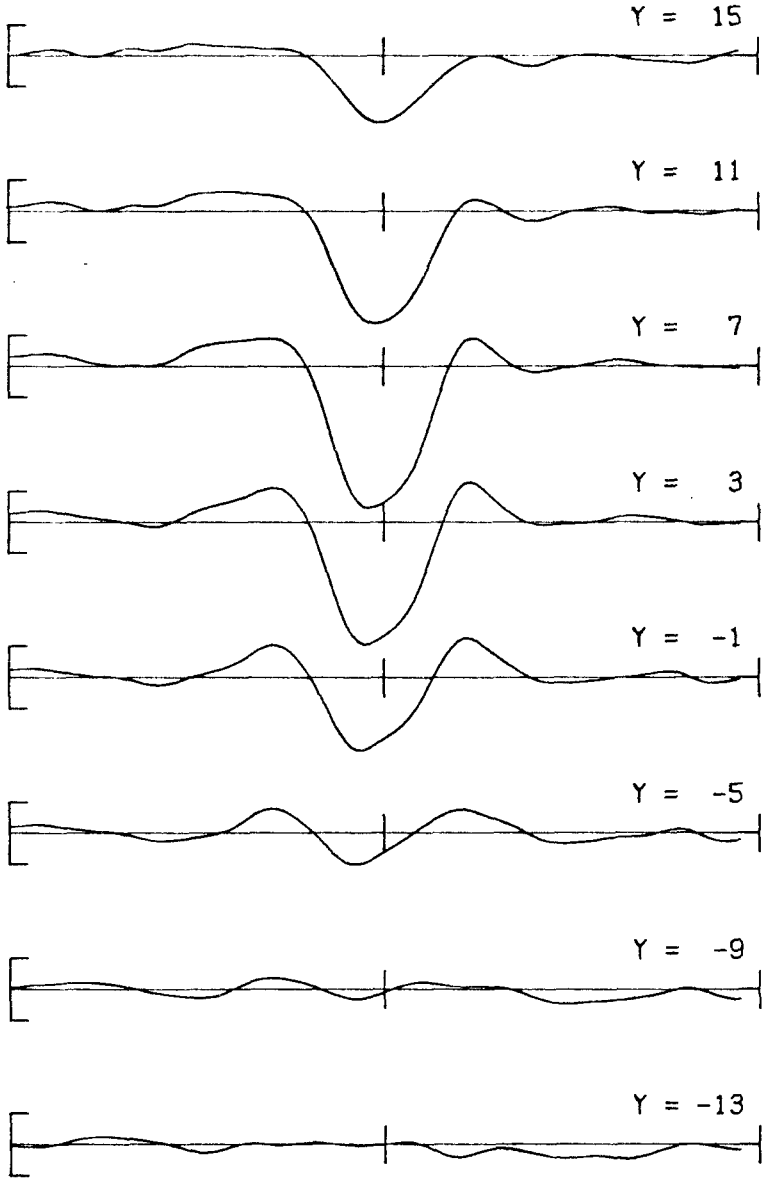

Figure 12 - Horizontal (east-west) cross sections through the 1976 OVRO disk subtraction map shown in Figure 10A. The positions of the cross sections with respect to Saturn are shown in Figure 13A. The horizontal length of the cross sections is 2 arcmin for Saturn at the standard distance of 8 AU. The vertical scale to the left of each cross section represents ±5 K of brightness temperature averaged over the CLEAN beam.

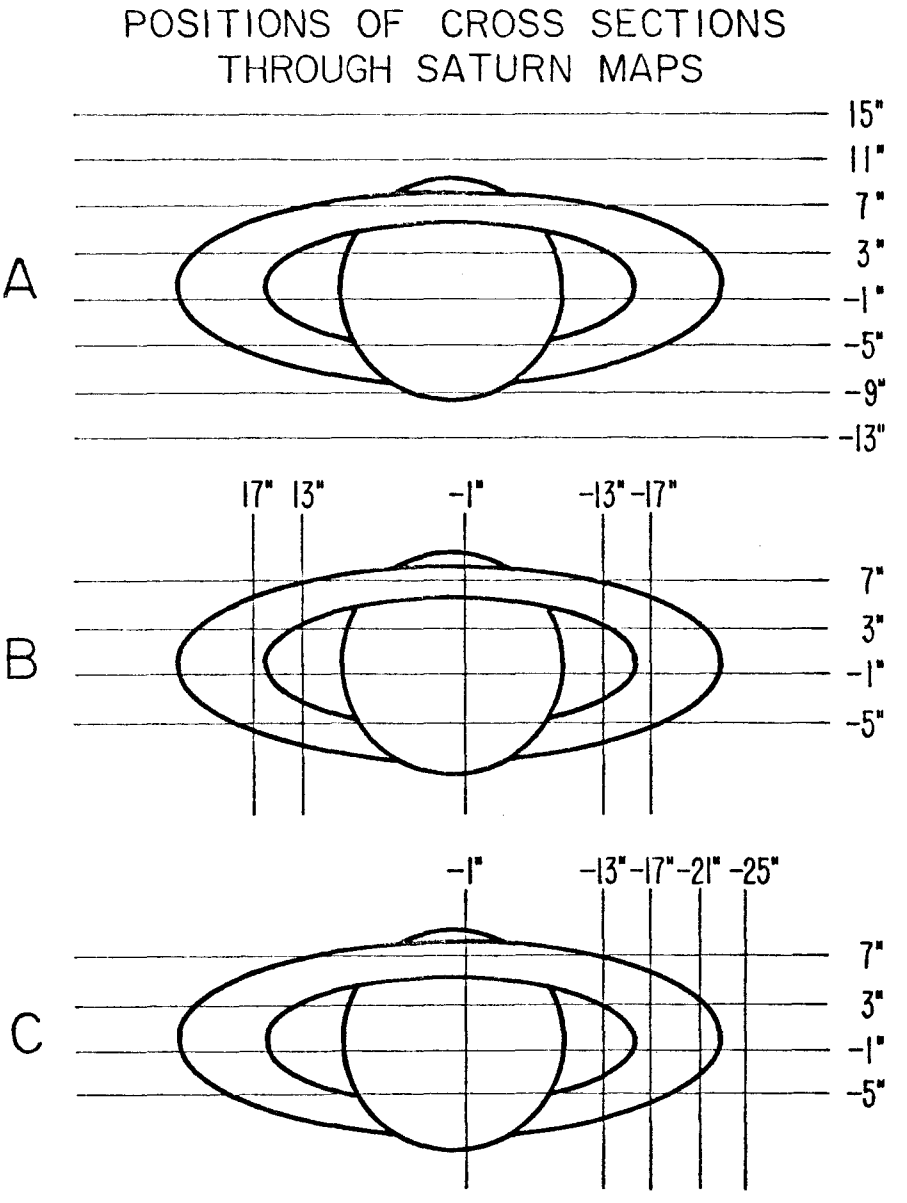

Figure 13 - Positions of cross sections with respect to Saturn. Dimensions on the figures are in arcsec for Saturn at the standard distance of 8 AU. Figure 13A gives the positions of the cross sections shown in Figure 12 and Figure 17. Figure 13B gives the positions of the cross sections shown in Figure 14. Figure 13C gives the positions of the cross sections shown in Figure 15.

of about the same size although the eastern deflection appears broader than the western one. The peak deflections due to the rings are not symmetric about the map center and appear to be shifted to the east by about two or three arcsec. It appears that the map would be symmetric about the center if it were shifted to the west by two or three arcsec, although such a shift is far greater than the likely errors in the position of Saturn. Thus, it is likely that the apparent offset has another cause.

The extent to which the Saturn maps agree with the model fitting results may be seen in Figure 14. This figure presents horizontal and vertical cross sections through the data map and model map which are shown in Figures 10A and B. The positions of these cross sections are shown in Figure 13B. The model and data cross sections are of generally the same shape, as indeed they should be. However, there are some aspects of the profiles which do not agree. In particular, the depth of the negative feature and peak deflection due to the rings do not agree. As was noted previously, the ring peaks appear to be shifted horizontally to the east about 2 to 3 arcsec relative to the model. The shapes of the ring induced deflections agree fairly well with those predicted by the models. The large negative feature due to the blockage of the planet by the rings is also shifted a couple of arcsec to the east of the model prediction, but its position agrees fairly well with the models in the north-south direction. The east-west shape of the negative feature does not agree well with the model feature since it is asymmetric in

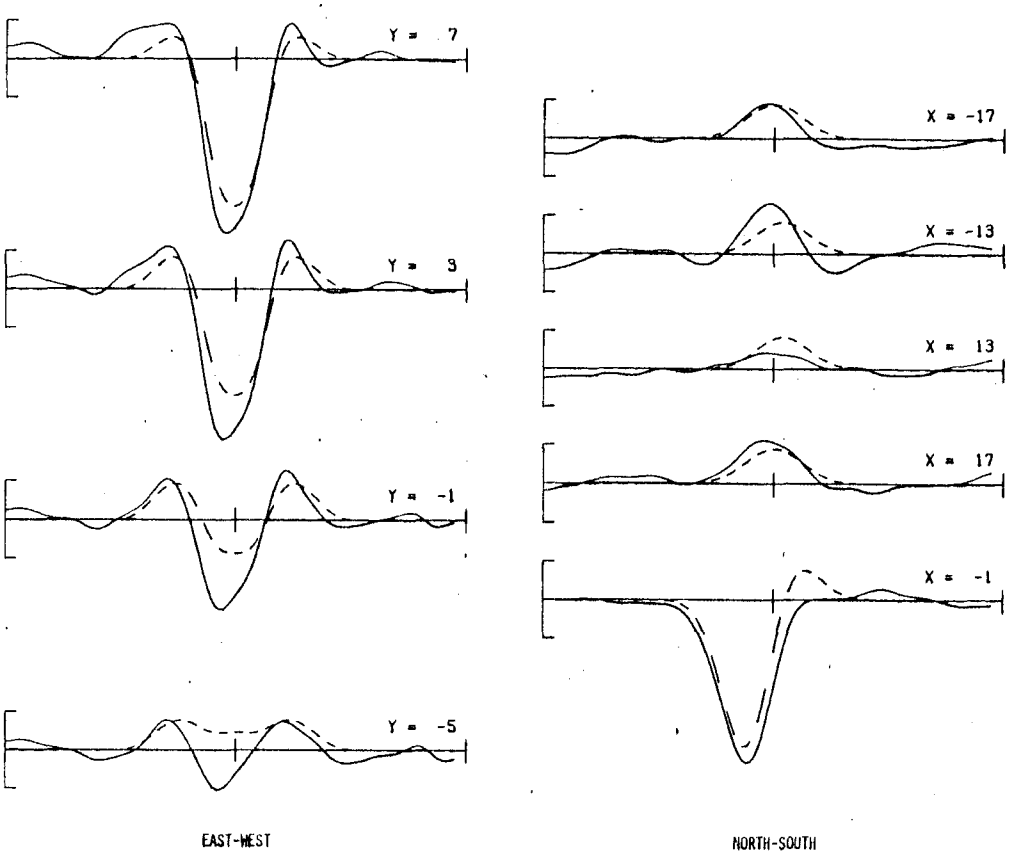

Figure 14 - Horizontal (east-west) and vertical (north-south) cross sections through the 1976 OVRO disk subtraction map shown in Figure 10A compared to cross sections through the model map (dashed profile) shown in Figure 10B. The positions of the cross sections with respect to Saturn are shown in Figure 13B. The horizontal length of the cross sections is 2 arcmin for Saturn at the standard distance of 8 AU. The vertical scale to the left of each cross section represents ±5 K of brightness temperature averaged over the CLEAN beam.

addition to appearing shifted to the east. The north-south shape of the negative feature agrees fairly well with the model feature although the maximum depth is not attained. In the portion of the disk not covered by the rings, the model shows a positive deflection where the data show none. In general, over the whole region of the disk, the data lie below the model.

The lack of total agreement between the data maps and the model maps is somewhat puzzling, since the model is a best fit to the visibility function that was Fourier transformed to make the data maps, but it is not surprising. In some cases, the lack of agreement can be seen to be caused by the fact that the model fitting procedure fits the best model that is symmetric about the y axis in the map. Thus, features that are shifted, such as the peak deflections due to the rings, will be imperfectly fit by the symmetric, best fitting model. In addition, the data on each baseline were weighted differently in the model fitting process. This has the effect of weighting the fit to certain spatial frequencies in the maps more highly than others so that the overall map of the model, which involves all the measured spatial frequencies, might be slightly different from the map of the data. Thus, the best fitting model is chosen on the basis of different, and probably more correct, criteria than would have been employed if the model fit were done in the x-y plane rather than the u-v plane. The fact that the data and model maps do not totally agree, then, does not indicate that the model fitting results are incorrect.

To see whether the model is a fair representation of a Saturn map that is symmetric about the map y axis, the data were Fourier transformed in a way that forced the map to be symmetric about the y axis. Cross sections through this map are compared to the map of Model 3 in Figure 15. The positions of these cross sections are given in Figure 13C. As can be seen from the cross section plots, the noise level in the sky in the symmetric maps is higher than the noise level in the regular version of the maps. This might seem contradictory, since one might expect that when the east and west halves of the maps are averaged the result might have a noise level that was lower by a factor of something like the square root of two. However, this is clearly not the case and the reason seems to be that, unlike a map made with a filled aperture telescope, the deflections due to noise on one side of the map are correlated to some extent with those on the other side of the map, since they are both produced by non-random errors in the measurement of the phase of the visibility function. Thus, when the sides are averaged, positive and negative deflections do not tend to cancel each other out, but rather deflections of the same signs tend to add together to produce a larger deflection. The symmetric maps are not, therefore, more sensitive versions of the Saturn data maps.

Figure 15 shows a much better agreement with the model since the average ring peaks are in the same east-west positions as the model peaks. Similarly, the negative feature is in the same east-west and north-south position as the model. The amplitudes of

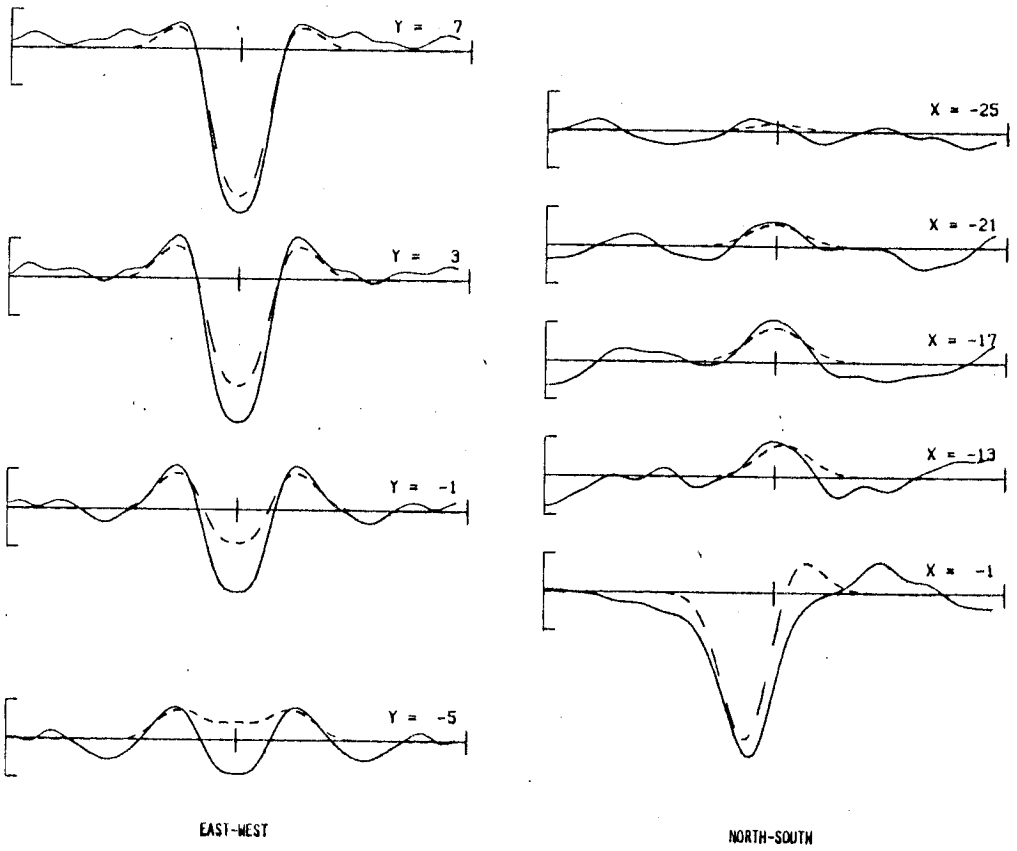

Figure 15 - Horizontal (east-west) and vertical (north-south) cross sections through the 1976 OVRO disk subtraction map which is forced to be symmetric about the y map axis compared to cross sections through the model map (dashed profile) shown in Figure 10B. The position of the cross sections with respect to Saturn are shown in Figure 13C. The horizontal length of the cross sections is 2 arcmin for Saturn at the standard distance of 8 AU. The vertical scale to the left of each cross section represents ±5 K of brightness temperature averaged over the CLEAN beam.

these features are still not in total agreement with the amplitudes of the model, although their shapes agree quite well. Thus, while the main features of the radio emission are adequately modeled, the agreement between the data maps and model maps is imperfect. These discrepancies will now be examined further to determine whether they are due to real and, so far, unmodeled structures in the Saturn system.

(ii) Maps of the Residuals to the Model Fits

Aperture synthesis maps of the residuals to Model 3 have been produced in the same manner as all of the other maps described here. The visibility function of Model 3 was subtracted from the measured visibility function and the result was Fourier transformed and "cleaned" to produce the residuals maps. These maps, which are maps of the difference between the data map and the model map, should show any unmodeled or incorrectly modeled features in the Saturn brightness structure. In this respect, they are quite like the disk subtraction maps which showed the rings and the effect of the blockage of the planetary emission by the rings as residual features that could not be modeled by a uniformly bright disk. The residuals maps are shown in Figures 16A and 16B. Figure 16A is a map of the residuals to Model 3 which has been cleaned with the high resolution 8 x 15 arcsec beam. Cross section plots for the map in Figure 16A are shown in Figure 17. The positions of these cross sections are given in Figure 13A.

The residuals maps in Figures 16A and 16B contain several minor deflections as well as a comparatively large negative deflection

Figure 16A - CLEAN 1976 OVRO aperture synthesis map of the residuals to Model 3, which is described in Part III. An outline of the planet and the combined A and B ring as seen at the time of the observations is shown for comparison. The HPBW of the CLEAN beam is 8 arcsec in the horizontal (x) map direction and 15 arcsec in the vertical (y) direction. The deflections in the map are in units of brightness temperature and represent the brightness temperature of the source averaged over the CLEAN beam. The contour values are: 4K, 2K, -2K, -4K, -6K, -8K. Dashed contours represent negative values. The interval between tick marks at the edge of the map is 10 arcsec for Saturn at the standard distance of 8 AU.

Figure 16B - CLEAN 1976 OVRO aperture synthesis map of the residuals to Model 3. This map is the same as that of Figure 16A except that the CLEAN beam is a circular gaussian with an HPBW of 15 arcsec. The contour values in this map are 2K, 1K, -1K, -2K, -3K, -4K, -5K.

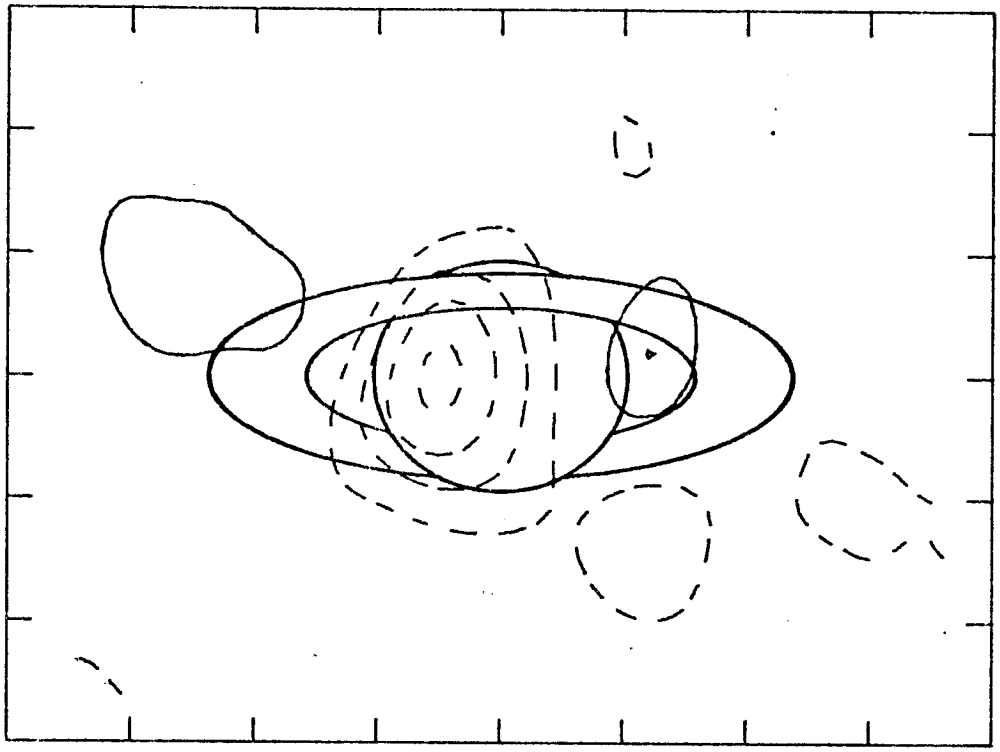

Figure 16A

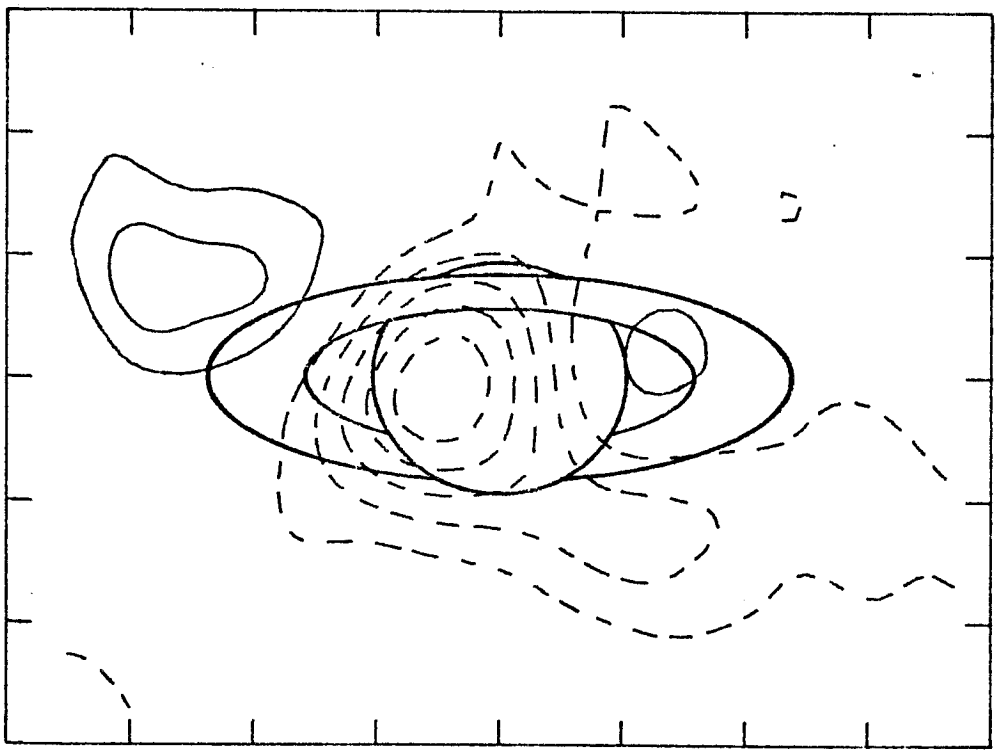

Figure 16B

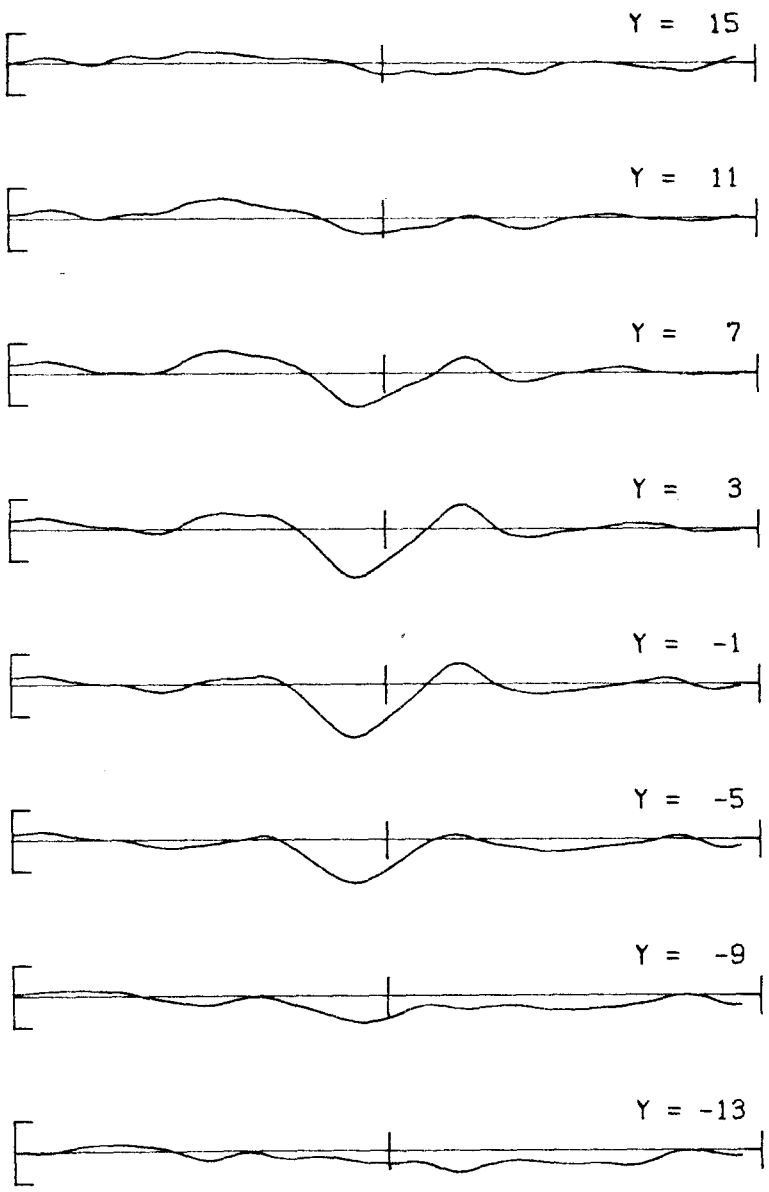

Figure 17 - Horizontal (east-west) cross sections through the 1976 OVRO residuals map shown in Figure 16A. The positions of the cross sections with respect to Saturn are shown in Figure 13A. The horizontal length of the cross sections is 2 arcmin for Saturn at the standard distance of 8 AU. The vertical scale to the left of each cross section represents ±5K of brightness temperature averaged over the CLEAN beam.

located in the eastern half of the planet. Since this is a residuals map, both negative and positive features may be real, and a first look at the cross-sections plotted in Figure 17 indicates that the negative feature, and possibly the positive features to either side of it, may be real ones. However, before claiming to have discovered a real feature in the residuals map, it is necessary to make an estimate of RMS deflection due to noise.

The RMS deflection in the residuals maps has been estimated in two ways. In the first way, the RMS deflection on a rectangular path should be far enough away from any real structures in the map so that it will not be influenced by them. For the 8 x15 arcsec beam map the average deflection was only 0.01 K while the RMS was 1.13 K. The circular 15 arcsec beam map gave an average deflection of 0.01 K and its RMS deflection was 0.60 K. The RMS deflections determined in this manner scale exactly as the beam areas as was expected from equation (5). Further, their absolute values are quite similar to those expected based upon equation (5) and the system parameters of the Owens Valley interferometer. The RMS deflections relative to the peak deflection in the 8 x 15 arcsec beam map without the disk subtraction (Figure 8), are 0.008 for the 8 x 15 arcsec beam map and 0.005 for the 15 x 15 arcsec beam map. Both of these normalized RMS deflections have values quite close to the best dynamic ranges that may be expected in an aperture synthesis map at this time(Brouw, 1975).

A second, more conservative, method of estimating the RMS deflection has also been employed. This method used the peak-to-peak amplitude of the deflections outside the cleaning box to estimate the RMS deflection in the same way that the peak-to-peak scatter of the visibility function measurements was used to estimate errors on the data in Part III. The RMS deflection was taken to be one-third the peak-to-peak deflections away from the source. This method gives an RMS deflection of 1.9 K for the 8 x 15 arcsec map and 1.0 K for the circular 15 arcsec map. These values normalized by the peak deflections in the full data map are 0.014 and 0.009 for the 8 x 15 arcsec and 15 x 15 arcsec maps, respectively.

The estimates of the RMS deflection due to noise made by the second method are larger than those made by the first method. Their size, however, seems to be more in keeping with the noise deflections observed in the map. If the estimate made by the first method is used, there are several 2-sigma deflections far away from the planet and rings in both the maps of Figure 16A and 16B. If the second estimation is used, then the only 2-sigma or greater deflections are in the region of the source. Thus, the second estimate of the RMS deflection seems to be the more consistent one based upon the apparent noise in the sky away from the source. The reason that this larger value is the better one may be because of the non-random types of noise that enter into an aperture synthesis experiment. The deflections that result from this type of noise may be too few in number to affect an RMS determination made by the first method,

but they are important to include in any estimate of the background noise level. Therefore, the values of 1 K and 2 K are adopted as the RMS noise level in the 15 x 15 arcsec and 8 x 15 arcsec maps. These values are obviously not intended to be hard criteria for establishing whether a given feature in the maps is real. For example, a one or two sigma deflection in the region of the rings will be given more careful consideration than a three or four sigma deflection far from the planet. The one sigma values, then, are merely intended to be guidelines for determining which features in the map are real ones.

The feature in the residuals maps of Figures 16A and 16B that is most likely to be real is the negative feature centered in the eastern half of the planet. This feature is four or five times the noise level and in a position that makes it likely to be a real structure. The high resolution 8 x 15 arcsec map shows that the feature is fairly well confined to the Saturn system and this fact adds to its believability. The next most likely feature is the positive deflection which lies between the planet and the western ring ansa. This deflection is twice the noise in the 8 x 15 arcsec map and confined to the Saturn system. It does not rise as far above the noise level in the 15 x 15 arcsec maps although this may be the result of being averaged with the large negative feature to a greater extent than in the 8 x 15 arcsec maps. There are other features in the residuals maps that are the size of the noise or somewhat larger. However, these features are not in the Saturn system and, for this reason, they are not

very likely to be real. Thus, the two features which are the most likely to be real and should be the most carefully considered are the large negative feature in the eastern half of the planet and the smaller positive feature between the western limb of the planet and the western ring ansa.

The large negative feature and the smaller positive feature are not likely to be due to any errors in the model fitting analysis. This is because they are not in the correct position and do not have the correct shape to be caused by a structure in the models such as the disk, rings or blocked regions. Apparently, then, the model has done all it can to fit the brightness structure of the source and the residuals are due to something which is not included in the model.

There are two explanations of the residual features which may each be adjusted to fit the residual brightness structures. First, it is possible that the assumption of uniform brightness across the planet is not correct and that, in fact, the eastern half of the planet has a lower brightness temperature than the western half. This explanation might seem attractive since the colder, eastern half of the planet is the morning side. However, the brightness temperature difference between the morning and afternoon halves of the planet implied by the size of the negative feature seems rather excessive.

A careful modeling of the effect of a brightness temperature variation that is linear in the x coordinate of the maps shows

that a considerable gradient in the brightness temperature across the disk is required to match the size and shape of the negative feature. It is clear, though, that it is possible to match the size and shape of the feature in some detail with this simple model. In Figure 18A a cross section through the center of the map in Figure 16A is shown along with a suite of models which have a linear brightness temperature variation across the disk. The residual linear brightness temperature structure is defined to be

$$T_B(x) = T_o \left[1 + \frac{1+P}{2} \left(\frac{x}{a} - 1 \right) \right]$$

where a is the equatorial radius of Saturn and the profiles shown have chosen T_o so that the depth of the model feature is the same as the depth of the feature in the residual map. Thus, P, the ratio of the positive brightness temperature at the west limb to the negative value of the east limb, is the parameter varied in the figure. It is seen that the profiles do a rather good job of mimicking the observations and, with a clever choice of the parameter P, they can be made to fit the negative feature and, to a lesser extent, the smaller positive feature. However, in order to achieve a good match between this model and the data map, the eastern half of the planet must have a brightness temperature that is about 10 K less than the western half.

The large variations in the planet brightness temperature across the disk make this model for the negative residual feature seem rather implausible, although because it can be made to fit the data, it

Figure 18A - Horizontal (east-west) cross section through the 1976 OVRO residuals map (dotted) shown in Figure 16A compared to model with brightness temperature variation described in the text. The cross section shown is the one at y = -1 arcsec in Figure 17. The parameter on the curves is the absolute value of the ratio of the brightness temperature at the (positive) west limb of the planet to that of the (negative) east limb. The horizontal length of the cross sections is 2 arcmin for Saturn at the standard distance of 8 AU. The vertical scale to the left of each cross section represents ±5K of brightness temperature averaged over the CLEAN beam.

Figure 18B - Horizontal (east-west) cross section through the 1976 OVRO residuals map (dotted) shown in Figure 16A compared to the position offset models described in the text. The cross section shown is the one at y = -1 arcsec in Figure 17. Models with position offsets of 0.50 and 0.25 arcsec for Saturn at the standard distance of 8 AU are shown. The offset is in the sense that would have to be added to the true position in order to bring it to the center of the map. The parameters on the curve are the ratio of the brightness temperature of the subtracted disk, which is taken to be 186K, to the true value. The horizontal length of the cross sections is 2 arcmin for Saturn at the standard distance of 8 AU. The vertical scale to the left of each cross section represents ±5 K of brightness temperature averaged over the CLEAN beam.

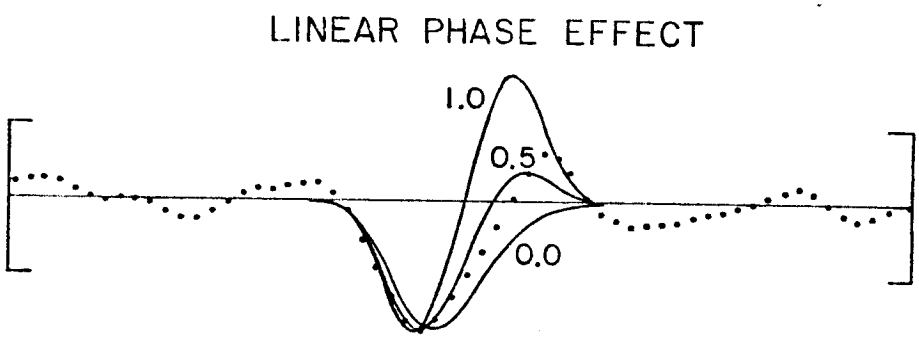

Figure 18A

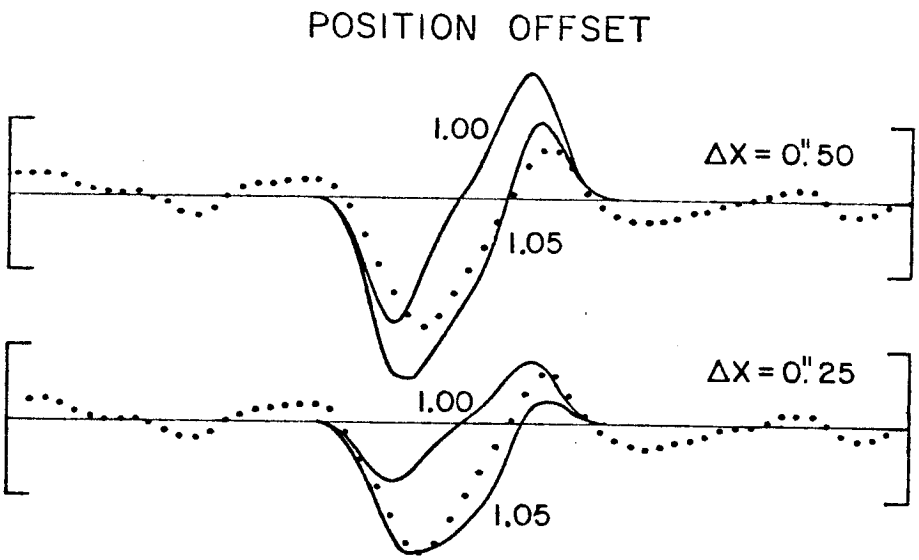

Figure 18B

cannot be ruled out. If a variation in the planet brightness temperature were the correct explanation of the negative residual feature, then it is likely that the variation is not produced by a variation of the physical temperature of the atmosphere in the region where the 3.71 cm emission originates. This is because the radio radiation comes from a pressure level of about 1 bar or greater (Gulkis and Poynter, 1972), and at these deep levels in the atmosphere the radiative time constant is much longer than the rotation period. Thus, it is more likely that the variation would be due to some change in the atmospheric opacity structure rather than a change in the temperature structure. Further, since no such large variation is observed in thermal infrared maps of the planet (Rieke, 1975), this change must take place in the deep atmosphere in the region where the 3.71 cm radiation originates. All of these constraints combine to make the explanation of the negative feature in terms of a brightness temperature variation seem rather unlikely. As well, the models which seem to fit the negative feature the best do not provide a very good explanation of the positive one. Thus, this model seems only capable of explaining the negative feature, and although it cannot be ruled out as an explanation, its consequences make it seem unlikely.

A second, and more believable, effect that can produce both the negative and the positive feature in the residuals maps is an offset of the true geometric center of Saturn from the map center. This effect was discussed briefly in a previous section where it was

pointed out that errors in the position of Saturn of half an arcsec or less were not unlikely. The appearance of a map with such an offset included will now be considered more carefully.

Figure 18B shows the effects of offsetting the planet to the west of the map center and then subtracting a disk at the map center. The profiles are horizontal cross sections through the center of the residuals map and they are compared to the predictions for a ½ arcsec offset in the top curve and a ¼ arcsec offset in the bottom curve. The parameters on the offset curves are the ratio of the brightness temperature of the disk subtracted from the map to the assumed true disk brightness temperature. In all cases, the brightness temperature of the subtracted disk was taken to be the Model 3 value of 186K and the disk dimensions were taken to be those used in the model fitting analysis.

The cross section profiles in Figure 18B show much the same structure as the data and seem to be more capable of explaining the small positive feature in the residuals map. It appears that the best fitting profile would be obtained with an offset of between ¼ and ½ arcsec and a subtracted disk whose brightness temperature was a few percent larger than the true disk brightness temperature. These values agree with both the likely position errors for the center of mass of Saturn and with the apparently high value of the planet brightness temperature obtained in the model fitting analysis. Further, the offset models show that both the negative and positive features in the residual map are likely to be explained with some adjustment of

the offset and relative brightness temperature values. Thus, the offset explanation appears to be the most likely one since it is consistent with the expected position errors and is capable of explaining the two largest features in the residuals map.

(iii) Maps and Models Including a Position Offset

The results of the previous section suggested that the true geocentric ephemeris of Saturn may be systematically offset from the nominal positions given in the American Ephemeris and Nautical Almanac (AENA). In this section, model fitting and aperture synthesis techniques are used to determine whether such a position offset exists and can be used to explain the features in the residuals maps. Model fitting for an average position offset is somewhat difficult since the offset parameters are non-linear. Therefore, a brute force least squares procedure, like the one used to solve for the effective disk radius, has been used to fit the position offset parameters to the data.

The results of the model fitting to the brightness temperature parameters of Model 3 and including a possible offset in the position of Saturn are given in Table 9 along with the parameters that were fit to Model 3 without an offset. The position offset is given in units of Saturn equatorial radii in the x (along the major ring axis) and y (along the minor ring axis) directions in the map. The offset is expressed as the correction to the AENA geocentric ephemeris that is required to give the best fit to

TABLE 9

MODEL INCLUDING POSITION OFFSET

COMPARED TO MODEL WITH NO OFFSET (3.71 cm)

	Model 3 XY (Includes Position Offset)	Model 3
T_B Planet	188.0 ± 1.6	186.0 ± 1.7
T_B Planet Blocked by C Ring	73.4 ± 20.7	106.9 ± 21.2
T_B Planet Blocked by A & B Ring	71.0 ± 9.6	65.2 ± 9.8
T_B C Ring	9.1 ± 2.9	8.9 ± 3.0
T_B B Ring and A Ring	7.6 ± 1.3	7.6 ± 1.3
T_{DISK}†	171 K	171 K
X Offset (equatorial radii)*	0.026 ± 0.007	---
Y Offset (equatorial radii)*	- 0.022 ± 0.012	---
Percent Improvement in Residuals from Model 3	3.2	---

† $T_{DISK} = \frac{\lambda^2}{2k} \times \frac{\text{Model Flux Density}}{\text{Solid Angle of Elliptical Disk with AENA Radii}}$

* Equatorial Radius of Saturn is 10.31 arcsec at 8 AU.

the data. As can be seen from Table 9 , the corrections that are determined are at least twice their standard errors and the sum of the squares of the residuals is significantly improved by the addition of the offset parameters. Thus, when these factors and the appearance of the residuals maps in Figure 16 are considered, the position offsets determined by the model fitting procedure are quite likely to be real.

Unfortunately, these results must remain somewhat uncertain since there is probably no way to distinguish between a position offset and a variation in the brightness temperature of the planet across the disk, which was another possible explanation of the features in the residuals maps. However, the variation that is required is probably much too large, and therefore, the position offset explanation is the more likely one.

Since the amount of variation of the planet's brightness temperature that was required to match the features in the residuals maps was deemed excessive, it is worth considering whether the position offset determined by the model fitting analysis is within reason. To do this, the position offsets given in Table 9 have been converted to the average offsets in the right ascension and declination of Saturn from the nominal AENA position. If the average distance to Saturn at the time of the observations is taken to be 9.9 AU and the position angle of its central meridian is -7°, then the position offsets determined by the model fitting are:

$$\Delta\alpha = 0.26 \pm 0.06 \text{ arcsec}$$

$$\Delta\delta = -0.16 \pm 0.09 \text{ arcsec}$$

These values are only approximate since the distance to Saturn varied between 9.6 and 10.0 AU during the observing run. This variation means that the position offsets relative to the equatorial radius varied from day to day as the distance to Saturn changed. For the purposes of this work, these approximate values are sufficient. However, they should not be taken to be the best estimates of the position offsets since a proper estimation would take the changing distance into account.

The offsets determined by the model fitting seem to be large, but they are within the probable errors in the AENA geocentric ephemeris. In addition, they are in the range of uncertainty of the position of OJ287, which was used to determine the position of the center of the map. Thus, a position offset remains a likely explanation. As a further test of the model fitting, however, the results have been compared to the position offset predicted by the Jet Propulsion Laboratory's Developmental Ephemeris 96, which is supposed to be an improvement over the AENA ephemeris. The geocentric position of Saturn predicted by JPL DE-96 for June 1, 1976 was computed by X.X. Newhall (private communication) and is:

$$\alpha_{\text{JPL DE-96}} = 8^{h}07^{m}20^{s}.31$$

$$\delta_{\text{JPL DE-96}} = 20^{\circ}40' 20''.01 \ .$$

The geocentric position predicted by the AENA for the same date is

$$\alpha_{AENA} = 8^h07^m20^s.277$$
$$\delta_{AENA} = 20^\circ40'\ 20''.36 \quad ,$$

and the difference between these two positions is

$$\Delta\alpha = \alpha_{JPL} - \alpha_{AENA} = 0.50 \text{ arcsec}$$
$$\Delta\delta = \delta_{JPL} - \delta_{AENA} = -0.35 \text{ arcsec}$$

which is in the same direction and slightly larger than the offset determined by the model fitting analysis. This further supports the claim that a position offset is the correct explanation of the features in the residuals maps of Figure 16.

The addition of the position offset parameters to the model does not affect the brightness temperature results for most of the regions in the model. Only the brightness temperature of the planet and that of the region of the planet blocked by the C ring change by more than one standard deviation. The planet brightness temperature increases by only slightly more than one standard deviation, and its increase is probably not significant. The brightness temperature of the region of the planet that is blocked by the C ring decreased by about 1.6 standard deviations, and therefore, it is not formally different from the value determined by the model without the offset either. The difference that is observed probably indicates a high degree of correlation between the brightness temperature of the region of the planet blocked by the C ring and the position of the planet in the model

fit. Such a correlation is not unreasonable since the region is on the planet and its size and shape are barely resolvable by the data. Thus, the region of the planet that is blocked by the C ring has the least well determined brightness temperature in the model fit and should, therefore, be viewed with the greatest caution.

In order to see whether the new model fit would explain all of the features in the residuals maps of Figure 16, a map of the residuals to the new model, Model 3XY, was made in exactly the same manner as the residuals map of Figure 16A. This new residuals map is shown in Figure 19A. The new map contains a broad negative feature that covers the entire planet. The feature's greatest negative value is located in the north-east quadrant of the planet and is less than the peak value in the old residuals map. The small positive feature, which was near the western limb of the planet in the old residuals map, is now nearly completely gone and no longer at a significant level. There are no other features at a significant level in the new residuals map.

The map of the residuals to Model 3XY has shown that much of the structure in the map of the residuals to Model 3 is the result of an offset in the position of Saturn from the center of the map. The negative feature is still present in the new residuals map; however it is broader and shallower than it was in the old maps. The negative feature in the new map resembles the shape of a feature that is due to emission from the

Figure 19A - CLEAN 1976 OVRO aperture synthesis map of the residuals to Model 3XY, which is the model fit that includes the apparent offset in the position of Saturn from the nominal AENA values. An outline of the planet and the combined A and B ring as seen at the time of the observations is shown for comparison. The HPBW of the CLEAN beam is 8 arcsec in the horizontal (x) map direction and 15 arcsec in the vertical (y) direction. The deflections in the map are in units of brightness temperature and represent the brightness temperature of the source averaged over the CLEAN beam. The contour values are: 2K, -2K, -4K, -6K. Dashed contours represent negative values. The interval between tick marks at the edge of the map is 10 arcsec for Saturn at the standard distance of 8 AU.

Figure 19B - The same map as Figure 19A except that the brightness temperature of the unobscured portion of the planet has been taken to have a value of 180K, which is 8K less than the best fitting value of Model 3XY.

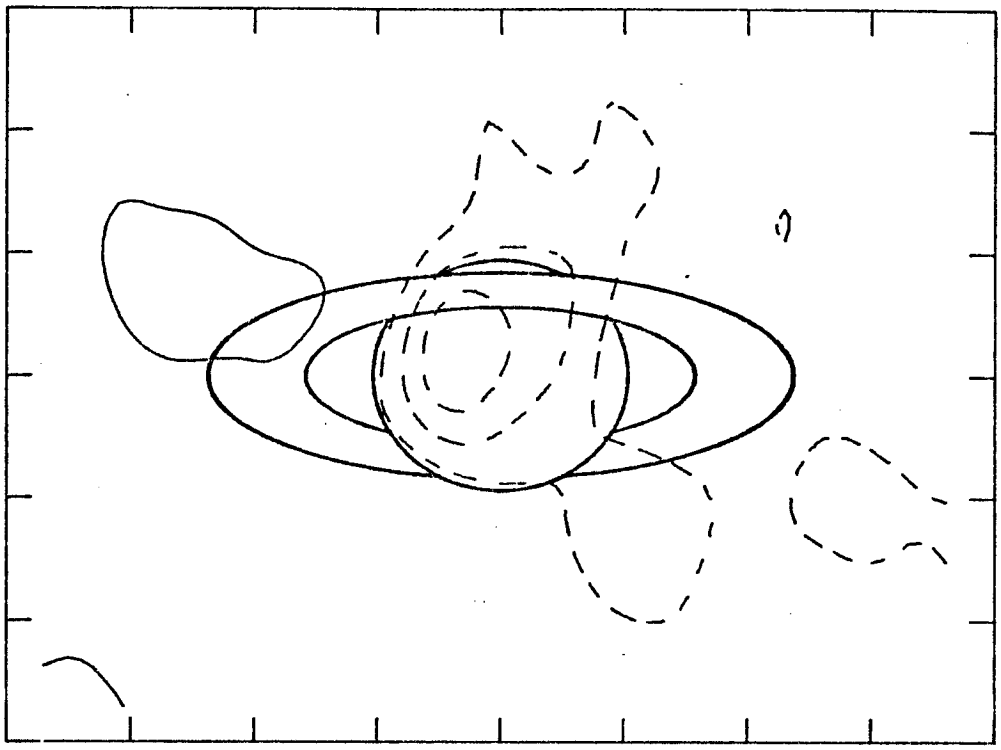

Figure 19A

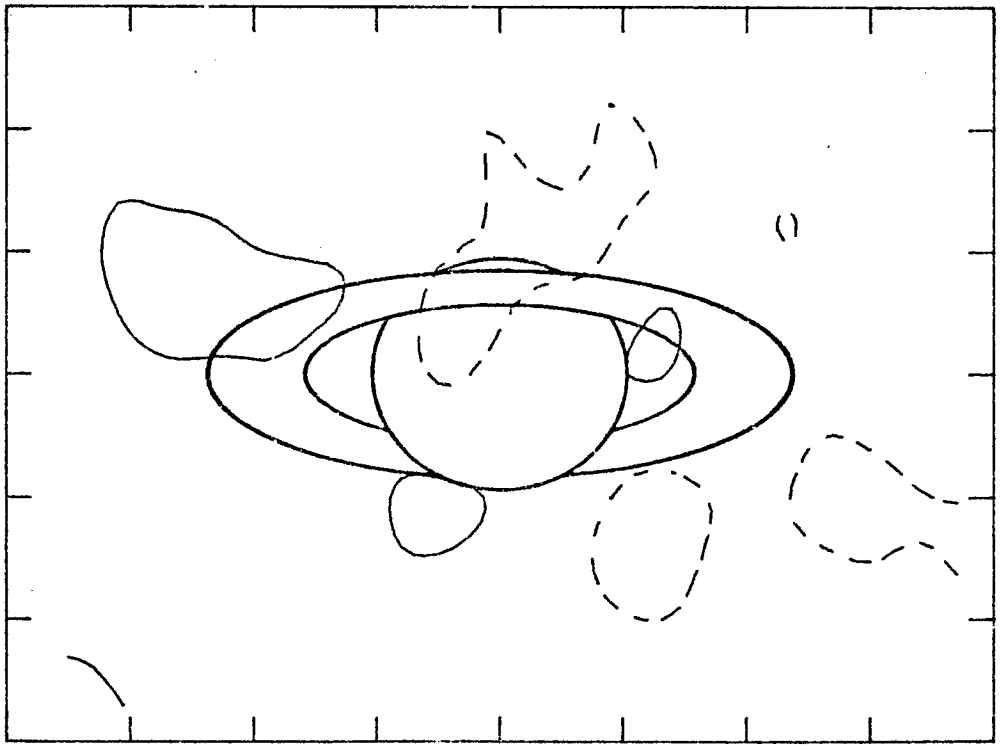

Figure 19B

uniformly bright planet. Since the feature is a negative one, it indicates that the brightness temperature of the planet that was determined by the model fitting was slightly higher than it needed to be in order to match the contours in the Saturn maps. To demonstrate this fact, the residuals map in Figure 19B has been produced. This map is the same as that of Figure 19A except that the unobscured portion of the planet has been taken to have a brightness temperature that is 8 K less than the value determined by the model fit. The map contains no features which are at a significant level. Thus, it appears that no new features which have not been included in the model fitting analysis are required to match the present data to its accuracy.

(iv) Summary of the Aperture Synthesis Results

In this section, aperture synthesis maps of Saturn and the ring system have been shown. The maps are free from many assumptions about the brightness structure of Saturn that are employed in a model fitting analysis, and therefore, they may be used to confirm the model fitting results and search for features which have not been included in the models. Generally, the maps confirm the model fitting results, although an exception to this is that the brightness temperature of the planet that is determined by the models is greater than it needs to be in order to match the contours in the map. The reason for this discrepancy is unknown, but random errors in the phase of the visibility function, which are more important to the maps than to the model fitting, may cause the

map brightness temperatures to be slightly underestimated. The residuals maps which correct for an offset in the position of Saturn from the nomial AENA values show that no new brightness features are required by the present data. In particular, no azimuthal variations in the brightness temperature of the rings are required, although they may be present and simply undetected. It is difficult to assess an upper limit on these hypothetical variations since the upper limit that is estimated depends upon the model of the variations that is assumed. It is suggested, therefore, that those who wish to pursue this question further compute maps of their proposed variations and compare them directly with the maps given here.

V. INTERFEROMETRIC OBSERVATIONS OF SATURN AT A WAVELENGTH OF 1.30 cm

a) Introduction

Interferometric observations of Saturn were made at the University of California's Hat Creek Radio Astronomy Observatory at a frequency of 23 GHz (1.30 cm wavelength). The observations were made during 2-22 November 1976, and they were designed to produce an aperture synthesis map of the Saturn system. Nine different interferometer baselines were used to obtain the u-v coverage shown in Figure 20.

The Hat Creek observations are similar to the Owens Valley observations, which were described in Part II, in many of their important features, but there are also important differences. The sensitivity of the Hat Creek interferometer is worse than that of the Owens Valley interferometer in an absolute sense, but the fact that Saturn has about nine times more flux at 1.30 cm than at 3.71 cm, because of its thermal spectrum, means that the relative errors on the visibility function are quite similar. The spatial resolution of the Hat Creek instrument is also quite similar to that of the Owens Valley instrument, although more resolution was achieved at the Owens Valley in both the east-west and north-south directions. The extra resolution is not very important to the aperture synthesis maps of the Saturn system, but it has been found to be important in the model fitting analysis of the data. The principal difference between the two experiments, in addition to the observing wavelength, is that the Hat Creek observations were made at a lower ring tilt angle.

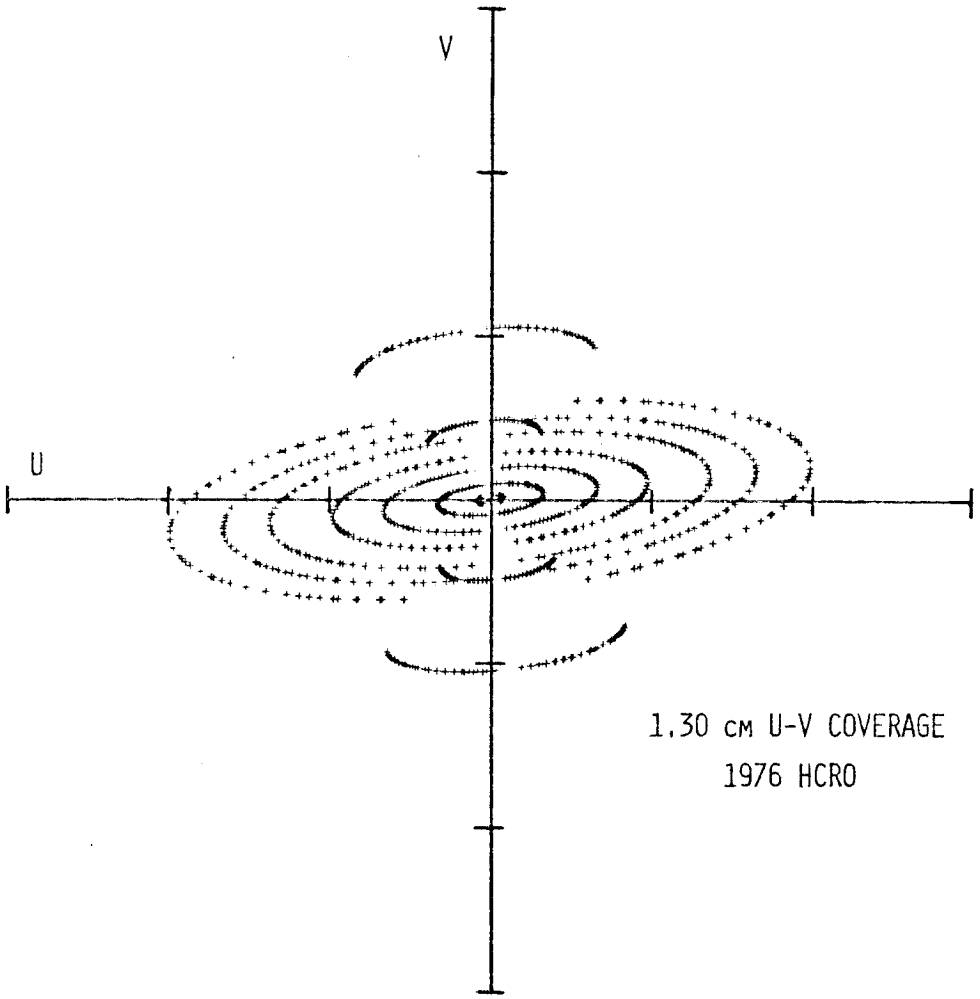

Figure 20 - u-v coverage of 1976 HCRO observations. u and v are the interferometer spacings, expressed in wavelengths, projected onto the planet Saturn. The v axis is at a position angle of -6.7° so that it coincides with the central meridian of Saturn. The intersection of the axes is the point u = 0, v = 0. The u axis increases to the left in increments of 10,000 wavelengths for Saturn as seen at the standard distance of 8 AU. The v axis increases to the top of the figure and is at the same scale. The visibility function at a point u,v is equal to its complex conjugate at -u,-v. Therefore, both values are plotted in the figure since there is information about the source at both locations.

The saturnocentric declination of the Earth was -15.3 degrees during the Hat Creek observations and -20.8 and -26.5 degrees for the Owens Valley observations. The lower ring tilt angle complicates the comparison of the Hat Creek and Owens Valley results since differences that are due to the change in wavelength might also be attributed to the change in the ring tilt angle. In addition, the lower ring tilt angle means that the rings present a small solid angle to the observer and are, therefore, more difficult to detect. Thus, although there are some important similarities between the two sets of observations, there are also important differences which may complicate comparisons of their results.

b) Observing Procedures

The Hat Creek interferometer system has been described fully by Welch et al. (1977), and several of the parameters of the system are given in Table 10. In this section, many aspects of the interferometer will be discussed, but the emphasis will be on those features of the observations that were important to the Saturn program.

The Hat Creek interferometer was used in the wide band continuum mode. In this mode, the incoming signal is split into two orthogonal, linear polarizations at each antenna and all four possible polarization pairs are independently correlated. The four possible configurations permit two parallel-feed and two crossed-feed observations to be made simultaneously. For the Saturn observations, the parallel feeds were arranged to be parallel and perpendicular to the central

TABLE 10

PARAMETERS OF THE HAT CREEK INTERFEROMETER

Observing Frequency	23 GHz
Single Antenna Beamwidth (1.2 x λ/D)	9 arcmin
Bandwidth	220 MHz
System Temperature	600 K

meridian of Saturn (PA = -7°) and parallel and perpendicular to a position angle located 45° away from the central meridian (PA = 38°). The parallel-feed and crossed-feed observations made with this set of position angles permit all four Stokes parameters of Saturn to be mapped with the maximum sensitivity.

After each 200 seconds of integration on a source, the observing computer reduces the observations in each of the four possible feed configurations to an amplitude and phase. The results of these 200-second integrations are then written on magnetic tape for further reduction. Typically, five 200-second Saturn integrations were vector averaged into a single 1000-second integration to improve the signal-to-noise ratio of a single observation. Observations of calibrators were typically vector averaged into half-hour integrations. It was found that a half-hour integration on a fairly strong source was required to adequately determine its amplitude and phase for use in calibrating the Saturn data or determining the interferometer baseline. The choice of calibrating sources, then, was rather limited and could not include the principle calibrator of the 1976 Owens Valley observations, OJ287, since it was too weak.

Unfortunately, after all the data reduction and analysis were completed, it was found that the values of u and v used in the analysis were not those of the centers of the integrations, but were the values appropriate for a time that was 100 seconds later than the center time. The effect of this small error has been carefully investigated by making a first order correction to the u-v values

and refitting the models to the data. No difference that was greater than 0.1 standard deviations occurred, and therefore the results of the model fitting and aperture synthesis analysis are unaffected by the small u-v error.

Interferometric observations at wavelengths as short as 1.30 cm require several corrections to be applied to the data that are not necessary at longer wavelengths due to the transmission of the incoming signal through the Earth's atmosphere. First, at 1.30 cm the Earth's atmosphere attenuates the incoming radiation significantly. The 1.30 cm optical thickness of the atmosphere at the Hat Creek observing site was typically 0.07 and this is enough to systematically affect the observations. The optical thickness is estimated by making observations of the brightness temperature of the sky. This method leads to errors on the amplitude of about 2% under the best conditions (Welch et al., 1977). In the presence of many scattered clouds or a thick cloud deck, however, consistent results were difficult to obtain and the errors due to atmospheric attenuation are probably larger. The second effect of the Earth's atmosphere is that it refracts the incoming rays. This refraction causes the differential path length between the two elements of the interferometer to be different from the geometric value and this difference could cause serious drifts in the phase measurements if it were not corrected. Thus, a correction for this effect is applied to the phase at the time of the observations by the observatory's computer.

The limb of the Sun was used to determine the antenna pointing corrections each time an antenna was moved. Subsequent checks on the pointing, using the Sun, showed that it was consistently good to within 0.5 arcmin. In addition to the solar observations, a television camera that was aligned with the electrical axis of one of the antennas was used to monitor the position of Saturn during the time it was observed at night. This continuous observation of Saturn in the beam confirmed that the average pointing errors were probably less than 0.5 arcmin.

The short observing wavelength required that the interferometer baselines be determined to approximately one millimeter or better in order to avoid serious systematic drifts in the phase. Two methods were used to determine the baselines at Hat Creek. The first method, which is commonly used at Hat Creek, consists of a long observation of a single source over all of its possible hour angles in the sky followed by a series of shorter observations of several sources at different declinations. The phase drifts observed on the long observation of a single source are used to determine the equatorial components of the interferometer baseline and the shorter observations following this are used to determine the polar component of the baseline. The second method, which is used extensively at the Owens Valley observatory, consists of making several observations of different sources at different positions about the sky. The phase differences between pairs of observations are then used to determine the best fitting baseline. It is felt that the second method is superior

since drifts in the instrumental phase, which occur in all interferometers, do not affect the baseline determination as seriously as they do the first. Such phase drifts affect the determination of the baseline by the first method since they cause the equatorial components of the baseline, which are based upon the long observation of a single source, to be estimated incorrectly. Fortunately, although drifts in the phase are observed to occur, the baselines determined by the first method appear to be adequate for the purpose of these observations, and there are no serious systematic differences found between the baselines determined by the two methods.

Although there is no question that the baseline can be determined, there is some question that the baseline determined will remain constant during all of the observations. A relative movement of the antennas by only a few millimeters can seriously affect the observations since it changes the baseline by a significant fraction of a wavelength. Such a movement has apparently taken place on at least two of the baselines and, to some extent, has probably occurred on more of them. The movement of the antennas has been detected by using phase calibrators on each of the days of observation to determine a baseline. In most cases, the baseline determined on one day is identical, within the errors, to that determined on other days. On two occasions, though, the baseline changed enough to affect the observations. On the 260-foot north-south baseline, the baseline changed by a couple of millimeters in its east-west component at some time between the two days of Saturn observations. The change

appears to have taken place all at once since each day's observations are well fit by a single baseline. Since this is the case, the baseline determined on each day is used for the final reduction of the observations on the 260-foot north-south baseline. The other baseline which apparently changed was the 320-foot east-west baseline. Here the change amounted to about 2 mm in the polar component of the baseline and occurred between the time that most of the baseline observations were made and the time that Saturn was observed. In this case, the Saturn calibrators were used to correct the baseline determined by the baseline calibrators, and this corrected baseline was used for the final data reduction. Although the effects of the apparent baseline changes are, to some extent, removed from the data, some residual effects are sure to remain and affect both the model fitting analysis and the aperture synthesis maps.

Approximately once every 2.5 hours during the Saturn observations, a point source of known flux density and position was observed in order to calibrate the gain and phase of the interferometer. The calibrators used are listed in Table 11 along with their assumed flux densities. The flux density and phase of CAS A were not used to calibrate the interferometric observations directly, but the flux density was used in the absolute calibration of the flux calibrators. Each of the other calibrators in Table 11 is known to be a variable radio source, and therefore, their relative flux densities were checked many times during the observing run. Since no variation was detected, their flux densities were assumed to be constant during the observations.

TABLE 11

CALIBRATORS FOR SATURN OBSERVATIONS AT 23 GHz

Source	Flux Density (Jansky)
CAS A*	256.5
3C84	46.2
3C120	7.7
3C273B	36.5

* Flux density from spectrum of Janssen, Golden and Welch (1974). CAS A not used as an interferometer calibrator.

The absolute calibration of the flux calibrators was determined by using one of the 20-foot antennas to measure the relative flux densities of 3C84 and CAS A. The ratio of the flux density of 3C84 to that of CAS A was determined by comparing several adjacent 20-minute integrations on the sources. The result, corrected for the resolution of CAS A by the antenna beam by a factor of 1.08 ± 0.01 (Janssen et al., 1974), is 0.18 ± 0.01. The uncertainty on this result is based upon the scatter of the individual measurements of the flux density ratio and the uncertainty quoted on the correction for resolution. It does not reflect possible systematic errors such as those due to antenna pointing or atmospheric attenuation. Thus, the error on the ratio may be greater than the value quoted.

The flux density of CAS A at 23 GHz has been taken from a fit to its spectrum by Janssen et al. (1974) which includes their absolute measurements at 22.285 GHz. The value for the flux density in epoch 1965.0 is 276.4 Jansky and must be corrected for the decrease in the flux density of 0.6% per year (Dent, Aller and Olsen, 1974). Thus, the final adopted value of the flux density of CAS A at 23 GHz at the time of the Saturn observations is 256.6 Jansky. The flux density of 3C84, then, is 46.2 ± 2.5 Jansky and the flux densities of the other sources in Table 11 were determined by comparison to this value using the interferomenter.

As can be seen from the discussion in the preceeding paragraphs, the absolute flux density calibration of the Hat Creek observations is accurate to about 6%. This estimate of the error does not include the

uncertainties in the measurement that are due to systematic errors, such as pointing errors, and therefore, it is probably an underestimate. As a check on the calibration, a 50-minute observation of Jupiter was made with the interferometer at its shortest baseline on the night of 10 November 1976 and compared to an adjacent 30-minute observation of the primary interferometer calibrator 3C84. This observation gave a result of 92 ± 5 Jansky for the flux density of Jupiter at the standard distance of 4.04 AU. Since Jupiter is quite large, even the shortest baseline used at Hat Creek resolved the planet to some extent, and therefore, a correction for this resolution is required. Jupiter was assumed to be a uniformly bright disk with the dimensions given in the American Ephemeris and Nautical Almanac, and a correction factor of about 1.06 was applied to the observation. The final, unresolved flux density of Jupiter, then, is 97 ± 5 Jansky at the standard distance of 4.04 AU, and when the dimensions given in the AENA for the night of the observation are used, the disk temperature is found to be 146 ± 7 K. It shall be seen in subsequent sections that the flux density of Saturn normalized to 8 AU is 16.2 ± 0.2 Jansky which corresponds to a disk temperature (assuming the AENA disk dimensions) of 139 ± 2 K. The ratio of the Saturn disk temperature to that of Jupiter is 0.95 ± 0.06 and is in good agreement with the results of other observers, which tend to fall between 0.90 and 0.95 (Janssen, 1974). The absolute disk temperatures of both planets are about 8% higher than those of other observers, but this difference is within the experimental errors. The review of Berge and Gulkis (1976) lists many observations of the disk

temperature of Jupiter in this wavelength region, and these seem to be more consistent with a value of about 135 K. Similarly, the review of Newburn and Gulkis (1973) lists observations of the disk temperature of Saturn which are more consistent with a value of about 130 K. Thus, the disk temperatures of Jupiter and Saturn that were measured against the flux scale of Table 11 are somewhat higher than the typical values of other observers. This difference is at about the level of uncertainty in the absolute calibration and is, therefore, consistent with the experimental errors.

The instrumental phase of the interferometer was found to vary slowly during the course of the observations. This variation is often correlated with the rising and setting of the Sun, which rose at about the time that Saturn crossed the meridian. The diurnal variation is typically on the order of 40 millilobes (0.3 radians) of phase and has been observed before in the Hat Creek system (Welch et al., 1977). To remove the effect, a smooth curve was fit to the measurements of the instrumental phase. The instrumental phase at a point in time was taken to be the average phase of the calibrators weighted by a gaussian centered on that time. The scale time of the gaussian weighting function was taken to be three hours, which is approximately the time interval between calibrations. Thus, the instrumental phase is determined primarily by the phases of the closest calibrators. The phase calibration removes most of the diurnal variation, but residual errors at about the 20 millilobe level probably remain and increase the noise level in the aperture synthesis maps.

VI. ANALYSIS OF THE HAT CREEK 1.30 cm OBSERVATIONS BY MODEL FITTING TECHNIQUES

a) Introduction

The model fitting analysis performed on the 3.71 cm Owens Valley data sets confirmed the results of previous workers by showing that the A and B rings have a very low brightness temperature and attenuate the emission from the planet significantly where they cross in front of it. The model fitting extended the previous work by showing that the A ring is less optically thick than the B ring at microwave wavelengths and that the C ring has a brightness temperature that is comparable to the A and B rings and a significant optical depth. Limb-darkening of the planetary emission was also searched for, but it was not detected.

In this part, model fitting techniques are applied to the 1.30 cm Hat Creek data in an attempt to extend the 3.71 cm results to shorter wavelengths. Since the radiation from the rings is primarily scattered planetary emission, any wavelength dependence of the ring brightness temperature will have important implications for the ring particles as will any wavelength dependence of the ring opacity inferred from the blockage of the planetary emission by the rings. In addition, a wavelength variation in the planetary limb-darkening will carry much information about the temperature and opacity structure of Saturn's atmosphere. Thus, since a primary goal of the Hat Creek observing program is to extend the Owens Valley results to the shorter wavelength, it is important to treat the Hat Creek data in the same manner as the Owens Valley data.

b) Model Fitting Procedures

The model fitting analysis performed on the Hat Creek data set is identical to that performed on the Owens Valley data sets in all of its essential characteristics. The same suite of models has been fit to the data and the planetary and ring dimensions of Cook et al. (1973), which are shown in Table 2 along with the apparent polar radius appropriate to the ring tilt value of 15.3 degrees, were used to define the sizes of the model components. The distance to the planet and its geocentric position were taken to be those given by the American Ephemeris and Nautical Almanac.

The data errors, which are used to weight the data in the model fit, were again determined from the scatter of the data points so that the various possible systematic errors that could affect the data are included in the estimation to some extent. The errors on the amplitudes and phases of the visibility function were estimated separately, since they are thought to be mostly independent of each other. The scheme that was used with the Owens Valley data for taking into account the correlations between the errors on the real and imaginary parts of the visibility function, which result from the independence of the amplitude and phase errors, was also used to fit the Hat Creek observations.

The system of weights used to fit the models to the Hat Creek data was designed to take into account both the relative data errors and the amount of new information about the Saturn system provided

by each additional data point. The amplitude and phase errors on a given baseline were taken to be the same for all points on that baseline as was the case with the Owens Valley data. The inverse square of these errors provides the basic weight applied to a given data point. As was the case with the 1973-1974 Owens Valley data set, however, a further consideration of the weighting system is required since certain regions of the u-v plane were sampled more densely than others. If the data were weighted only on the basis of data errors, these highly sampled regions would dominate the model fitting even though they may not be very sensitive to certain model parameters. In order to correct this effect, the baselines were grouped together according to their resolution and the observations on a given baseline were downweighted by the total number of observations in that baseline's resolution group. This downweighting makes each group about equally important in determining the best fitting model. The baseline groups were chosen to be: the shortest baseline, the longest north-south baseline, the intermediate north-south baseline, the east-west baselines whose resolution was equivalent to or greater than the longest north-south baseline, and the east-west baselines whose resolution was equivalent to the intermediate north-south baseline. The final data errors used in the model fitting are shown in Table 12.

c) Results of Model Fitting

The results of the model fitting will be presented in two parts. In the first part, the four models that were fit to the Owens Valley

TABLE 12

ERRORS USED IN MODEL FITTING TO HAT CREEK DATA

Resolution Group	Baseline	Amplitude Error (Jy)	Phase Error (lobes)	Average Amplitude† (Jy)	Number of Points in Resolution Group
1	40'EW	1.00	0.02	16.59	44
2	560'NS	0.50	0.04	3.01	89
3	260'NS	0.75	0.02	12.55	112
4	155'EW	1.00	0.02	15.67	218
4	320'EW	0.75	0.02	12.00	218
5	475'EW	0.50	0.03	8.60	444
5	655'EW	0.50	0.06	4.95	444
5	795'EW	0.50	0.06	3.78	444
5	950'EW	0.50	0.08	2.37	444

† Flux density at standard distance of 8 AU.

data will be fit to the Hat Creek data and discussed. The models that do not include the C ring seemed to give the best results and will, therefore, be given the most consideration. Models including the C ring will be discussed briefly. However, since they are not sensitive to the parameters of the C ring, they will not be emphasized. Finally, in the second part, limb-darkening of the planetary emission was searched for and apparently detected.

(i) Models Consisting of the Planet, the Blocked Region, and the Rings

In this section, the same four models that were fit to the Owens Valley data were fit to the Hat Creek data. The results of the model fitting are given in Table 13. Model 1, which appears to give the most consistent results, consists of the brightness temperature of the A and B rings combined into a single, uniformly bright ring, the brightness temperature of the region of the planet that is blocked by the A and B rings and that of the unblocked portion of the planet. As was the case with the Owens Valley results, the Hat Creek model fitting results are given in terms of absolute brightness temperature and brightness temperatures normalized by the brightness temperature of the unblocked planet. The normalized brightness temperatures should be unaffected by any errors in the absolute calibration scale used to make the observations.

TABLE 13

RESULTS OF MODEL FITTING (1.30 cm)

Model	T_B Planet	T_B Planet Blocked by C Ring	T_B Planet Blocked by A + B Ring	T_B C Ring	T_B B Ring	T_B A Ring	T_{DISK} †	Improvement in Residuals Relative to Model 1 (percent)
1	150.0 ± 1.0 (1.000 ± 0.007)	-	52.9 ± 6.1 (0.353 ± 0.041)	-	6.0 ± 1.1 (0.040 ± 0.008)	6.0 ± 1.1* (0.040 ± 0.008)	140 K	-
2	150.2 ± 1.0 (1.000 ± 0.007)	-	52.6 ± 6.1 (0.350 ± 0.041)	-	1.8 ± 4.1 (0.012 ± 0.027)	11.7 ± 5.2 (0.078 ± 0.035)	140 K	0.1
3	148.4 ± 1.4 (1.000 ± 0.009)	240.2 ± 34.0 (1.619 ± 0.229)	21.2 ± 13.1 (0.143 ± 0.088)	-23.9 ± 7.6 (- 0.161± 0.051)	11.1 ± 2.0 (0.075 ± 0.013)	11.1 ± 2.0* (0.075 ± 0.013)	140 K	1.4
4	148.4 ± 1.4 (1.000 ± 0.009)	251.2 ± 34.6 (1.691 ± 0.233)	17.5 ± 13.3 0.118 ± 0.090)	-40.8 ±12.4 (- 0.275± 0.083)	25.9 ± 8.8 (0.175 ± 0.060)	0.2 ± 6.6 (0.001 ± 0.044)	140 K	1.7

* A and B ring combined into single ring

† $T_{DISK} = \frac{\lambda^2}{2k} \times \frac{\text{Model Flux Density}}{\text{Solid Angel of Elliptical Disk with AENA Radii}}$

An examination of Table 13 will show that the results of Model 1 are the most reliable ones. In Model 2, the brightness temperatures of the A and B rings are solved for separately. In this solution, the A ring is much brighter than the B ring, which is inconsistent with the Owens Valley results. The correlation coefficient between the brightness temperatures of the two rings is quite high, and in view of this, the results are probably not real. The addition of the C ring parameters to the model fits to Models 3 and 4 again result in unreal appearing and, in some cases, physically implausible results. Again, the correlations between the parameters are quite high and are probably responsible for the erroneous results. Thus, it appears from the model fitting results that no models more complicated than Model 1 can be reliably fit to the Hat Creek data.

The reason for this inability to fit the same models to the Hat Creek data that were fit to the Owens Valley data is apparent; the Hat Creek data set is simply not as sensitive to the various model regions as the Owens Valley data set. This fact is expressed mathematically through the high correlation coefficients of the model fit, but it has also been found, by examining plots of the data and various models, that adding or neglecting the C ring does not affect the visibility function of the Saturn models by a significant amount relative to the data errors. The lack of sensitivity of the Hat Creek data set relative to the Owens Valley data set is probably the

result of the poorer resolution of the Hat Creek interferometer and the less favorable geometry for viewing the planet. The poorer resolution means that model components that are of similar shape, size and position are not as readily separated by the interferometric data, and the lower tilt angle of the rings tends to make these similarly shaped regions even more highly correlated. Thus, it appears that the Hat Creek observations will be unable to extend some of the Owens Valley results to shorter wavelengths.

The lack of consistent results for Models 2, 3 and 4 raises some questions about the believability of Model 1's results. To test whether the parameters in this model are really required to fit the Hat Creek data set, Models 0A and 0B have also been fit and their results are given in Table 14. Model 0A consists of only the planet and does not include the rings or the possibility of the rings blocking any planetary emission. Model 0B also does not include the rings, but it does permit the region where the rings block the planet to have a brightness temperature that is different from the remainder of the planet.

The results of Models 0A and 0B are consistent with those of Model 1. The sum of the squares of the residuals to Model 0A is much higher than both Model 0B and Model 1. This is a fairly clear indication that at least the effect of the rings blocking the planetary emission is required in order to fit the data satisfactorily. The difference between the sum of the squares of the residuals to Model 0B

TABLE 14

RESULTS OF MODELS WITHOUT RINGS (1.30 cm)

Model	T_B Planet	T_B Planet Blocked by A + B Ring	T_{DISK}†	Improvement in Residuals Relative to Model 1 (percent)
OA	139.6 ± 0.6 (1.000 ± 0.004)	-	138 K	-23.7
OB	151.0 ± 1.0 (1.000 ± 0.007)	56.3 ± 6.2 (0.373 ± 0.041)	137 K	- 3.2

† $T_{DISK} = \frac{\lambda^2}{2k} \times \frac{\text{Model Flux Density}}{\text{Solid Angle of Elliptical Disk with AENA Dimensions}}$

and Model 1 is smaller, but it is still probably significant and indicative of the fact that the rings are also required to fit the data. In addition, since the brightness temperatures of the unblocked planet and the blocked region are nearly the same in Model 0B as in Model 1, it is quite likely that the results of Model 1 are real.

Model 1 shows all of the features of the brightness temperature structure of Saturn that were known, or suspected, before the observations were made. The brightness temperature of the planet at 1.30 cm is less than has been determined at longer wavelengths. This result was known previously and is due to the temperature structure, and apparently, the distribution of ammonia in the atmosphere of Saturn (Gulkis and Poynter, 1972). The absolute value of the planet's brightness temperature is higher than its disk temperature since the disk temperature does not take the blockage of the planetary emission by the rings into account. This effect was also observed at 3.71 cm in the Owens Valley data set. It indicates that the rings and their effects on the planetary emission should be taken into account when the disk temperatures are interpreted.

The ring brightness temperature of Model 1 is consistent with what was expected at this wavelength in that it is very low compared to the planet's brightness temperature and to the brightness temperature of the rings at infrared wavelengths. In fact, the normalized ring brightness temperature determined at 1.30 cm is in

excellent agreement with the 3.71 cm values. The agreement suggests that the rings do not change brightness, relative to the planet, by more than about 1% of the brightness temperature of the planet between the wavelengths of 1.30 and 3.71 cm. It may also indicate that the brightness temperature of the rings does not change significantly with ring tilt angle between the values of 15.3 and 26.5 degrees.

The optical thickness of the combined A and B ring that is implied by the normalized brightness temperature of the region of the planet which is blocked by the rings is 0.27 ± 0.04. If the rings are assumed to have an intrinsic normalized brightness temperature of 0.04, then this value is revised to 0.31 ± 0.04. This value refers to some sort of average of the A and B ring optical depths. If the brightness temperature of the region blocked by the combined A and B ring is taken to average according to the relative areas of the regions that block the planet and the A ring optical depth is assumed to be half of the B ring optical depth, then the B ring optical depth implied by this value is 0.40 ± 0.06. This result is much lower than the Owens Valley results at 3.71 cm and, if interpreted literally, says that the ring optical depth decreases by a factor of 2 between 3.71 cm and 1.30 cm. This result, if it were real, could place strong constraints on the sizes of the rings particles. However, it is quite possible that these results are affected by features of the

Saturn brightness structure that are not included in Model 1 and that this has caused the result to be different from that of the Owens Valley data set. This possibility will be explored further in the discussion of the effects of an offset in the planet's position on the aperture synthesis analysis of the data set, and an explanation of the apparent difference between the Hat Creek and Owens Valley results will be offered.

The results of the model fitting to the Hat Creek data set are disappointing in that they do not permit all of the Owens Valley results to be extended to the shorter wavelength. The results do contain the important information that the rings do not change their brightness, relative to that of the planet, between the 3.71 cm Owens Valley wavelength and the 1.30 cm Hat Creek wavelength. The similar results for the Hat Creek and Owens Valley observations may also indicate that the ring brightness temperature does not change with ring tilt between the values of 15.3 and 26.5 degress. Finally, the rings apparently attenuate the emission from the planet. This implies that they have a significant optical depth, although the exact value of the optical depth may be affected by features of the brightness structure that are not included in the models, such as an offset in the position of the planet. This point will be considered in greater detail in the discussion of the aperture synthesis analysis of the Hat Creek data.

(ii) Models to Test for the Presence of Limb-Darkening

The presence of limb-darkening of the planetary emission could have important consequences for the entire model fitting analysis as well as for the study of the atmosphere of Saturn. It is possible that the unmodeled limb-darkening, if it exists, could affect the other model fitting results, and therefore, it is important to determine whether these effects occur. It is also important to determine the amount of any planetary limb-darkening since it contains important information about the atmospheric temperature and opacity structure. For these reasons, models including the effects of limb-darkening have been fit to the Hat Creek data set.

Limb-darkening has been approximated by allowing the radius of the uniformly bright planet to vary in the model fits. An interferometer responds to a limb-darkened disk in nearly the same way that it responds to a slightly smaller disk. Thus, a fit for the planetary radius, which shall be called the effective disk radius, will indicate whether limb-darkening is present. As was the case with the Owens Valley fit, however, a difference of less than about 0.5 percent between the effective disk radius and the nominal radius cannot be considered significant, since the radius of Saturn is known imperfectly.

In order to determine how much limb-darkening is implied by a given effective disk radius, a disk that was limb-darkened according to

$$\frac{I(\mu)}{I(1)} = 1 + D - D\mu ,$$

where μ is the cosine of the angle of incidence, $I(\mu)$ is the intensity of the planetary emission for a given μ and D is the limb-darkening coefficient, was fit to a uniformly bright disk of variable radius using the u-v coverage obtained by the Hat Creek data set. This method was also used in the case of the Owens Valley data but was repeated for the Hat Creek data since the relationship between D and the effective disk radius depends upon the data set used. The limb-darkening coefficient that is best fit by a particular effective disk radius for the Hat Creek data set is shown in Figure 21. Also shown are the values determined from the 1976 Owens Valley data set. The Hat Creek and Owens Valley data sets give a similar relationship between the limb-darkening coefficient and the effective disk radius, but they are different in detail and demonstrate that the relationship should be found empirically since it seems to depend upon the sampling of the u-v plane.

The effective disk radius of the planet was fit to the Hat Creek data using the same procedure that was applied to the Owens Valley data. The disk radius was forced to take on various values and the rest of the parameters were solved for using the usual least squares approach. The method known as brute force least squares was then used to determine the best fitting effective disk radius. The sum of the squares of the weighted residuals are shown in Figure 22 as a function of the effective disk radius. There is a clear minimum in the curve

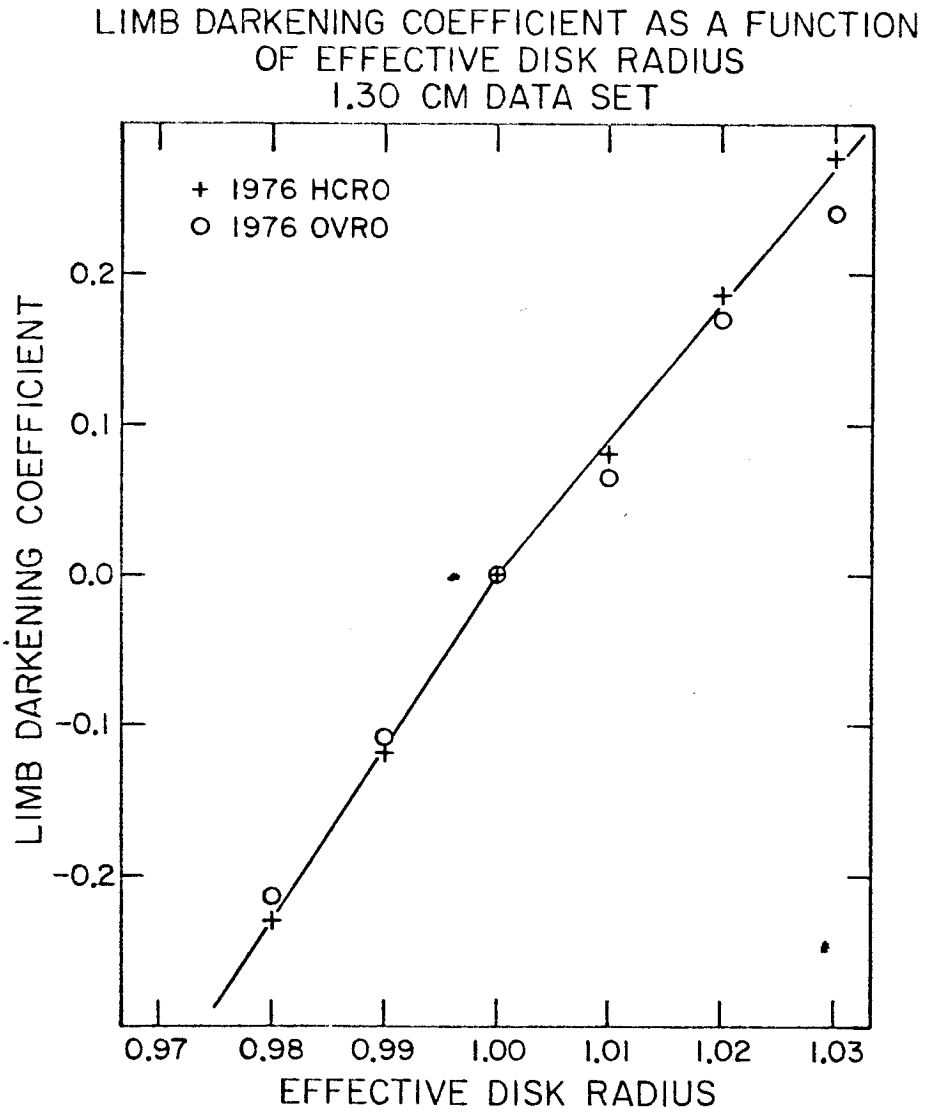

Figure 21 - Results of least squares fit of effective disk radius to limb-darkened disks for the Hat Creek 1.30 cm data set. The results for the 1976 Owens Valley 3.71 cm data set are also shown in the figure for comparison. The lines shown on the figure only represent an approximation of the measured values and are not a best fit to the points in any sense.

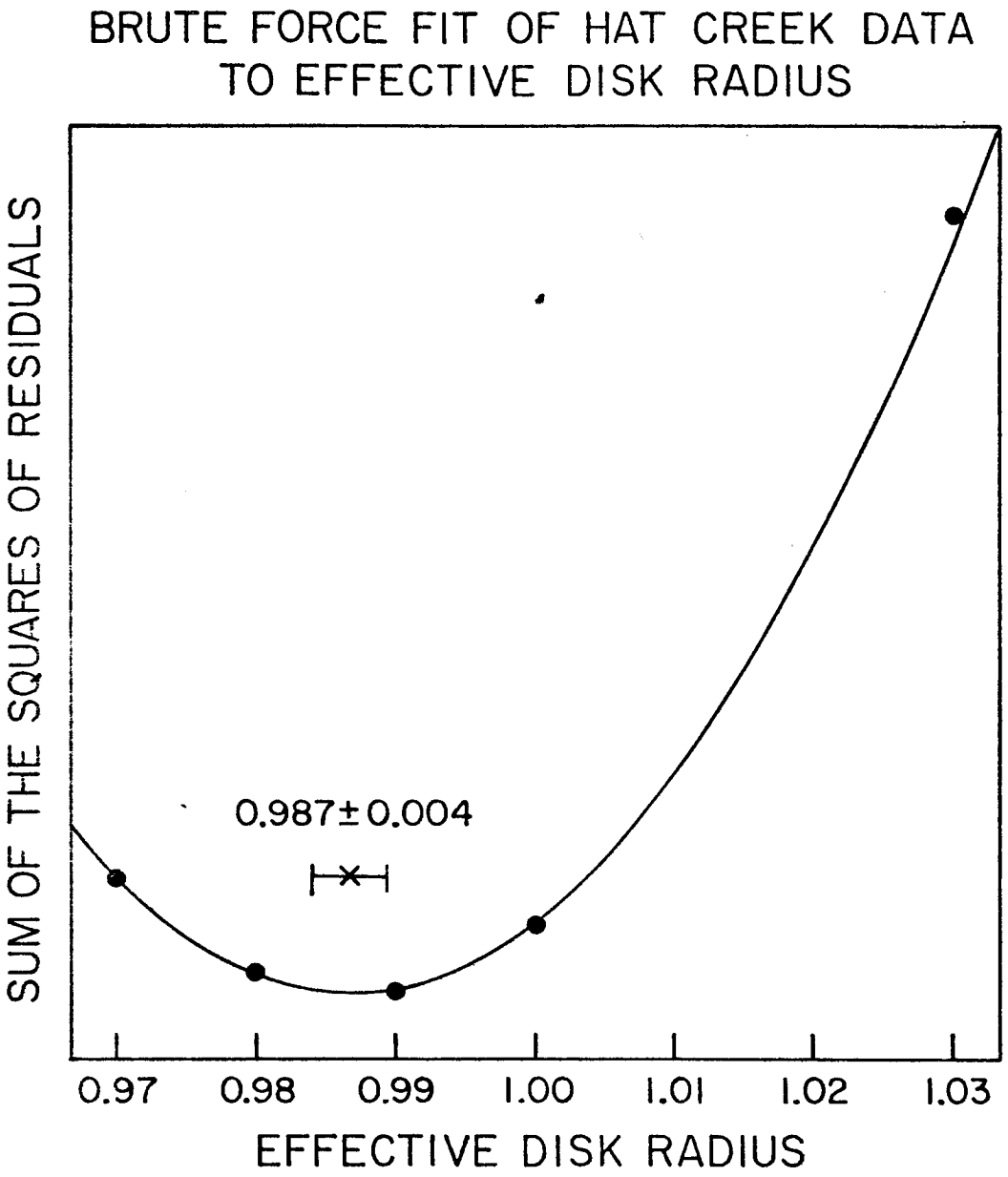

Figure 22 - Sum of the squares of the residuals to the model fits to the 1976 Hat Creek data set plotted as a function of the effective disk radius. The brute force least squares procedure fits a parabola to the lowest three points shown in the figure and uses it to determine the best fitting value of the effective disk radius. The best fitting value is 0.987 ± 0.004.

at a value of about 0.987. The results of the model fits to the brightness temperature regions of Model 1 including the effective disk radius parameters are shown in Table 15.

The best fitting effective disk radius is 0.987 ± 0.004 which suggests that the planet is significantly limb-dark at 1.30 cm wavelength. The model fitting results for the other parameters are slightly affected by the introduction of the effective disk radius parameter, but none changes by more than one standard deviation from the results of the model with the nominal disk radius. Thus, the models which include the disk radius as a parameter indicate that the emission from the planet is probably limb-darkened and that the limb-darkening does not seriously affect the results for the other parameters in the model fit.

The effective disk radius found for the Hat Creek data is significantly different from the value of 1.000 ± 0.004 which was found from the 1976 Owens Valley data set. It is also significantly different from the 1973-1974 Owens Valley result, which is suspected to be inferior to the 1976 Owens Valley result. This difference implies that Saturn is more limb-dark at 1.30 cm than it is at 3.71 cm. If the relationships between the limb-darkening coefficient and the effective disk radius are used, then the limb-darkening coefficients implied by the Owens Valley results are 0.08 ± 0.04 and 0.00 ± 0.05 for the 1973-1974 and 1976 data sets. The limb-darkening coefficient implied by the Hat Creek result is -0.15 ± 0.05. The Owens Valley

TABLE 15

MODEL 1 INCLUDING EFFECTIVE RADIUS (1.30 cm)

T_B Planet	150.8 ± 1.1 (1.000 ± 0.008)
Effective Radius	0.987 ± 0.004
T_B Planet Blocked by A + B Ring	57.0 ± 6.8 (0.378 ± 0.045)
T_B A + B Ring	7.0 ± 1.3 (0.046 ± 0.008)
T_{DISK} †	140 K
Improvement in Residuals Relative to Model 1 (percent)	1.0

† $T_{DISK} = \frac{\lambda^2}{2k} \times \frac{\text{Model Flux Density}}{\text{Solid Angle of Elliptical Disk with AENA Dimensions}}$

results are in the range that could be entirely explained by an error in the nominal Saturn radii of Cook et al. (1973). The Hat Creek results, however, are both outside of this range and significantly different from the Owens Valley values. Thus, the most likely interpretation of all of the results is that the 3.71 cm planetary emission is not significantly limb-dark while the 1.30 cm emission is. This finding is interesting since models of the atmospheres of Jupiter and Saturn which fit the microwave spectrum give less limb-darkening at 1.30 cm than at 3.71 cm (Berge and Gulkis, 1976; Olsen, private communication). The wavelength dependence of the limb-darkening that is inferred from this study may have interesting implications for the atmsophere of Saturn.

VII. ANALYSIS OF THE HAT CREEK 1.30 cm OBSERVATIONS BY APERTURE SYNTHESIS TECHNIQUES

a) Introduction

One of the principal goals of the Hat Creek observing program was to produce an aperture synthesis map of the Saturn system. As has been stated previously, an aperture synthesis map allows the brightness structure of a radio source to be determined in a manner that is free from any assumptions about it. This model independence of the aperture synthesis method allows it to be used to search for brightness structures which were unrecognized previously as well as to provide a confirmation of the model fitting results.

In addition to providing a confirmation of the model fitting results, the Hat Creek aperture synthesis maps may be expected to confirm the apparent offset of the position of Saturn from the value predicted by the American Ephemeris and Nautical Almanac (AENA) that was suggested by the Owens Valley maps. Such an offset is expected to be systematic in nature, and since the Hat Creek data were obtained only five months after the Owens Valley data, it should be present in the Hat Creek map. An offset in the position of Saturn from the nominal AENA position might have important consequences for the model fitting analysis. In the Owens Valley model fitting, it was seen that the brightness temperature of the region of the planet blocked by the C ring was the parameter in the model fits that was most affected by the position offset. In the case of the Hat Creek

analysis, it might be expected that the region of the planet blocked by the A and B rings could be similarly affected and that a position offset could be the cause of the apparently low optical depth found by the model fitting. If this were the case, then the position offset discovered by the maps would have great implications for the ring particles as well as for the AENA geocentric ephemeris of Saturn.

b) Aperture Synthesis Procedures

The aperture synthesis mapping of the Hat Creek data was carried out in the same manner as the mapping of the Owens Valley data. The measured visibility function was Fourier transformed and "cleaned" to produce a map of the radio emission from Saturn that was as free as possible from the effects of the sidelobes of the synthesized (DIRTY) beam. The u-v coverage obtained by the observations at Hat Creek was shown previously in Figure 20. The synthesized beam produced by the u-v coverage is shown in Figure 23. There is a ring of 10 to 15% sidelobes around the main beam and this is similar to the appearance of the Owens Valley synthesized beam. The largest sidelobes lie to the north and south of the main beam and are nearly 30% of the peak response. Fortunately, they are situated about 30 arcsec away from the main beam, and since Saturn's polar diameter is less than 20 arcsec, they should not interfere with the map. This is in contrast to the largest sidelobes in the Owens Valley beam which were at about the 35% level and adjacent to the main beam. The lack of such sidelobes causes the Hat Creek

Figure 23 - Contour map of the synthesized beam of the 1976 HCRO aperture synthesis experiment. The contour levels are 90%, 70%, 50%, 30%, 10%, -10%, and -30% of the peak response. The interval between the tick marks at the edge of the map is 10 arcsec for Saturn at the standard distance of 8 AU.

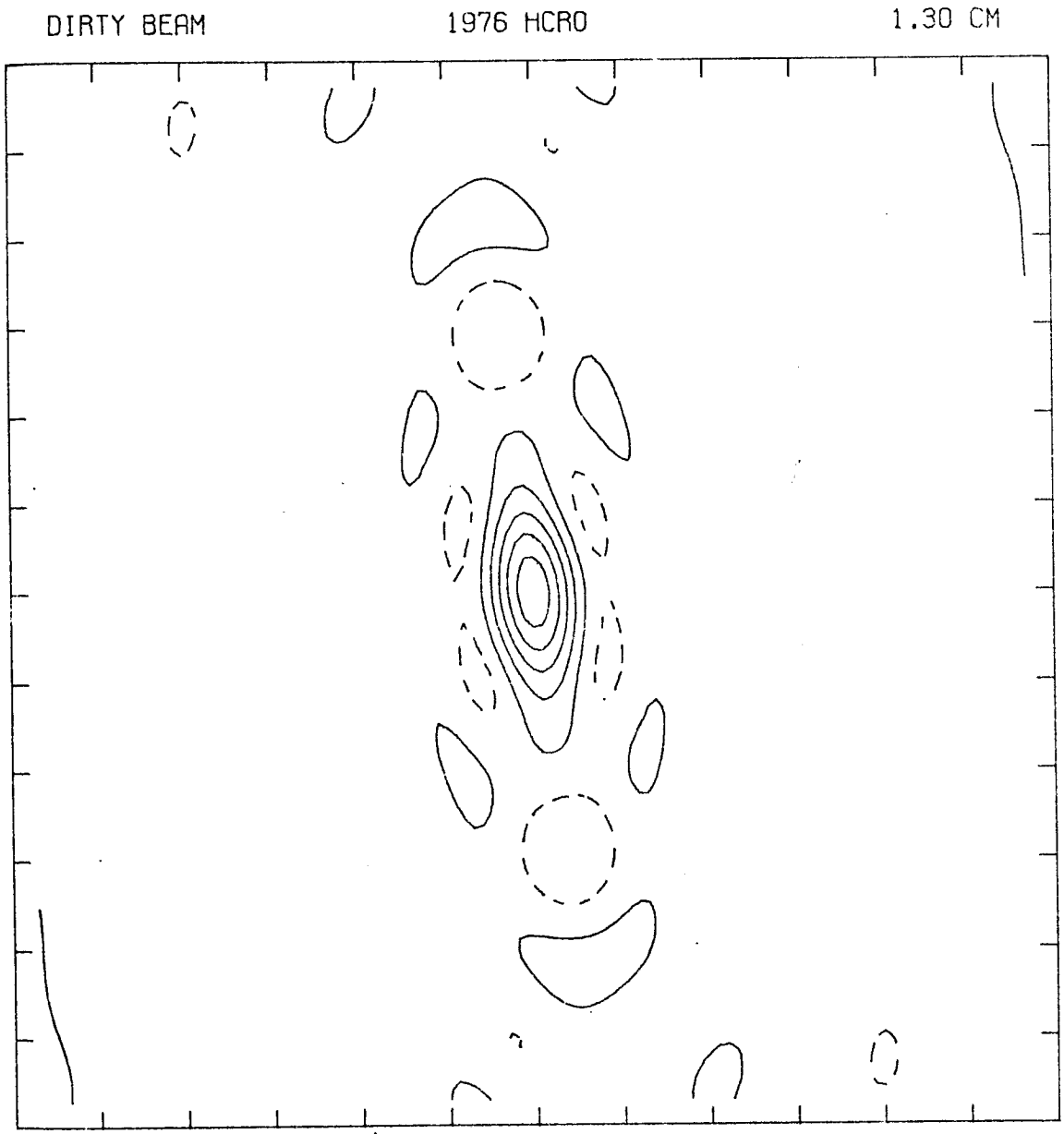

Figure 23

DIRTY map to have a much more satisfactory appearance than the Owens Valley DIRTY map.

The DIRTY map is shown in Figure 24, and it contains some interesting features. The centroid of the emission is apparently displaced to the south of the center of the map, and the contours are somewhat wider in the south as well. These features are consistent with the effects expected from the blockage of the northern hemisphere of the planet by the rings. In addition to these features, it is also apparent from the DIRTY map that the rings are not present at the level of the lowest contour in the map (5% of the peak response). Thus, even the Hat Creek DIRTY map shows important structures in the radio emission from Saturn, and this fact permits the subsequent cleaning and analysis to be done with confidence.

A CLEAN map of the Hat Creek data is shown in Figure 25. The cleaning of the Hat Creek map was done in exactly the same manner as the cleaning of the Owens Valley map. CLEAN is an iterative deconvolution process that chooses a collection of point sources which, when convolved with the DIRTY beam, will give the DIRTY map. The point sources chosen are constrained to lie in a 50 x 22 arcsec (dimensions refer to Saturn at the standard distance of 8 AU) box which includes the planet and the rings. Each iteration of CLEAN removed 30% of the response of the DIRTY beam from the largest deflection remaining in the map. 500 iterations were performed, and as was the case with the Owens Valley map, the number of iterations did not affect the appearance of the map after a certain point. The

Figure 24 - 1976 HCRO aperture synthesis map of Saturn. The map represents the convolution of the true brightness structure of Saturn with the synthesized beam shown in Figure 23. The peak response in the map is 4.85 Jy, and the contour levels are 95%, 85%, 75%, 65%, 55%, 45%, 35%, 25%, 15%, 5%, -5%, and -15% of the peak response. Saturn is at the center of the map and the horizontal (x) and vertical (y) axes of the map are aligned with the major and minor ring axes, respectively. x increases to the left and is toward Saturn's east limb, and y increases to the top and is toward its north limb. The interval between the tick marks at the edge of the map is 10 arcsec for Saturn at the standard distance of 8 AU.

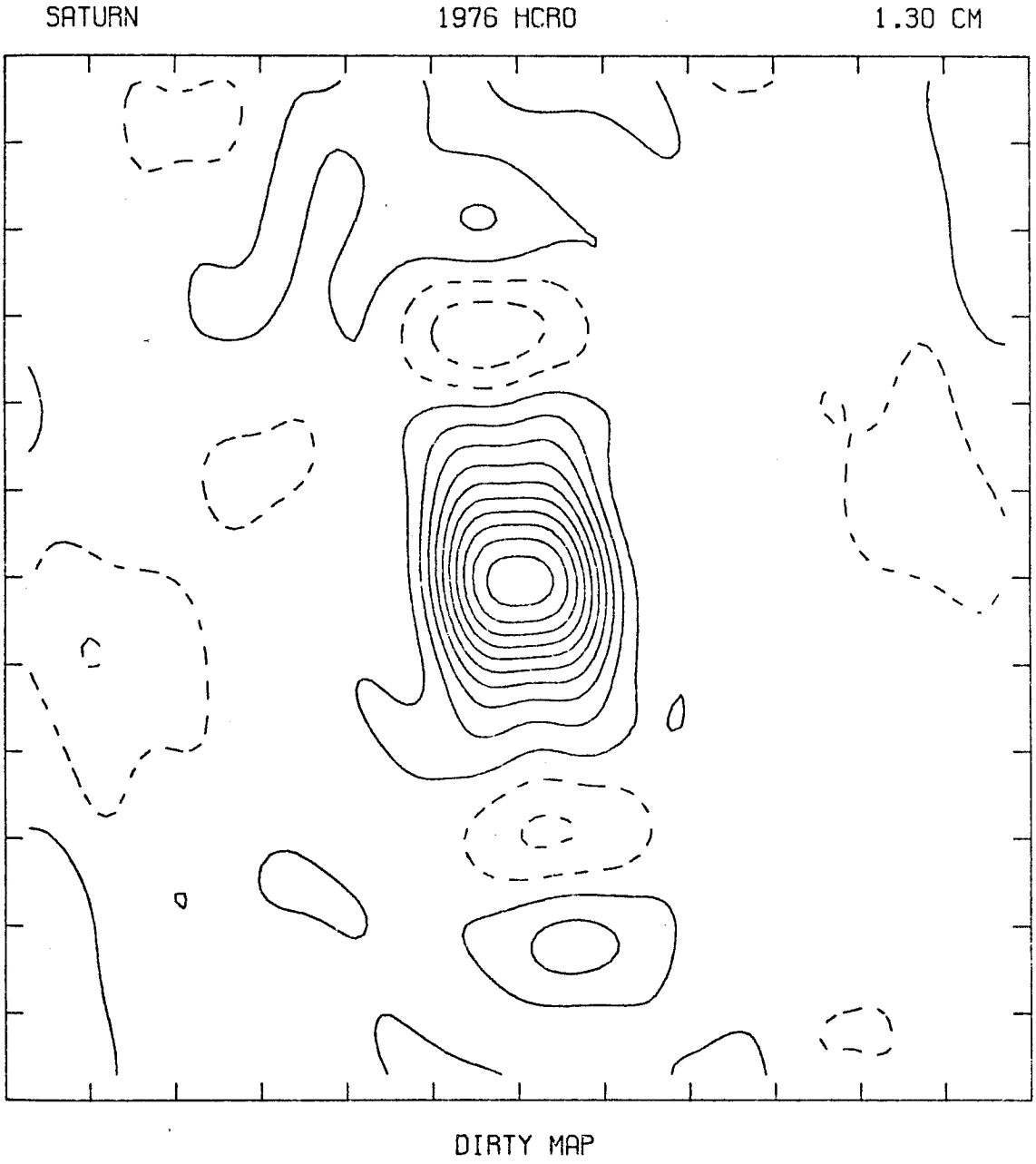

Figure 24

Figure 25 - CLEAN 1976 HCRO aperture synthesis map of Saturn. The map of Figure 24 has been deconvolved with the synthesized beam of Figure 23 and the result is reconvolved with a gaussian beam. The dimensions (HPBW) of the gaussian, CLEAN beam are 8 arcsec in the horizontal (x) direction and 15 arcsec in the vertical (y) direction. The deflections in the map are given in the units of brightness temperature and represent the brightness temperature of the source averaged over the CLEAN beam. The contour values are 110K, 90K, 70K, 50 K, 30K, 10K, 3K, -3K. Dashed contours represent negative values. Saturn is at the center of the map and the x and y map axes are aligned with the major and minor ring axes, respectively. x increases to the left and is toward Saturn's east limb, and y increases to the top and is toward its north limb. The interval between the tick marks at the edge of the map is 10 arcsec for Saturn at the standard distance of 8 AU.

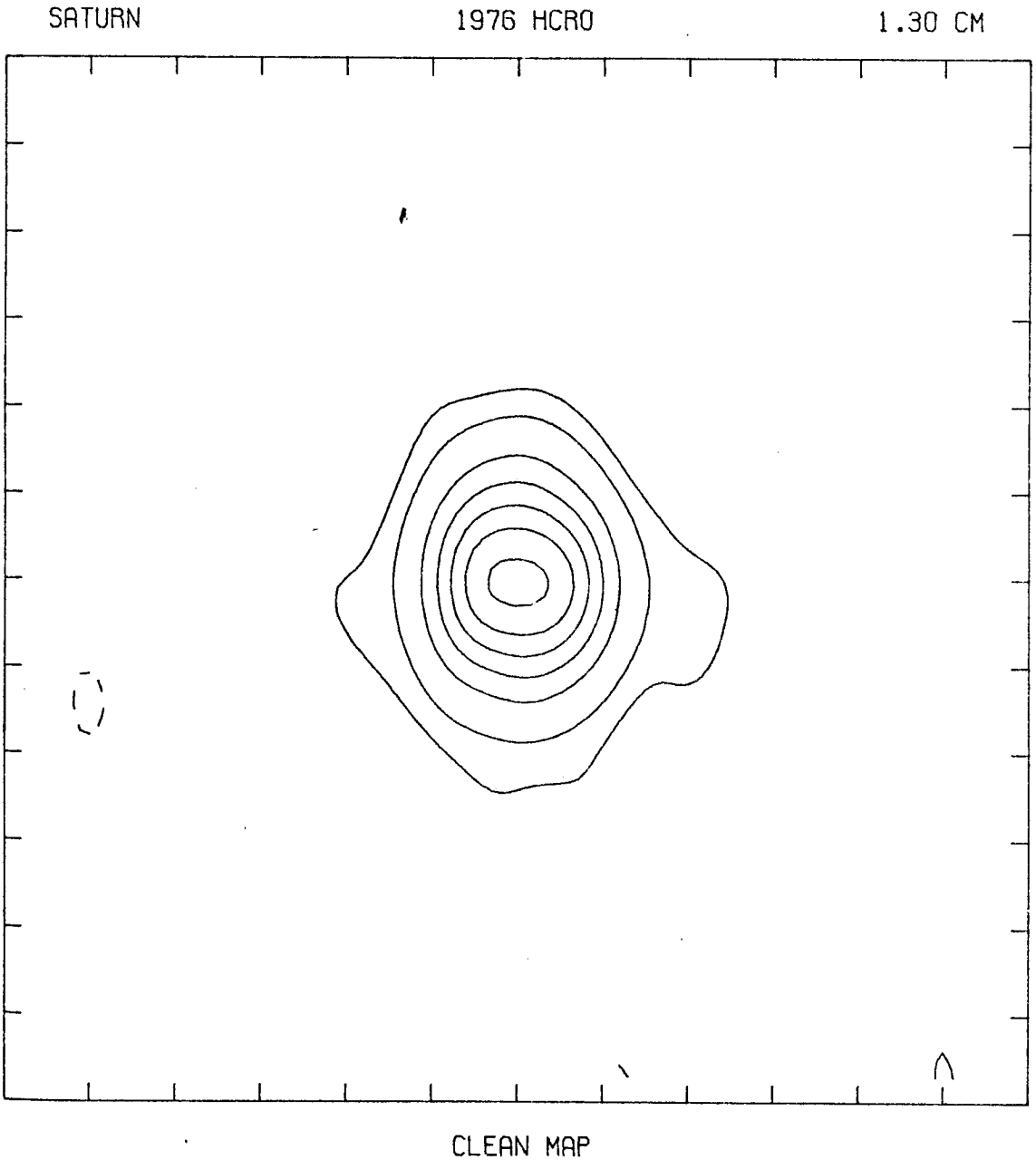

Figure 25

point sources that were iteratively removed from the map were then returned to it in the form of the response to a sidelobe-free, gaussian beam. Two such CLEAN beams were used in the analysis, and they are identical to those used in the Owens Valley maps since the resolution in the two aperture synthesis experiments is nearly the same. An 8 by 15 arcsec (half power beam width) gaussian beam was used to give a map with the greatest amount of resolution that is available in the data. This is the beam that has been used to produce the CLEAN map of Saturn in Figure 25 . A second CLEAN beam, which is a 15 arcsec (HPBW) circular gaussian beam, was used to produce a map with greater sensitivity to large, low brightness features in the map. Since the RMS deflection in a map is inversely proportional to the solid angle of the beam, the large circular beam should have about twice the sensitivity of the small elliptical beam.

The clean map of Figure 25 and a similar map produced using the circular 15 arcsec beam allow estimates of the sensitivity of the maps to be made. In the case of the Owens Valley maps, the RMS deflection in the maps was estimated in two ways. The best way, which gave the most consistent results, was based upon the peak-to-peak deflections in the map away from the source. The RMS deflection is then estimated to be one-third of the peak-to-peak value. The other method, in which the RMS deflection in the map was more straightforwardly computed, seemed to produce an underestimate of the RMS deflection. This discrepancy is probably due to systematic errors on

the measured visibility function which produce a few large deflections in the map. These large deflections are not as important to a straightforward determination of the RMS deflections in the map as they are to an estimate based on the peak-to-peak variation. Since they are important sources of error, the peak-to-peak method is adopted. Using this method, the RMS deflection in the 8 x 5 arcsec beam maps is about 2 K while the RMS deflection in the 15 arcsec circular beam maps is about 1 K. The RMS deflections given here and the CLEAN maps which will be presented are in units of degrees Kelvin and represent the brightness temperature of the source averaged over the CLEAN beam. The RMS values are about the same as those of the Owens Valley maps and indicate that the sensitivities of the two data sets are quite similar. The RMS values will be used as a guideline for determining which features in the maps are real. However, they should not be used in a strict sense since a one-sigma deflection at the position of the source obviously deserves more consideration than a one-sigma deflection away from the source.

The map in Figure 25 shows deflections, which are probably due to the rings, to either side of the main response to the planet. In order to investigate the effects of the rings on the emission from the planet and the radiation from the rings themselves, however, it is necessary to remove the response to the planet from the map. This has been done in the manner of the Owens Valley maps. The planet is modeled as a uniformly bright elliptical disk at the center

of the map. The dimensions of the disk are taken to be those used in the model fitting analysis. The disk brightness temperature was chosen to be 140 K, which is approximately consistent with both the Hat Creek data and the flux density of Saturn measured by observers using single antennas.

The resulting disk subtraction map which has been cleaned with the 8 x 15 arcsec beam is shown in Figure 26. The map contains three key assumptions: the position of the subtracted disk, the size of the cleaning box and the size and brightness of the subtracted disk. As was the case with the Owens Valley disk subtraction maps, the choice of the brightness temperature and size of the disk subtracted is not very critical to the map. Similarly, the size of the cleaning box is not critical since real features outside the cleaning box would remain in the map. However, the choice of the position of the disk is a sensitive one and small errors in the position of Saturn can cause significant features in the disk subtraction map. This possibility should be kept in mind when viewing the disk subtraction maps.

c) Results and Discussion of the Aperture Synthesis Analysis

(i) Disk Subtraction Maps

The disk subtraction map shown in Figure 26 is reproduced in Figure 27A along with an outline of the planet and the visible A and B rings. Since it is difficult to appreciate the surrounding noise level from contour maps, cross sections through the maps are presented in Figure 28. The map shows a large negative deflection

Figure 26 - CLEAN 1976 OVRO aperture synthesis map of Saturn with the response to a uniformly bright, 140 K disk removed from the center of the map. The dimensions of the disk are the same as those used in the model fitting analysis. The HPBW of the CLEAN beam is 8 arcsec in the horizontal (x) map direction and 15 arcsec in the vertical (y) direction. The deflections in the map are in units of brightness temperature and represent the brightness temperature of the source averaged over the CLEAN beam. The contour values are 5 K, 4 K, 3 K, 2 K, -2 K, -3 K, -4 K, and -5 K. Dashed contours represent negative values. Saturn is at the center of the map and the x and y map axes are aligned with the major and minor ring axes, respectively. x increases to the left and is toward Saturn's east limb, and y increases to the top and is toward its north limb. The interval between the tick marks at the edge of the map is 10 arcsec for Saturn at the standard distance of 8 AU.

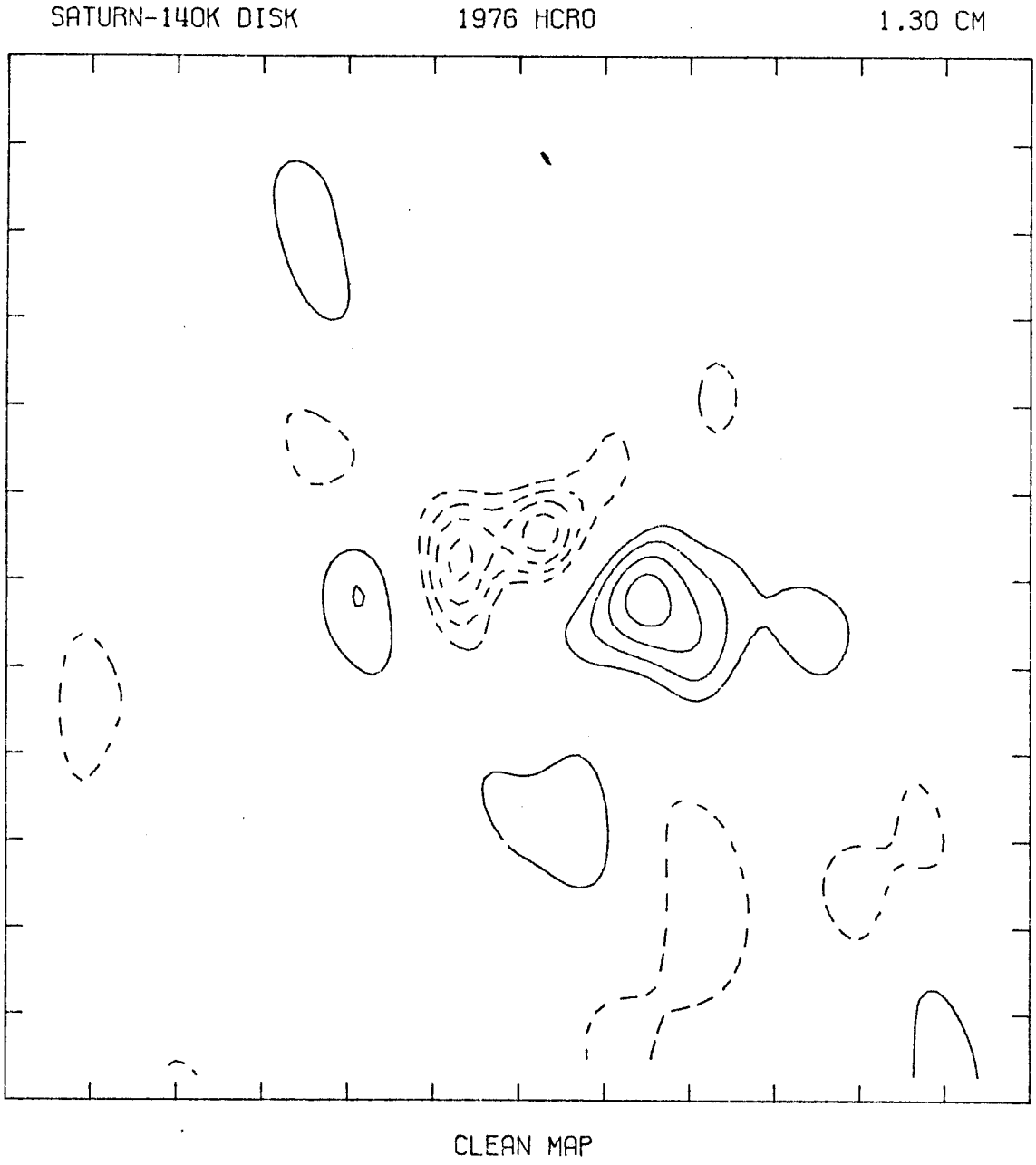

Figure 26

Figure 27A - CLEAN 1976 HCRO aperture synthesis map of Saturn with the response to a uniformly bright, 140 K disk removed from the center of the map. The dimensions of the disk are the same as those used in the model fitting analysis. An outline of the planet and the combined A and B ring as seen at the time of the observations is shown for comparison. The HPBW of the CLEAN beam is 8 arcsec in the horizontal (x) map direction and 15 arcsec in the vertical (y) direction. The deflections in the map are in units of brightness temperature and represent the brightness temperature of the source averaged over the CLEAN beam. The contour values are: 5 K, 4 K, 3 K, 2 K, -2 K, -3 K, -4 K, -5 K. Dashed contours represent negative values. The interval between tick marks at the edge of the map is 10 arcsec for Saturn at the standard distance of 8 AU.

Figure 27B - CLEAN 1976 HCRO aperture synthesis map of Model 1, which is described in Part VI. This map of the best fitting model was produced in exactly the same way as the map of the data, shown in Figure 27A. The beam, contour levels, and scale of the map are identical to those in Figure 27A.

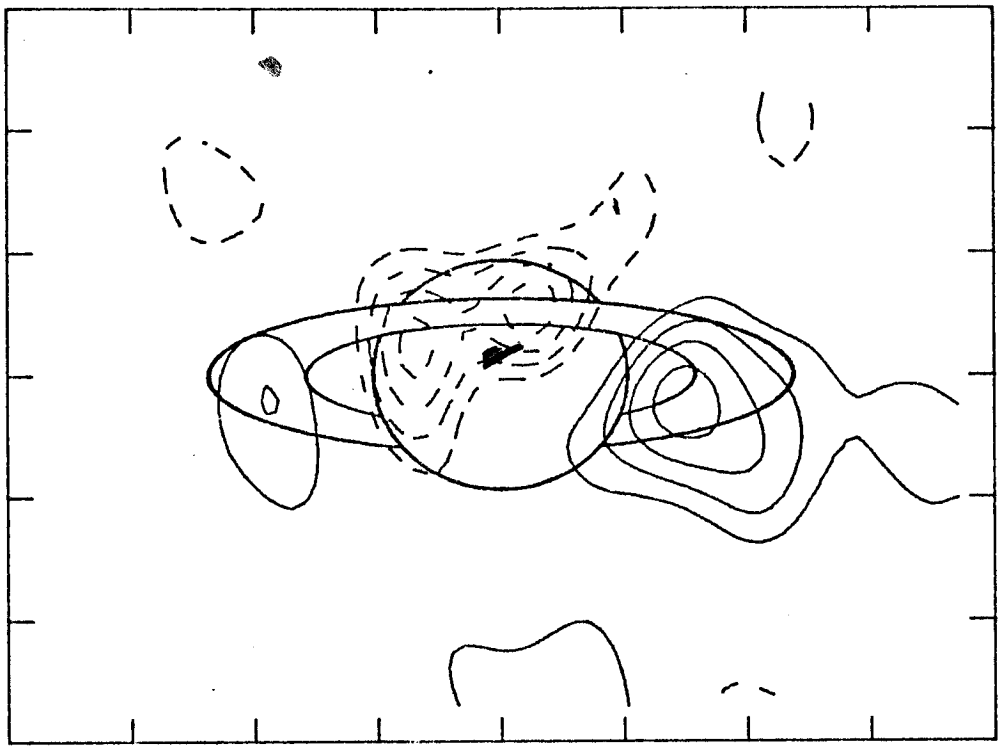

Figure 27A

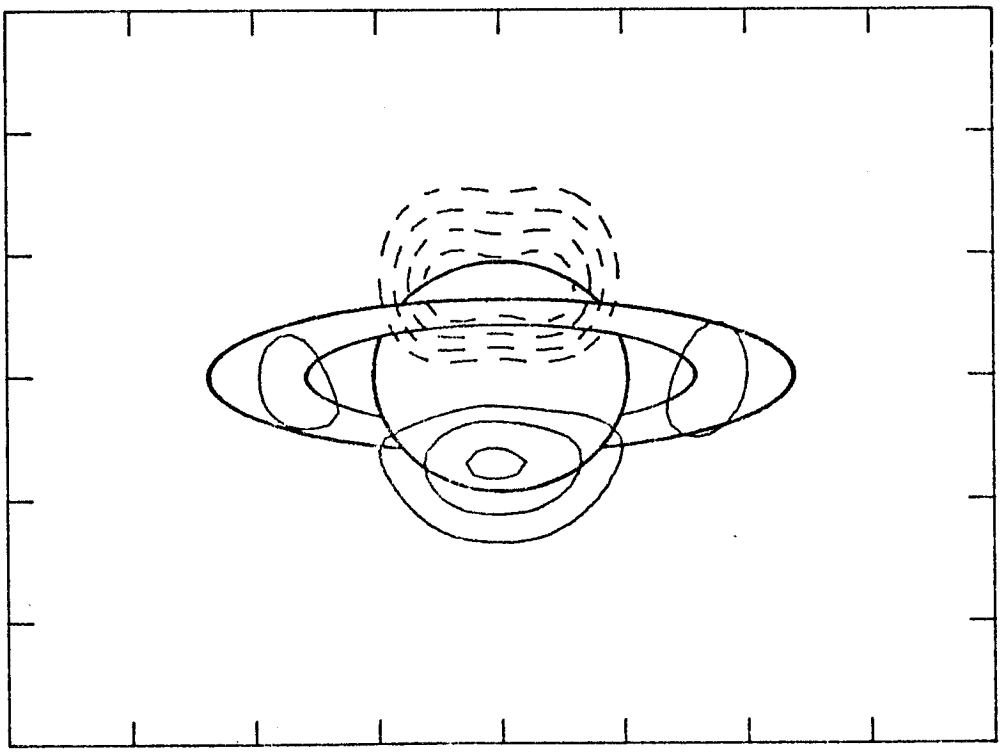

Figure 27B

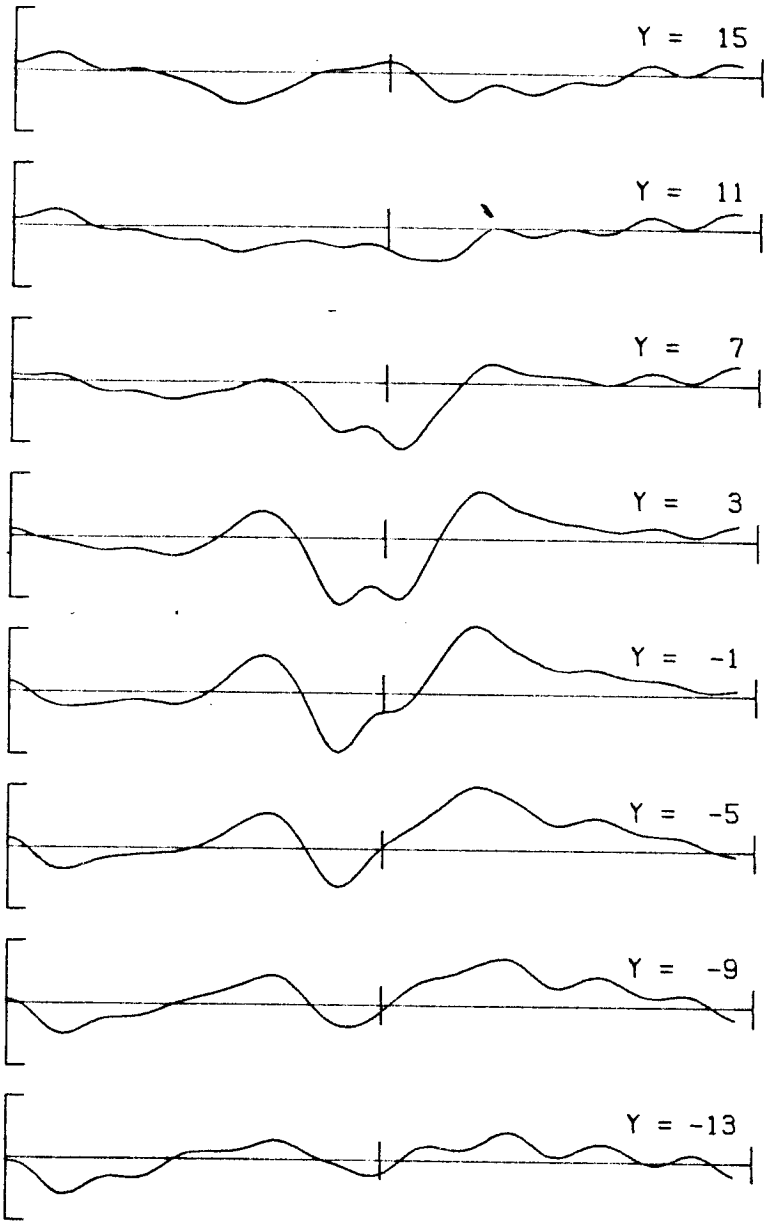

Figure 28 - Horizontal (east-west) cross sections through the 1976 HCRO disk subtraction map shown in Figure 27A. The positions of the cross sections with respect to Saturn are shown approximately in Figure 13A, although at the time of the Hat Creek observations the rings were closed farther than shown in the figure. The horizontal length of the cross sections is 2 arcmin for Saturn at the standard distance of 8 AU. The vertical scale to the left of each cross section represents ±5K of brightness temperature averaged over the CLEAN beam.

where the rings cross the planet and positive deflections to either side at the position of the rings. The negative feature is due to the blockage of the planetary emission by the rings. Since a uniformly bright disk was removed from the map, there has been too much flux removed from the region where the rings block the planet, and as a result, the negative feature appears. The negative feature has a double peaked structure, and it is not symmetric about the central meridian of Saturn. The feature covers a great portion of the planet's eastern half. This same asymmetry was observed in the Owens Valley maps and attributed to an offset of the position of Saturn from the nominal AENA position. This effect will be investigated further in the following sections. The radiation from the position of the rings is also asymmetric, but it appears to be at a significant level on either side of the planet. The western ansa is significantly brighter than the eastern ansa, and this sense of asymmetry is also consistent with what was observed in the Owens Valley maps and attributed to a position offset.

Figure 27B is a map of Hat Creek Model 1 which was prepared in exactly the same manner as Figure 27A. Model 1 consists of the combined A and B rings, the region of the planet where the rings block the planetary emission, and the remaining unblocked portions of the planet. The best fitting brightness temperatures of these regions of Model 1 are given in Table 13. The map in Figure 27B was produced by computing the visibility function of Model 1, subtracting the response

to a 140 K uniform disk from it and Fourier transforming and cleaning the result according to the usual procedure. Basically, the two maps are in good agreement and indicate that the features in the data map which are attributed to the rings are probably real ones. The negative feature in the model map is of about the same magnitude and has the same double-peaked structure as the negative feature in the data map. It is, however, at a slightly different position on the planet. The map of Model 1 contains a positive feature at the southern limb of the planet which is not present in the data map. There are several potential explanations of this feature, but a likely one is that the brightness temperature of the planet in Model 1 is slightly higher than it needs to be in order to satisfy the deflections in the data map. Finally, the features that are due to the rings are difficult to compare with the model because of the large east-west asymmetry. Many of the differences between the data map and the map of Model 1 may be due to the possible offset of the planetary position from the nominal value.

Disk subtraction maps of the data and Model 1 which have been cleaned with the 15 arcsec circular beam are shown in Figures 29 A and B. There are few differences between this set of maps and the set of maps made with the high resolution 8 x 15 arcsec beam. One difference is that the negative feature that is due to the blocking of the disk emission by the rings is no longer double peaked. However, this difference is likely to be due to the lower resolution of the 15 arcsec circular beam. Thus, in this case, the extra sensitivity of the

Figure 29A - CLEAN 1976 HCRO aperture synthesis map of Saturn with the response to a uniformly bright, 140 K disk removed from the center of the map. The dimensions of the disk are the same as those used in the model fitting analysis. An outline of the planet and the combined A and B ring as seen at the time of the observations is shown for comparison. The HPBW of the CLEAN beam is 15 arcsec in the horizontal (x) map direction and 15 arcsec in the vertical (y) direction. The deflections in the map are in units of brightness temperature of the source averaged over the CLEAN beam. The contour values are: 4 K, 3 K, 2 K, 1 K, -1 K, -2 K, -3 K, and -4 K. Dashed contours represent negative values. The interval between tick marks at the edge of the map is 10 arcsec for Saturn at the standard distance of 8 AU.

Figure 29B - CLEAN 1976 HCRO aperture synthesis map of Model 1, which is described in Part VI. This map of the best fitting model was produced in exactly the same way as the map of the data, shown in Figure 29A. The beam, contour levels, and scale of the map are identical to those in Figure 29A.

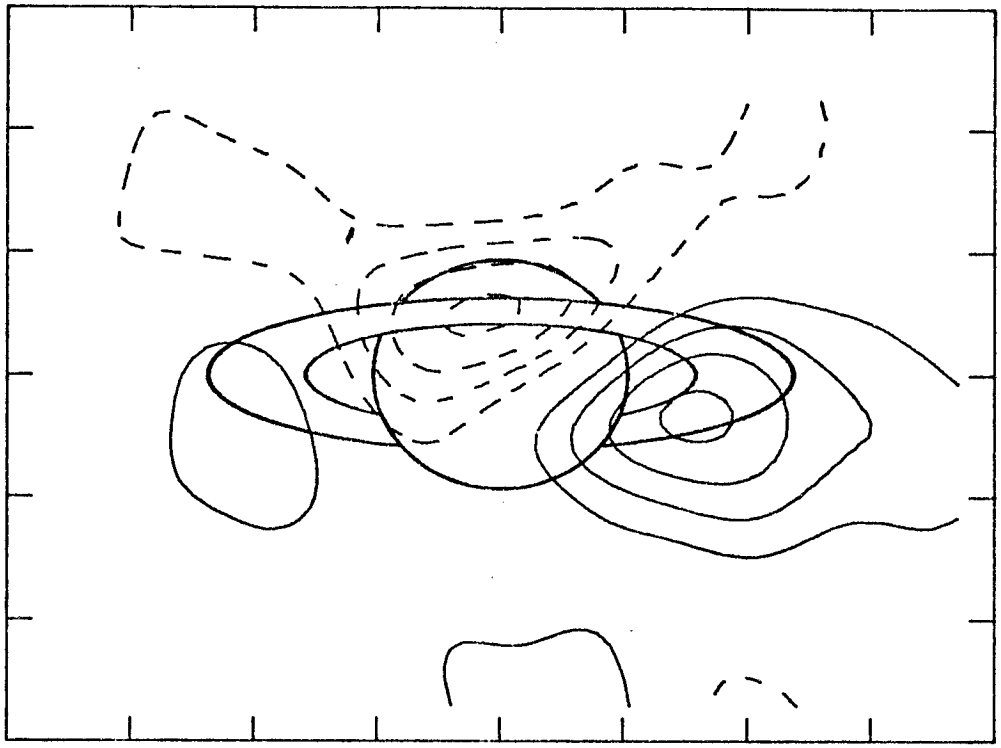

Figure 29A

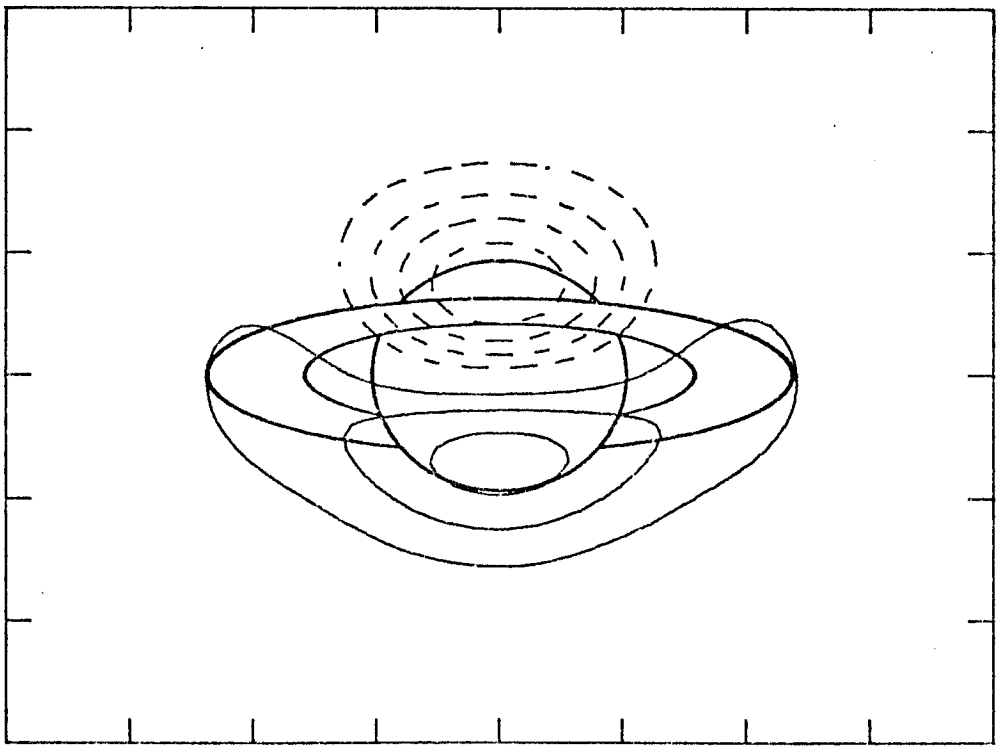

Figure 29B

maps which use the larger beam does not alter the conclusions derived from the high resolution maps.

(ii) Maps of the Residuals to the Model Fits

Comparisons between the data maps and the maps of Model 1 are facilitated by making the maps in Figures 30A and B. These maps are made by Fourier transforming and cleaning the difference between the measured visibility function and the visibility function of Model 1. The residuals map in Figure 30A has been cleaned using the 8 x 15 arcsec beam and the map of Figure 30B has been cleaned using the 15 arcsec circular beam. Cross sections through the map of Figure 30A are shown in Figure 31. The maps show a negative feature on the south-east limb of the planet and a smaller positive feature on the western ansa. There is also a small positive feature near the northern limb of the planet. None of these features is similar to a feature that would be due to one of the brightness regions in Model 1. Thus, it is likely that the features reflect structures in the radio emission from Saturn that are not included in Model 1.

The largest feature in the residuals maps is the negative one on the south-east limb of the planet. This feature is about 3 times larger than the nominal noise level in Figure 30A and about 4 times larger in Figure 30B. The feature is similar in magnitude, shape and position to a negative feature in the Owens Valley residuals map. However, it is displaced to the south of the planet's equator while the Owens Valley feature was centered on the equator. The next largest features are approximately 2 times the noise level and

Figure 30A - CLEAN 1976 HCRO aperture synthesis map of the residuals to Model 1, which is described in Part VI. An outline of the planet and the combined A and B ring as seen at the time of the observations is shown for comparison. The HPBW of the CLEAN beam is 8 arcsec in the horizontal (x) map direction and 15 arcsec in the vertical (y) direction. The deflections in the map are in units of brightness temperature and represent the brightness temperature of the source averaged over the CLEAN beam. The contour values are: 3K, 2K, -2K, -3K, and -4K. Dashed contours represent negative values. The interval between tick marks at the edge of the map is 10 arcsec for Saturn at the standard distance of 8 AU.

Figure 30B - CLEAN 1976 HCRO aperture synthesis map of the residuals to Model 1. This map is the same as that of Figure 30A except that the CLEAN beam is a circular gaussian with an HPBW of 15 arcsec. The contour values in this map are 2 K, 1 K, -1 K, -2 K, and -3 K.

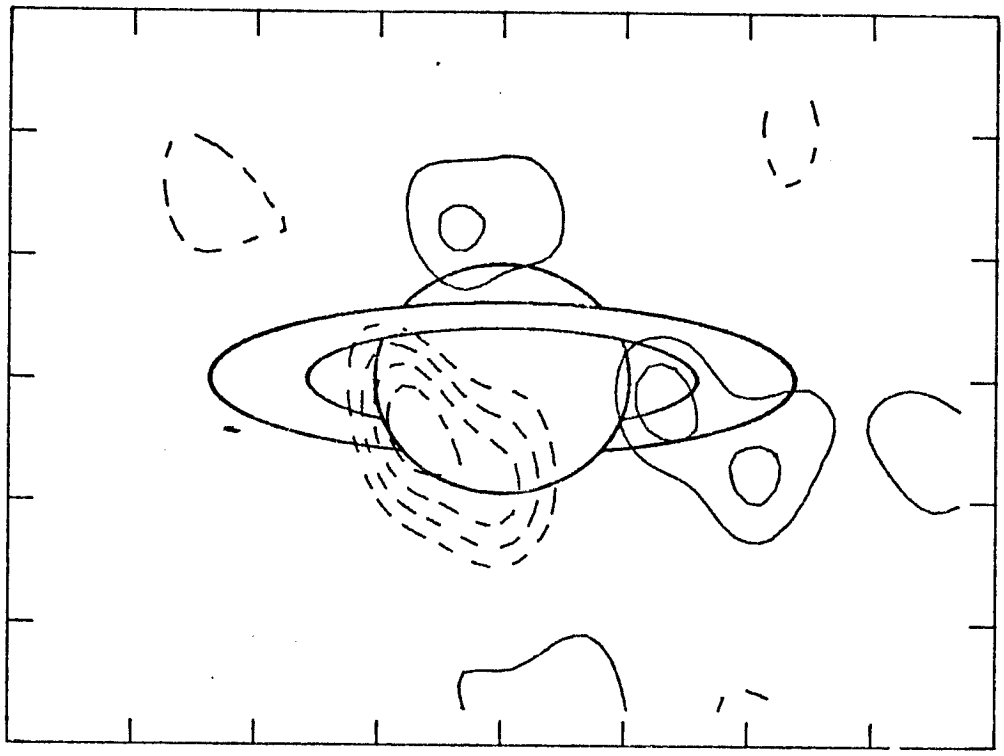

Figure 30A

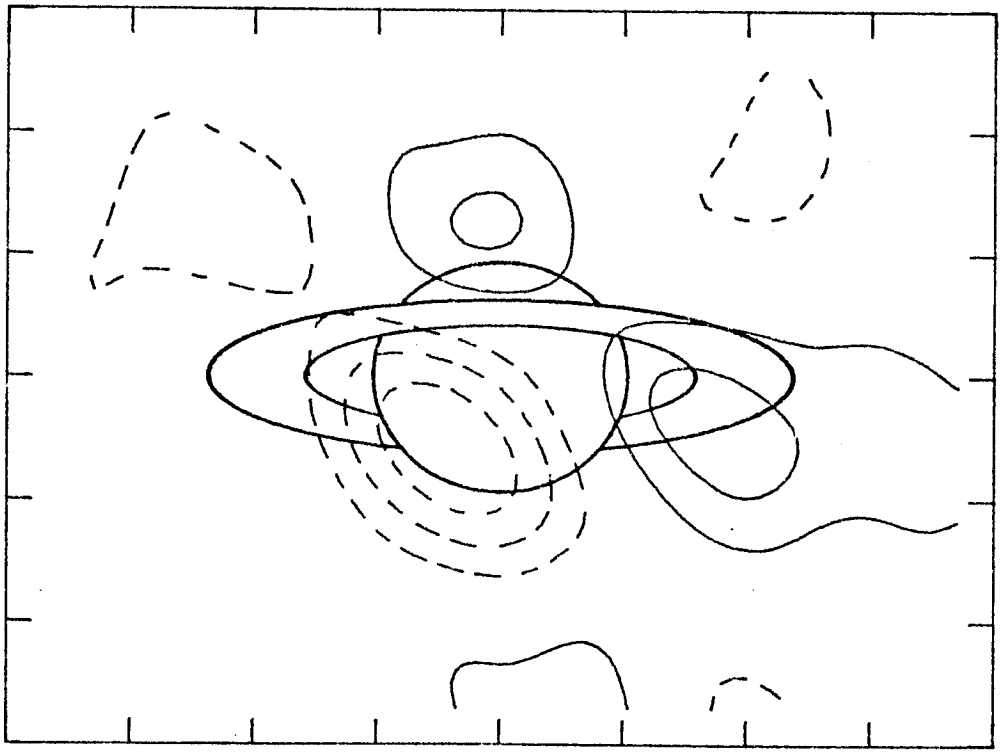

Figure 30B

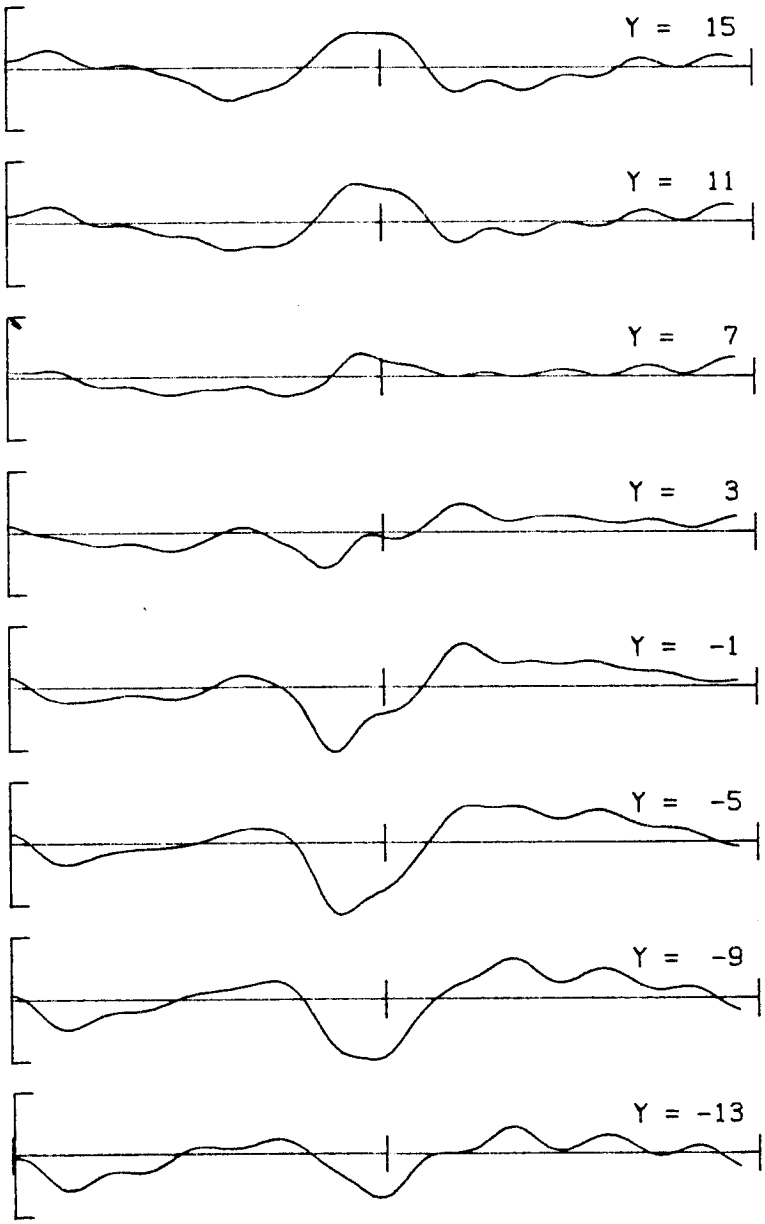

Figure 31 - Horizontal (east-west) cross sections through the 1976 HCRO residuals map shown in Figure 30A. The positions of the cross sections with respect to Saturn are shown approximately in Figure 13A, although at the time of the Hat Creek observations the rings were closed farther than shown in the figure. The horizontal length of the cross sections is 2 arcmin for Saturn at the standard distance of 8 AU. The vertical scale to the left of each cross section represents ±5K of brightness temperature averaged over the CLEAN beam.

situated near the northern limb of the planet and on the western ring ansa. The positive feature on the western ansa is similar in magnitude to a positive feature in the Owens Valley residuals map, but it is shifted to the south of the position of the Owens Valley feature. The other positive feature has no analog in the Owens Valley map, but it must still be considered since it is very near the source. There are no other features in the map which deserve consideration since they do not rise much above the noise and are not very close to the source.

The most likely explanation of the large negative feature on the planet and the small positive feature on the western ansa is the same one which was offered for the similar features in the Owens Valley map. It is possible that these features could have an entirely different explanation; however such a possibility seems unlikely. It was seen, in the case of the Owens Valley maps, that both the positive and negative features could be explained by allowing the planet to be offset from its nominal AENA position. An alternative hypothesis, which could only explain the negative features on the planet, was that the brightness temperature of the planet varies across the disk. The variations in the planetary brightness temperature that are required to match the Hat Creek data are the order of 10 K and this high value makes this hypothesis less attractive than the other. It is possible that the other positive feature in the map can also be explained by a position offset, since it lies at the northern limb of the planet and is opposite an extension of the negative feature.

The positive and negative features to the north and south of Saturn are in the sense which is expected by a position offset in the same direction that was found from the Owens Valley data. Thus, all of the features in the residuals maps may be explained by an offset in the position of Saturn from the nominal AENA position.

(iii) Maps and Models Including a Position Offset

The appearance of the residuals maps of Figure 30 suggests that the true geocentric ephemeris of Saturn may be systematically offset from the positions given in the American Ephemeris and Nautical Almanac (AENA). A systematic offset was also apparently discovered in the residuals maps of the Owens Valley data. In order to determine the extent of the proposed offset and its effect upon the other parameters in the model fit, a brute force least squares technique has been used to fit the data to a model which includes a position offset. Aperture synthesis procedures have also been used to determine whether a model which includes an offset can account for the features in the residuals maps of Figure 30.

The results of the model fitting to the brightness temperature parameters of Model 1 and including a possible offset in the position of Saturn are given in Table 16. The values of the parameters without the offset are also given in Table 16 for comparison. The position offset is given in units of Saturn equatorial radii in the x and y directions in the map, and it is expressed as the correction to the AENA geocentric ephemeris that is required to give the best fit

TABLE 16

MODEL INCLUDING POSITION OFFSET

COMPARED TO MODEL WITH NO OFFSET (1.30 cm)

	Model 1 XY (Includes Position Offset)	Model 1
T_B Planet	153.1 ± 1.0	150.0 ± 1.1
T_B Planet Blocked by A & B Ring	26.4 ± 5.9	52.9 ± 6.2
T_B A & B Ring	6.8 ± 1.2	6.1 ± 1.2
T_{DISK}†	139 K	139 K
X Offset (Equatorial Radii)*	0.028 ± 0.009	-----
Y Offset (Equatorial Radii)*	-0.038 ± 0.009	-----
Percent Improvement in Residuals from Model 1	3.2	-----

† $T_{DISK} = \frac{\lambda^2}{2k} \times \frac{\text{Model Flux Density}}{\text{Solid Angle of Elliptical Disk with AENA Radii}}$

* Equatorial Radius of Saturn is 10.31 arcsec at 8 AU.

to the data. Table 16 shows that the best fitting position offsets are at least three times their errors and that the addition of the offset parameters to the model improves the residuals to the fit significantly. As well, the offset values found for the Hat Creek data are identical to those found for the Owens Valley data within the errors. Thus, the position offsets are quite likely to be the explanation of the features in the residuals map.

As was the case with the Owens Valley data, it is probably impossible to distinguish between a position offset and a variation of the planet's brightness temperature across the disk. However, the brightness temperature variation that is required to match the features in the residuals map is quite large, and therefore, not likely to occur. Further, the brightness temperature variation may be expected to produce only those features situated on the planet, such as the large negative one in the south-east quadrant, while the offset is capable of explaining features that are not on the planet. Thus, the position offset explanation of the features is the more likely one.

The position offsets in terms of right ascension and declination are

$$\Delta\alpha = 0.31 \pm 0.08 \text{ arcsec}$$

$$\Delta\delta = -0.32 \pm 0.08 \text{ arcsec}$$

These values were computed under the assumptions that the average distance to Saturn at the time of the observations was 9.0 AU and that the position angle of its central meridian was -6.7°.

The values are only approximate because an average distance to Saturn was used to compute them. In fact, the distance changed during the observing run, and therefore, the position offset relative to the equatorial radius also changed. These values compare favorably with the offsets predicted by JPL Developmental Ephemeris 96 (X.X. Newhall, private communication) in Part IV, since they are in the same direction and of similar magnitude. The JPL DE-96 offsets are those predicted for June 1, 1976, but the systematic difference between the JPL DE-96 and the AENA should be approximately the same in November, 1976, when the Hat Creek observations were obtained. The similarity between the offset predicted by the JPL DE-96 and the offsets determined by both the Hat Creek and Owens Valley data sets is a good indication that the proposed position offset is real.

The model parameters shown in Table 16 appear to be sensitive to the position of the planet in the model fitting. The ring brightness temperature is the only parameter that does not change significantly when the offset is introduced. The planet brightness temperature increases by about three standard deviations, and the brightness temperature of the region of the planet blocked by the A and B rings decreased by about four standard deviations. These differences are formally significant, and if interpreted literally, they indicate that the parameters are quite sensitive to the position of the planet in the model fit.

It is difficult to be confident of these results since they may simply indicate that the models are not very sensitive to the region of the planet that is blocked by the rings. For example, the least sensitive parameter of the Owens Valley models, the region of the planet that is blocked by the C ring, was found to be the one that was most affected by the position offset. However, in that case the parameter changed by only 1.6 standard deviations while in this case the parameters change by three or more. Thus, the large changes may be an indication that the differences are real.

Another factor which may indicate that the differences are real is the ring optical depth that is implied by the new values. Using these values, the combined ring optical depth is 0.54 ± 0.10 which is in much better agreement with the 3.71 cm optical depths determined in Part III. This value includes a correction for the intrinsic brightness temperature of the rings which is assumed to be 6.8 ± 1.2 K. The similarity between the visible wavelength optical depths and the 3.71 cm optical depth implies that the optical depth at intermediate wavelengths should be comparable, although this is not necessarily the case. Thus, since the new 1.30 cm optical depths are more consistent with the other optical depths, the change in the parameter values with position may be real. This change, then, may provide an explanation of the low 1.30 cm optical depths found in Part VI.

A map of the residuals to the offset model fit is shown in Figure 32. A comparison of this residuals map and the map of Figure 30A shows that the addition of the position offset parameters removes almost all of the features in the map. The only remaining feature that is greater than twice the noise level is located in the north-western quadrant of the map. It is difficult to associate this feature with any real structure on the planet, although one possibility is that the position offset found by the model fitting is slightly incorrect. With this possible exception, the position offset has explained all of the major features in the residuals map, and therefore, no new features that are not included in the models are required to match the data to its accuracy.

(iv) Summary of the Aperture Synthesis Results

Aperture synthesis maps of Saturn and the ring system have been produced from the interferometric observations obtained at Hat Creek. The maps are free from many assumptions about the brightness structure of Saturn that are employed in a model fitting analysis, as were the Owens Valley maps discussed in Part IV. Thus, they may be used to confirm the model fitting results and search for features which have not been included in the models. As with the Owens Valley data, the Hat Creek maps are consistent with the model fitting analysis and do not require any new brightness features, except those due to an offset in the position of Saturn from the nomial AENA values. In particular, no azimuthal variations in the brightness temperature of the rings are required by the data. It is difficult to assess

Figure 32 - CLEAN 1976 HCRO aperture synthesis map of the residuals to Model 1 XY, which is the model fit that includes the apparent offset in the position of Saturn from the nominal AENA values. An outline of the planet and the combined A and B ring as seen at the time of the observations is shown for comparison. The HPBW of the CLEAN beam is 8 arcsec in the horizontal (x) map direction and 15 arcsec in the vertical (y) direction. The deflections in the map are in units of brightness temperature and represent the brightness temperature of the source averaged over the CLEAN beam. The contour values are: 3 K, 2 K, -2 K, -3 K, -4 K. Dashed contours represent negative values. The interval between tick marks at the edge of the map is 10 arcsec for Saturn at the standard distance of 8 AU.

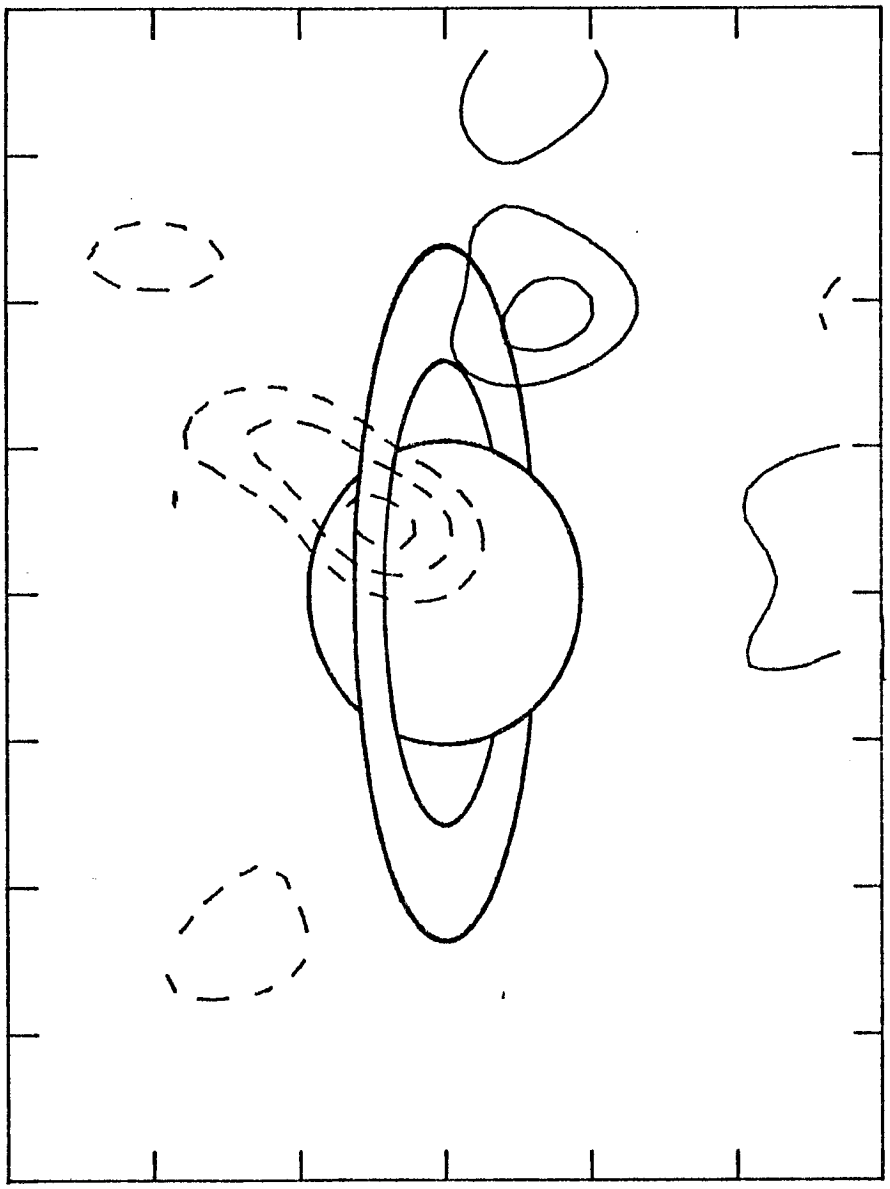

Figure 32

an upper limit on hypothetical variations since the upper limit that is estimated depends upon the model of the variations that is assumed. Proposed models of the rings which include such variations should, therefore, be directly compared to the maps presented here by making a map of the proposed brightness structure.

VIII. DISCUSSION OF THE OWENS VALLEY AND HAT CREEK RESULTS AND THEIR IMPLICATIONS FOR THE RINGS OF SATURN

a) Introduction

The main point of this work has been to determine the principal observational properties of Saturn's rings at centimeter wavelengths. In particular, it is important to measure such properties as the ring optical depth and brightness temperature and determine whether they vary with wavelength. Eventually, the observations made here may be used to constrain solutions for the physical properties of the ring particles. At the present time, however, such solutions would have little meaning since any physical model of the rings contains many parameters, and at present, there are relatively few measurements to constrain their values.

The interpretation of all observations of the rings is uncertain since it is not known whether the rings are many particles thick or only a single particle thick. Each of these limiting cases of what is probably a continuum of possible ring models uses different physical mechanisms to account for the various observations of the rings. The results relating to the ring particles, therefore, depend upon which model is used. Information about the thickness of the rings is rather limited since only an upper limit of about 3 km has been obtained (Lumme and Irvine, 1977). At the present time, the best estimates of the thickness of the rings come from various theoretical arguments which, unfortunately, often lead to divergent conclusions. Multiple scattering and interparticle

shadowing in a many-particle-thick ring provides a natural explanation of many of the visible wavelength observations such as the opposition effect (Kawata and Irvine, 1974) and the change in ring brightness with ring tilt angle (Esposito and Lumme, 1977). However, dynamical studies of the rings (Brahic, 1977; Goldreich and Tremaine, 1977) suggest that collisions between the particles in a many-particle-thick ring would cause it to spread radially until it was only a few (or perhaps one) particles thick. Thus, it is difficult to say which ring model is appropriate, and therefore, it is apparent that the present observations can only be expected to lead to qualitative conclusions about the nature of the ring particles.

That the observations may only lead to qualitative conclusions is not too disappointing since they appear to provide strong constraints upon the ring particle size and composition. In particular, the high radar cross section (Goldstein and Morris, 1973; Goldstein et al., 1976) and microwave opacity and the low microwave brightness temperature of the rings can only be explained if the ring particles are the size of the microwave wavelengths or larger and are composed of either a highly transparent or highly reflective material. Since water ice has been detected as a constituent of the rings (Pilcher et al., 1970) and is known to be highly transparent at microwave wavelengths (Whalley and Labbé, 1969), it is considered to be the most likely constituent of the rings (Briggs, 1974; Pollack, 1975; Janssen and Olsen, 1977). Metallic particles probably could also satisfy the microwave observations (Pollack, 1975; Goldstein et al.,

1976) but there is no other evidence for their presence in the rings. Particles of silicate composition would have to be quite small in order to agree with the low ring brightness temperatures (Pollack, 1975; Janssen and Olsen, 1977), and therefore, they probably could not produce the observed radar cross sections (Cuzzi and Pollack, 1977). At this time, then, the simplest and most consistent explanation of the passive microwave and radar observations is that the particles are composed of water ice and are on the order of the size of the microwave wavelengths or larger. It should be noted, however, that this simple model does not explain all observations of the rings at all wavelengths, and it may not even be able to satisfy the existing radio observations (Janssen and Olsen, 1977). Thus, any information that can be used to refine this simple picture will be important.

The present observations may be expected to refine this simple model in a number of ways. In particular, they may be expected to yield new information about the wavelength dependence of the scattering properties of the ring particles since they are extensive sets of observations made at two wavelengths and analyzed in a consistent manner. The detection of any change in the ring optical depth or brightness temperature with wavelength would place important constraints on the particle size and composition. Even the lack of a wavelength dependence of these properties gives useful information about the particles. The information gained in this manner is somewhat dependent upon the scattering model

used to interpret the observations, but many of the important conclusions are independent of the particular scattering model employed. It is the purpose of this section, then, to point out what properties are consistent with all observations and models and to set the stage for future, more quantitative, studies of the interferometric data presented here.

b) Comparison of the Hat Creek and Owens Valley Results

It was noted in the discussion of the Hat Creek results that the ring brightness temperatures and optical depths found in the Hat Creek and Owens Valley analyses were similar. This finding is quite significant since, if the brightness temperatures and optical depths are the same at both wavelengths, then the properties of the scattering particles in the rings may also be wavelength independent. Therefore, it is important to determine whether the results at the two wavelengths can be explained by the same class of particles. This assertion will probably not be possible to prove in general since the observations were made at different ring tilt angles. It will be difficult, therefore, to separate effects that are due to the difference in wavelength. The comparison between the Hat Creek and Owens Valley observations, then, relies upon the extrapolation of the Owens Valley results to the lower ring tilt angle of the Hat Creek observations.

Since the Hat Creek data were incapable of detecting the C ring, only the results of the model fits without the C ring will be compared. The final results of the Hat Creek and Owens Valley

model fits to models which combine the A and B ring into a single ring are summarized in Table 17. The brightness temperature of the combined A and B ring, when it is normalized by the brightness temperature of the planet, is 0.040 ± 0.008 for the Hat Creek observations. The Owens Valley results are 0.031 ± 0.007 for the 1973-1974 data set and 0.043 ±0.007 for the 1976 data set. The two Owens Valley results are not thought to be significantly different since, when the C ring is added to the model, the two data sets give identical results of 0.041 ± 0.008 and 0.041 ± 0.007 for the normalized brightness temperature of the combined A and B ring. Thus, there is no formal difference between the normalized brightness temperature of the rings determined by the Hat Creek and Owens Valley observations.

The most satisfactory explanation of this result is that the brightness temperature of the rings, relative to that of the planet, does not change significantly with ring tilt angle or wavelength over the ranges that have been observed. Of course, other explanations are possible, but they do not seem as plausible. For example, scattering models of the rings generally indicate that their brightness temperature increases with decreasing ring tilt, if it changes at all. This would require the brightness temperature of the rings to decrease with wavelength by just the right amount to give the same normalized brightness temperature at 1.30 cm that was obtained at 3.71 cm.

TABLE 17

BRIGHTNESS TEMPERATURE AND OPTICAL DEPTH SUMMARY

OF FINAL RESULTS FOR COMBINED A AND B RING

	$\frac{T_B \text{ A+B Ring}}{T_B \text{ Planet}}$	Optical Depth of Combined Ring†
1976 Hat Creek (1.30 cm)	0.040 ± 0.008	0.31 ± 0.04 (0.54 ± 0.10)*
1973-1974 Owens Valley (3.71 cm)	0.031 ± 0.007	0.97 ± 0.16
1976 Owens Valley (3.71 cm)	0.043 ± 0.007	0.59 ± 0.10

† Includes correction for ring brightness temperature of 0.04 ± 0.01. Note that A and B rings cover different relative amounts of the planet in 1973-1974 than in 1976.

* Includes the effect of the position offset.

Such a decrease does not seem likely since a rather special one is required. In addition, the particles are more likely to become more opaque at shorter wavelengths and emit some thermal radiation, which would cause the brightness temperature of the rings to increase with decreasing wavelength. This possibility could be accommodated if the brightness temperature of the rings were allowed to decrease with decreasing ring tilt angle, but as has been said, this possibility is contrary to what is expected based upon simple scattering models. Thus, the simplest and most likely explanation of the result is that the brightness temperature of the rings relative to that of the planet does not vary significantly with wavelength or ring tilt. This explanation implies that, within the uncertainties of the measurements, the scattering properties of the ring particles are the same at 1.30 cm as they are a 3.71 cm.

The conclusion that the scattering properties of the rings are nearly the same at the two wavelengths is strengthened when the ring optical depths are considered. The present observations indicate, but do not require, that the optical thickness of the rings is the same at 1.30 cm as it is at 3.71 cm. This result is not too surprising since the 3.71 cm optical thickness of the rings is comparable to the visible wavelength optical thickness. However, it is difficult to say with certainty that the 1.30 and 3.71 cm optical thickness is the same since the 1.30 cm estimate is strongly affected by an apparent offset in the planet's position from the nominal values given in the American Ephemeris and Nautical

Almanac. Without the offset, the optical thickness of the combined A and B ring is estimated to be 0.31 ± 0.04 while the estimate with the apparent offset included is 0.54 ± 0.10. These results may be directly compared to the result of the 1976 Owens Valley data set since the A and B rings blocked nearly the same relative areas on the planet in the two cases. The 1976 Model 1 result is 0.59 ± 0.10, which is significantly different from the Hat Creek result without the offset. However, the Hat Creek result with the offset included is the same as the 1976 Owens Valley value. Thus, since the aperture synthesis maps suggest that the offset is a necessary feature of the radio emission from Saturn, the models which include the offset are probably the better ones, and the best interpretation of them is that the rings have nearly the same optical thickness at 1.30 cm and 3.71 cm. The same optical thickness is typical of the estimates made at visible wavelengths.

c) Comparison of Results with Those of Previous Workers

The results of the analysis of the Owens Valley data have shown that the A, B and C rings have very low brightness temperatures that are roughly comparable. An analysis of the results for the brightness temperature of the region of the planet that is blocked by the rings shows that their optical depths are approximately the same as those estimated for the rings at visible wavelengths. The results of the analysis of the Hat Creek observations are in good agreement with those of the Owens Valley observations and indicate that the rings probably have the same brightness temperature

(relative to the planet) and optical depth at 1.30 cm that they do at 3.71 cm. These conclusions are in good qualitative agreement with the results of the interferometric observations made by others. There are, however, some quantitative differences which must be examined carefully.

No other observers have attempted to isolate and detect emission from the C ring or the effects of its opacity on the emission from the planet. In addidion, the Hat Creek observations were, apparently, not sensitive enough to detect the C ring. Thus, only the results of the models without the C ring will be compared to the results of others. Although it has been shown that the absence of the C ring in the models does not strongly affect the Owens Valley results, some caution should be observed when considering the results of other observations since its effects are unknown in those cases and may be significant, particularly when observations are made on only a couple of baselines. The possible effects of limb-darkening should also be considered when comparing the results with those of others, particularly those at other wavelengths. Limb-darkening did not appear to affect the Hat Creek results, and it was not detectable in the Owens Valley data. However, its effects on the model fitting results may be significant at other wavelengths.

The only other detection of the rings at 3.71 cm has been made by Cuzzi and Dent (1975) using the 3 element NRAO interferometer at spacings of 100 m, 1800 m and 1900 m. Briggs (1974) made observations earlier with the same instrument, but was only able to place an upper

limit of 20 K on the ring brightness temperature and report that the optical depth of the B ring was comparable to its visible optical depth. Cuzzi and Dent derived a B ring brightness temperature of 15 ± 3 K assuming a model in which the rings are uniformly bright and the A ring has a brightness temperature that is 40% of the B ring. The optical depth of the B ring was found to be 0.8 ± 0.1 and the total flux from Saturn was consistent with a disk temperature of 161 ± 5 K. This disk temperature and the opacity of the B ring may be used to derive an unblocked planet brightness temperature of 174 K. If the A and B ring brightness temperatures are combined according to their relative areas at the time of the observations, then the combined, uniformly bright, A and B ring brightness temperature is 11 K.

In order to make a comparison of the results of Cuzzi and Dent with those of Owens Valley Model 1, it is appropriate to normalize the brightness temperature of the rings by the brightness temperature of the unblocked portion of the planet. Although the flux calibrations should be consistent, since both data sets assume a flux of 2.7 f.u. for 3C138, it is possible for systematic errors to enter through the use of secondary calibrators. For this reason, the parameter that is probably best determined by an interferometer is the ratio of the ring brightness temperature and planet brightness temperature. Cuzzi and Dent's results imply a normalized ring brightness temperature of 0.063 ± 0.017. This result is formally different from the Owens Valley Model 1 result of the 1973-1974 data set, 0.031 ± 0.007, but it is not

formally different from the 1976 result of 0.043 ± 0.007. Since it is believed that the 1973-1974 and 1976 results are not significantly different, they may be combined to yield a result of 0.04 ± 0.01 which is not formally different from the result of Cuzzi and Dent. Thus, the results of Model 1 and Cuzzi and Dent are in fair agreement.

Although these results are in fair agreement, the results of Cuzzi and Dent are higher by a large, if not formally significant, amount. It is interesting, therefore, that the results of Cuzzi and Dent can be brought into better agreement by considering only the ring brightness temperature that they determined on their short, 100 m, baseline. This baseline gave a B ring brightness temperature result of 12.5 ± 3 K which was substantially lower than the result from the longer baselines which was 17.5 ± 2 K. If a normalized, combined A and B ring brightness temperature is derived for the short baseline data, then its value of 0.052 ± 0.017 is in much better agreement with the Owens Valley data than is the result obtained from all the baselines. This better agreement between the results may be closer to the truth and due to the manner in which Cuzzi and Dent fit their model to their data. Their method consists of a brute force fitting of the data to a single parameter, which is essentially the ratio of the ring to planet brightness. This method ignores the possible correlation between the brightness temperature of the rings and the brightness temperature of the blocked region which, on long baselines, is expected to be an important parameter. On short baselines, how-

ever, the blocked region has little effect on the solution for the ring brightness temperature (Janssen and Olsen, 1977). Thus, one might expect the short baseline result to be closer to the true value since it should be least affected by correlation with the blocked region of the planet.

The B ring optical depth determined by Cuzzi and Dent is in good agreement with the optical depth of Owens Valley Model 1. Both results are consistent with the optical depth of the B ring that is estimated at visible wavelengths. It is possible, however, that the microwave results are slightly in error as a result of the assumptions made to compute them. If there were a large, undetected asymmetry in the brightness of the rings, for example, then their brightness temperature in front of the planet might differ from that determined by a model fit to uniformly bright rings. The optical depth, then, would be incorrectly estimated since the amount of radiation attributed to the rings in front of the planet would be in error. The optical depths are not seriously affected, however, since an underestimate of their brightness temperature in front of the planet by a factor of 3 causes the B ring optical depth to be underestimated by only 50%. Similarly, if there is no radiation from the rings where they cross the planet, then the optical depths are overestimated by about 20%. Another factor, which could cause the optical thickness of the rings to be underestimated, is the neglect of the Cassini division. Since the Cassini division is less optically thick than the rings, it should not attenuate the planetary emission

incident upon it as much as the rings and more radiation will penetrate them where they block the planet. The extra radiation will probably cause the ring optical depths to be underestimated, although the amount of underestimation is difficult to determine and extremely model dependent. If, however, the optical thickness of the division is taken to be 0, then the optical thickness of the rings might be underestimated by about 25%. Thus, the estimated optical depths may be affected by the assumptions employed to compute them. However, the errors introduced by incorrect assumptions are not likely to be greater than 50% and are probably much less. Thus, while it is unlikely that the 3.71 cm optical depth is much less than the visible optical depth, it may turn out to be somewhat greater.

Other interferometric observations in which emission from the rings is detected, have recently been reported by Jaffe (1977) at 6 cm and Janssen and Olsen (1977) at 8 mm. Jaffe reports observations made with the Westerbork Synthesis Telescope and his results indicate a B ring brightness temperature of 7 ± 1 K and an A ring brightness temperature of 4 ± 1 K. The brightness temperature of the unblocked region of the planet is 176 ± 2 K and the estimate of the B ring optical depth is 0.4 ± 0.1. Janssen and Olsen (1977) made observations with the new Table Mountain millimeter-wave interferometer and obtained an unblocked planet brightness temperature of 144 ± 4 K and a combined A and B ring brightness temperature of 12.7 ± 2.0 K. They were unable to estimate the ring optical depth because of the limited resolution of the interferometer.

The ring brightness temperature result of Jaffe (1977), when the A and B ring results are combined into a single ring and normalized by the brightness temperature of the unblocked planet, is 0.034 ± 0.006. This is consistent with the Hat Creek and Owens Valley results and indicates that the rings do not vary in brightness temperature between 1.30 and 6 cm by more than about 1 percent of the brightness temperature of the planet. The result of Janssen and Olsen (1977), however, may indicate a significant increase in the brightness temperature of the rings relative to that of the disk at shorter wavelengths. Their result of 0.088 ± 0.014 is significantly different from all of the centimeter wave results except that of Cuzzi and Dent (1975). The result is quite different from the Hat Creek Model 1 result of 0.040 ± 0.008, and if this difference is real, it places severe constraints upon physical models of the rings.

The B ring optical depth obtained by Jaffe (1977) at 6 cm is formally significantly different from those of the Owens Valley and Cuzzi and Dent at 3.71 cm. Jaffe (1977) cautiously interprets this difference as a real effect but points out that the determination is very dependent upon the choice of planetary radii. His choice is unfortunate because it does not allow for the effect of the viewing geometry. Thus, the polar radius is chosen by Jaffe to be the true polar radius when it is actually expected to be about 2% larger at the time of his observations. This effect has been included in the Owens Valley models and those of Cuzzi and Dent and makes comparison

between their results and the results of Jaffe difficult. A consideration of the effect in the Owens Valley data has shown that, if it is not included, then the estimate of the optical depth is lowered by about 0.2. Thus, about all that can be fairly said is that the difference between the optical depth at 3.71 cm and at 6 cm, if it exists at all, is probably not as large as the formal results indicate.

Many other observations of Saturn and the rings have been made but are difficult to compare to the present results. The upper limits on the ring brightness temperature that were set by Berge and Read (1968), Berge and Muhleman (1973), and Briggs (1974) are all consistent with the Owens Valley and Hat Creek results and indicate that the ring brightness temperature remains at least as low as the 3.71 cm value out to 21 cm wavelength. The results of Briggs (1974), like those of Jaffe (1977), indicate that the B ring optical thickness may decrease with wavelength, although this conclusion is by no means certain. At wavelengths shorter than 8 mm, no interferometric observations have been made and, therefore, estimates of the ring brightness must be made from single dish observations that do not resolve the ring system. These estimates, with the exception of that of Rather et al. (1974) at 1 mm, show no sign of the rings. More recent observations of Saturn at 1 mm made by Elias et al. suggest that Rather et al's. result may be incorrect and provide a crude upper limit of about 50 K for the brightness temperature of the rings (Janssen and Olsen, 1977). At present, all that may reasonably be said is that

the rings remain far below their infrared brightness temperature at millimeter wavelengths. However, in view of the result of Janssen and Olsen, their millimeter wave brightness temperature may exceed that of centimeter wavelengths.

d) Comparison of Microwave Observations with Simple Ring Models

(i) The Microwave Spectrum of the Rings

The brightness temperatures of the rings determined by this study and others are summarized in Figure 33. The figure shows the brightness temperature of the combined A and B rings normalized by the brightness temperature of the planet and plotted against the wavelength of observation. This is a natural way to view the microwave spectrum of the rings for two reasons. First, it is a relative measurement and is, therefore, not affected by errors in the absolute calibration of the data. Such errors make the comparison of observations made at different wavelengths extremely difficult. Second, the brightness temperatures of the rings and planet are intimately related since the radiation from the rings is primarily radiation that was thermally emitted by the planet and scattered to the earth by the ring particles. Thus, their ratio will remain constant as long as the particles' scattering properties do not change. Most of the observations indicate that, in fact, the ratio has a value of about 0.04 which does not change over the range of wavelengths observed. These values can be almost entirely explained by the scattered planetary radiation, and apparently

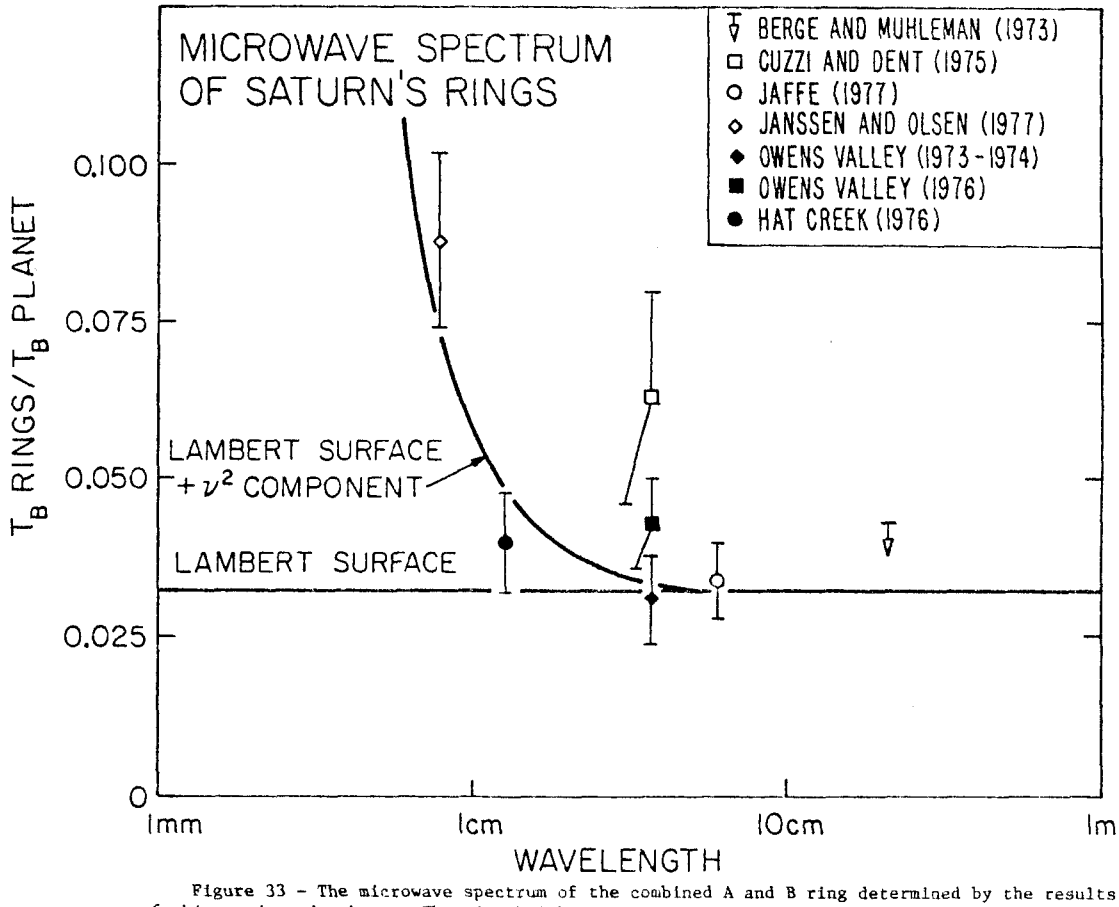

Figure 33 - The microwave spectrum of the combined A and B ring determined by the results of this study and others. The ring brightness temperature is shown normalized by the brightness temperature of the unblocked portion of the planet to remove any errors due to the absolute calibration of the observations. The curves shown in the figure represent the amount of radiation due to reflection of the planetary emission off of a Lambert surface at the position of the rings and that due to reflection plus a component that is proportional to the frequency squared. The frequency squared component is meant to approximate the radiation due to thermal emission from the rings.

no thermal emission is required to explain most of the microwave spectrum. A notable exception to this statement is the measurement of Janssen and Olsen (1977) at 8 mm wavelength which is not consistent with the centimeter wave measurements and may indicate the presence of some thermal emission from the rings.

The simplest scattering model which may be used to compare the observed radiation from the rings with that expected due to scattered planetary emission is that of a Lambert surface. The Lambert surface is known to be a good approximation to both diffuse scattering from clouds and from very rough planetary surfaces. The diffuse scattering from a many-particle-thick layer is like diffuse scattering from a cloud where the ring particles take the place of the cloud particles. The scattering from a monolayer of particles may be likened to that from a rough planetary surface since the ring particles are quite close together and would shadow one another to some extent. Therefore, the Lambert surface is an appropriate model to use for both the many-particle-thick and single-particle-thick ring models. Scattering calculations for a many-particle-thick layer of conservative isotropic scatters, which shall be discussed later, show that the Lambert surface is an adequate representation of diffuse scattering from such a layer. Unfortunately, the problem of diffuse scattering from a monolayer of particles is not well understood, and it is not possible to check the Lambert surface approximation of it.

The average brightness temperature, normalized by the planetary brightness temperature, of a conservative Lambert surface in the position of the A and B rings is shown in Figure 33 along with the microwave observations. The Lambert surface model provides a satisfactory fit to most of the observations at the Hat Creek wavelength of 1.30 cm and longer. The simplest explanation of the observations, then is that the radiation from the rings at these wavelengths is nearly all scattered planetary thermal emission., and that the ring particles themselves are nearly conservative scatterers at centimeter wavelengths.

The observation of Janssen and Olsen (1977) may indicate that a profound change in the brightness of the rings occurs just shortward of the 1.30 cm Hat Creek observations. The extra ring brightness indicated by this result, if it is real, is probably due to thermal emission from the ring particles. An alternate explanation of this increase in the ring brightness is that it is due to millimeter sized particles which did not scatter efficiently at centimeter wavelengths but begin to be seen at 8 mm wavelengths. The explanation is probably not the correct one since, if it were true, the centimeter wavelength optical depths would be lower than the visible wavelength optical depths. However, the microwave optical depths are nearly the same as the visible, and in addition, consideration of a many-particle thick layer of isotropic scatters has shown that it is

not possible to simply increase the optical depth of the layer and achieve the ring brightness temperature measured by Janssen and Olsen (1977). Thus, the most likely explanation of their value, if it is correct, is that it is due to thermal emission from the ring particles.

In order to see whether the thermal emission that is required by the measurement of Janssen and Olsen is compatible with the other microwave observations, another model is considered. In this model, a component of ring radiation which is proportional to the square of the frequency has been added to the amount that is expected from diffuse scattering from a Lambert surface. The frequency squared dependence may be appropriate for the rings since the absorption coefficient of ice is probably proportional to the square of the frequency (Whalley and Labbé, 1969). Thus, following the reasoning of Janssen and Olsen (1977), the thermal emission from a slab of ice will increase as the frequency squared. This dependence may also be the case for a many-particle-thick layer of particles since each particle may be viewed as a "slab" with thermal emission that is proportional to frequency squared.

A model with a frequency squared component is shown in Figure 33. The particular model of the normalized ring brightness temperature, T_R, is given by

$$T_R = T_L + T_T(\nu/23)^2$$

where T_L is the brightness expected for a conservative Lambert

surface, T_T is the component due to thermal emission, and ν is the frequency in GHz. For the model shown in the figure, T_T is chosen so that the model ring brightness at 1.30 cm is equal to the nominal Hat Creek value plus one standard deviation. It is seen from the figure that such a model just nicks the lower end of the error bar of the point of Janssen and Olsen and that, therefore, the model can be made to be consistent with all of the data. However, the fact that two points, the Hat Creek and Janssen and Olsen points, can be made consistent with a two parameter model does not support the observations made or indicate that the model is correct. In fact, as pointed out by Janssen and Olsen (1977), this simple model cannot explain all millimeter-wave observations since, if it is extrapolated to shorter wavelengths, the rings would reach their infrared brightness temperature at a wavelength of about 2 mm. Since the upper limits to the ring brightness temperature at 1 mm are far lower than this, it is clear that the behavior of the rings is more complicated than one might predict, if the observation of Janssen and Olsen (1977) is correct.

At the present time, more complicated models of the rings are not called for since the observations that require them are difficult to make and may be misleading. What is called for are further measurements of the millimeter radiation from the rings to confirm the increase in their emission that is indicated by the value of Janssen and Olsen.

(ii) The Optical Thickness and Brightness Temperature of the Rings

In the previous section, it was stated that most of the centimeter wave ring brightness temperature could be explained by planetary thermal emission that is scattered to the earth by the ring particles. In this section, this statement is examined more carefully in the context of simple physical models of the rings. The two physical models which must be considered are the many-particle-thick ring and the single-particle-thick ring. It must be remembered that an intermediate case may also be permitted.

The calculation of the diffusely scattered and thermally emitted radiation from a many-particle-thick ring is straightforward, since it employs the standard radiative transfer techniques of Chandrasekhar (1960). In particular, for this study the single scattering phase function of the ring particles is assumed to be isotropic, and Chandrasekhar's (1960) X and Y functions, which have been computed by Carlstadt and Mullikin (1966), are used to compute the intensity of the diffusely scattered planetary radiation from the rings. The amount of thermally emitted radiation from such a layer is also computed using the X and Y functions and may be derived by following the reasoning of Goody (1964) for the semi-infinite case.

The brightness temperature of a many-particle-thick ring of isotropic scatterers is a function of two physical parameters: the optical thickness of the rings and the single scattering albedo of the particles. Since the interferometric observations measure

both the ring brightness temperature and optical thickness, the physical model may be used to estimate the single scattering albedo of the particles. The single scattering albedo, $\tilde{\omega}_o$, is a useful property of a particle and is defined to be the ratio of the particle's scattering cross section to its extinction cross section, which includes both scattering and absorption.

The results of the calculations for the many-particle-thick ring model are shown in Figure 34. The brightness temperature of each of the three rings is plotted as a function of their optical thickness for two cases in which the single scattering albedos are 0.95 and 1.00. The brightness temperature and optical thickness results of the Owens Valley observations are also shown on the figure. The brightness temperatures that are plotted represent the weighted average of the 1973-1974 and 1976 Model 4 results. The optical thicknesses shown are not the formal solutions, but are likely values based upon the formal solutions from the models with and without the C ring. These values are summarized in Table 18. The B ring results of Cuzzi and Dent (1975) and Jaffe (1977) are also shown in the figure for comparison.

The many-particle-thick models compare favorably with the observations. All observations shown, except that of Cuzzi and Dent (1975) are consistent with conservative scattering ($\tilde{\omega}_o$=1) although the best fitting value of $\tilde{\omega}_o$ would probably lie between 0.95 and 1.00. Since the observations of all three rings are consistent with the same range of single scattering albedo, it is

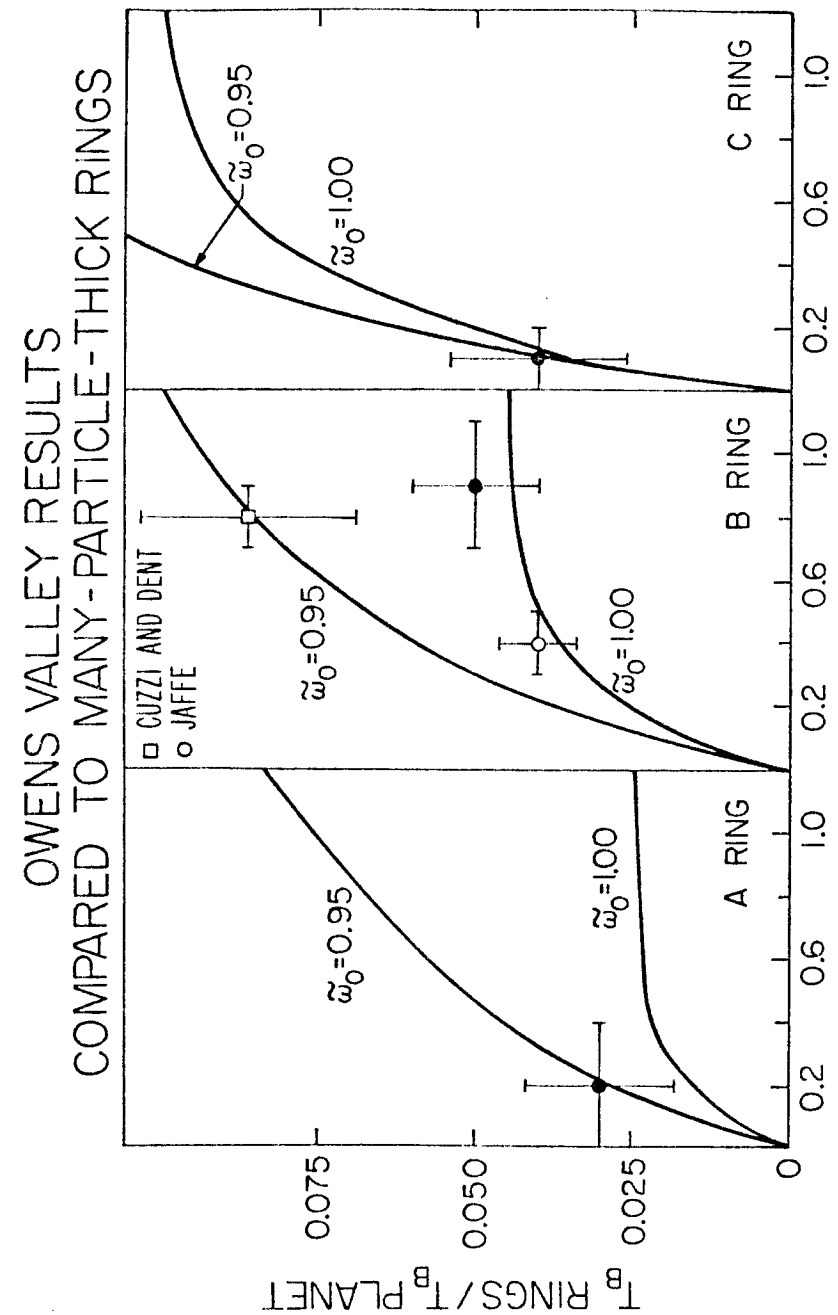

Figure 34 - Comparison of the OVRO ring brightness temperature and optical thickness results (filled points) with model of the rings as a many-particle-thick layer of isotropically scattering particles. The B ring results of Jaffe (1977) and Cuzzi and Dent (1975) are shown for comparison.

TABLE 18

SUMMARY OF FINAL OWENS VALLEY (3.71 cm)

RESULTS FOR INDIVIDUAL RINGS

Ring	$\frac{T_B \text{ Ring}^*}{T_B \text{ Planet}}$	Optical Depth †
A Ring	0.030 ± 0.012	0.2 ± 0.2
B Ring	0.050 ± 0.010	0.9 ± 0.2
C Ring	0.040 ± 0.014	0.1 ± 0.1

* Brightness temperatures are weighted averages of the 1973-1974 and 1976 Model 4 results.

† Optical depths are not formal results but estimates based upon the formal results of fits to models with and without the C ring.

possible that the same kind of particle is present in all three rings. If this assumption is made, then the B ring values allow the best estimate of $\tilde{\omega}_o$ to be made, and this value would be very close to 1, if the observation of Cuzzi and Dent is ignored. The Owens Valley observations, then, are consistent with a many-particle-thick layer of particles which are nearly conservative scatterers. Since the optical thickness and ring brightness temperature of the Hat Creek observations are nearly the same as those of the Owens Valley observations, they are probably consistent with the same model, and it is likely that the particles are nearly conservative at all centimeter wavelengths. At 8 millimeters wavelength, if the observation of Janssen and Olsen is correct, the particles cannot be conservative. Within the context of the many-particle-thick model, a single scattering albedo of about 0.92 is required to explain the result of Janssen and Olsen. Thus, only a small change in the single scattering albedo is required to explain the result of Janssen and Olsen, and the ring particles probably remain excellent scatterers.

In addition to being consistent with the observations of the rings' optical thickness and brightness temperature, the many-particle-thick model is also consistent with the lack of a strong dependence of the ring brightness temperature on the ring tilt angle. The tilt angle dependence of some of the ring models is shown in Figure 35 along with the Hat Creek and Owens Valley observations. The Owens Valley results are those of Model 3, in which the A and

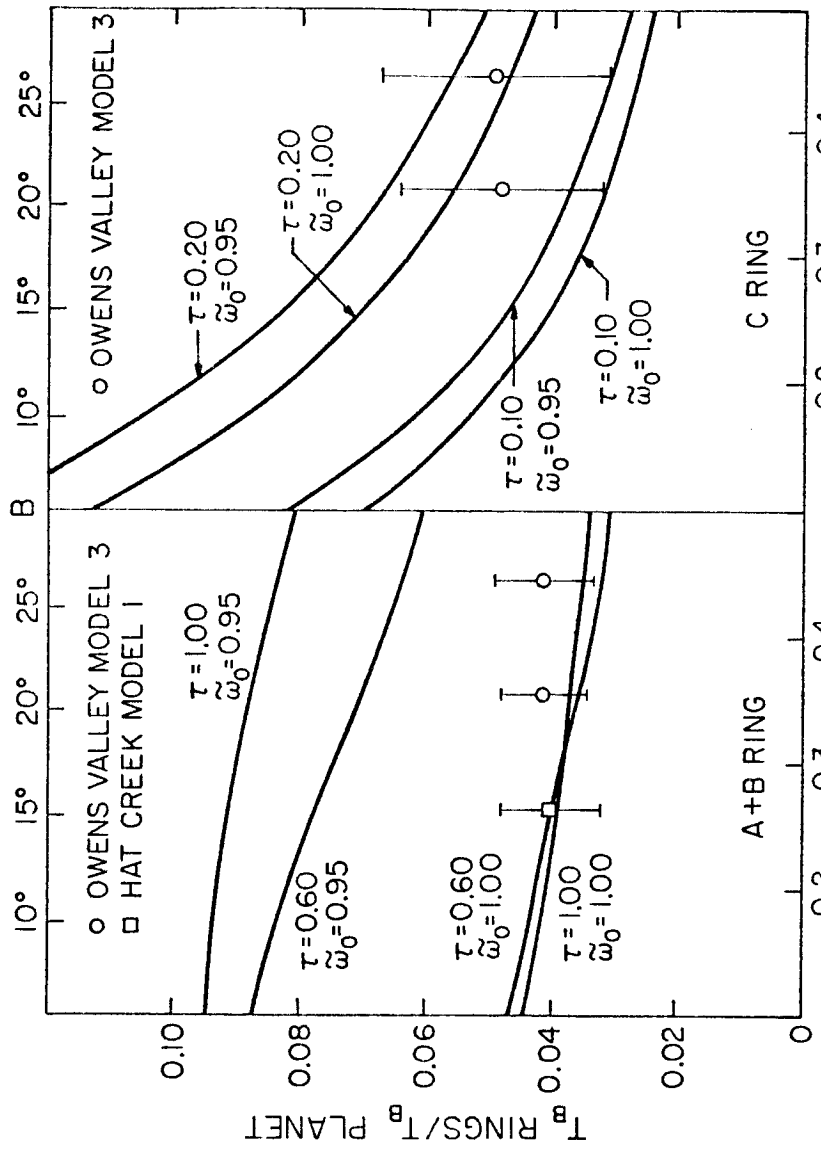

Figure 35 - Comparison of the tilt angle dependence of the many-particle-thick model with the Owens Valley and Hat Creek observations. The OVRO values plotted are those of Model 3 which combines the A and B rings into a single ring to improve the determination of its brightness temperature. The Hat Creek Model 1 value is also shown since it seems to be consistent with the Owens Valley value, although it may contain a hidden wavelength dependence.

B ring are combined into a single ring to improve the determination of their brightness temperature. The Hat Creek value is the result of Model 1 and is included since the Hat Creek and Owens Valley results seem to be consistent with one another. As has been stated previously, however, it is possible that the Hat Creek value shown in the figure is affected by a wavelength dependence as well as a tilt angle dependence. It is clear from the figure that the variations in the ring brightness temperature which are predicted by the many-particle-thick model are not large enough to be detected by the microwave observations. However, in the coming years, as the tilt angle of the rings decreases, it may be possible to detect a change in the brightness temperature of the C ring if the many-particle-thick model is the correct one. Microwave observations should continue to be made in order to determine whether such effects exist.

The agreement between the simple many-particle-thick model and the observations is interesting. However,it is obvious that it is not the only model which can be made to fit the observations. It is possible that collisions between the ring particles have caused the rings to spread out radially until they are only one particle thick. Therefore, the diffusely scattered and thermally emitted radiation from a single-particle-thick ring will now be estimated and compared to the observations.

An estimate of the expected amounts of this radiation is difficult, since there is no good theory of diffuse scattering and thermal emission from a monolayer of particles. For the purpose of the present discussion, the single-particle-thick layer will be approximated by a Lambert surface. A Lambert surface may be expected to be a reasonable approximation of a monolayer since it is known to be an adequate representation of a rough surface. If the ring particles are fairly close together, as they must be to satisfy the available information on their optical thickness, then an approximation of them as a rough surface may not be inappropriate. Unfortunately, the model is not a very physical one and is not easily used to make inferences about the ring particles. However, it does serve to illustrate that a model of the rings that is only one particle thick is probably capable of explaining the microwave observations.

The solution for diffuse scattering of radiation by a Lambert surface is well known. The surface which represents the rings is allowed to have an albedo, A, and a fraction of its total area, f, which is permitted to scatter and attenuate incident radiation. The diffusely scattered radiation, then, comes from a Lambert surface with an effective albedo, A_{EFF}:

$$A_{EFF} = A\ f \quad .$$

If the albedo of the Lambert surface is not equal to 1, then it is also expected to emit thermal radiation. The thermal radiation

that is emitted is isotropic and given by the surface's temperature times an effective emissivity, ε_{EFF}, which is given by

$$\varepsilon_{EFF} = f(1 - A).$$

Thus, the total intensity of the radiation from this ring model is given by the sum of the scattered and emitted radiation, and it is a function of the surface albedo, A, and the fraction filled with particles, f.

The ring brightness temperature of the Lambert surface model for each of the three rings is plotted in Figure 36 as a function of the filling factor, f. Three different curves, representing the surface albedos of 0.8, 0.9, and 1.0, are shown for comparison to the observations. The Owens Valley observations measure the ring brightness temperature and the filling factor. The latter is estimated by measuring the ratio of the brightness temperatures of the region of the planet that is blocked by the rings and the remaining, unobscured portion of the planet. The values of this parameter that were estimated from the Owens Valley data were highly dependent upon whether the C ring was included in the model. Thus, since the results with the C ring were inconsistent with those without the C ring, a box which contains the range of values consistent with both models is shown in the figure for comparison to the models.

The surface albedo of the Lambert surface may be estimated from the graph in Figure 36 in the same way that the particle

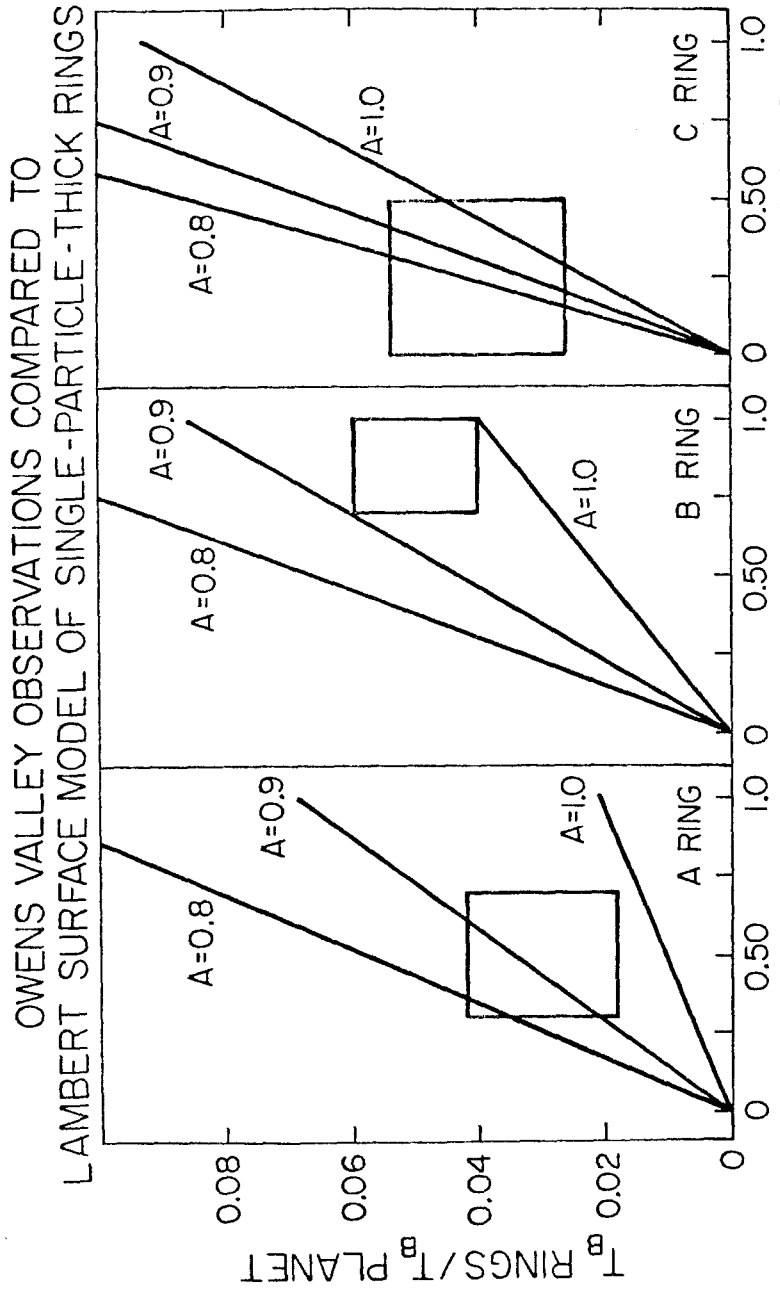

Figure 36 - Comparison of the Lambert surface model of single-particle-thick rings with the Owens Valley results. The determination of the fraction of the rings' surface filled with particles was very dependent upon whether the C ring was included in the model fit. Since consistent results were not obtained, the most probable values of the ring brightness temperature and fraction of the surface filled with particles are shown as a box

single scattering albedo was estimated from Figure 33. The surface albedo, unfortunately, is difficult to interpret in terms of the scattering properties of the ring particles. However, it must be closely related to the particle's single scattering albedo since the Lambert surface model is meant to represent a single layer of particles. The figure shows that this simple model can be made consistent with the observations if its surface albedo is between 0.8 and 1.0. This value is quite high and probably indicates that the ring particles have a fairly high single scattering albedo. It is also apparent that the model is in agreement with the observations of the ring brightness temperature at different tilt angles, since a Lambert surface appears equally bright at all angles of incidence. Thus, to the extent that a single-particle-thick layer can be modeled by a Lambert surface, the observations are consistent with a monolayer of particles with a fairly high single scattering albedo.

(iii) The Radar Cross Section of the Rings

The two models which have been compared to the observations are extremely simple ones. In spite of this, they are capable of explaining the microwave observations presented here and those of other observers as well. It is interesting, therefore, to see whether they are capable of explaining the radar cross section of the rings as well. The radar cross section is the ratio of the total power returned by the rings to that expected from an isotropically scattering surface of the same size. It has been measured to

be 1.37 ± 0.16 (Goldstein et al., 1976) at 3.5 cm wavelength and is the same at 12.6 cm. The radar echo was also observed to be almost completely depolarized by the rings.

The radar results are easy to compare with the Lambert surface model. The observed radar cross section may be expained by a Lambert surface with an effective albedo, A_{EFF}, of 0.78 (Cuzzi and Pollack, 1977). If the A ring is taken to have a filling fraction, f, of one-half and the B ring has f equal to 1, then the Lambert surface model can be made to agree with the radar cross section if its surface albedo is 1. Further, since a Lambert surface totally depolarizes all reflected radiation, the polarization results will be satisfied as well. Thus, it is possible to stretch this ad hoc model to the limit of its believability and satisfy the available observations. Unfortunately, since the model is not a physical one, it yields little useful information about the ring particles.

The many-particle-thick layer of isotropic scatterers cannot be made to agree with the radar observations unless the optical thickness of the rings is greatly increased. The average optical thickness of the A and B rings at centimeter wavelengths is probably about 0.6, and if this value is used to compute their radar cross section, using the X and Y functions, then a value of only 0.87 results. This value is fairly high, but is not in agreement with the observations. In order to make the simple model agree with the ob-

served radar cross section, the optical thickness of the rings is required to be about 2.5. This optical thickness is totally inconsistent with the microwave observations, and therefore, the model of the rings as a many-particle-thick layer of isotropic scatterers cannot satisfy the radar data. Thus, if the many-particle-thick layer is the correct model of the rings, the particles are required to scatter anisotropically.

e) Conclusions and Suggestions for Future Work

At the present time, the most likely explanation of the microwave results continues to be that the particles are large and composed of water ice. The particles are probably very large compared to the microwave wavelengths, although sizes which are more comparable to the wavelength may not be ruled out. Particles which are meter sized or larger provide the simplest explanation of the similarity between the microwave and visible wavelength optical depths of the rings and the wavelength independence of the radar cross section. The large particles, implied by the radar and optical depth measurements, and their high single scattering albedos, implied by the microwave brightness temperature of the rings, mean that they are composed of either a highly transparent or highly reflective material. Since water ice has been detected in the rings and is known to be highly transparent at microwave wavelengths, it remains the most likely ring material. However, as pointed out by Janssen and Olsen (1977), meter sized

particles of water ice may be inconsistent with the apparently low ring brightness temperatures at millimeter wavelengths. Eventually, this fact may be used to rule out water ice as the main component of the rings, although at this time it may simply indicate that the absorption properties of ice at low temperatures and microwave wavelengths are poorly known.

It is evident that much work remains to be done before the full implications of the radar and microwave observations of Saturn's rings are known. One of the most obvious things that needs to be done is to develop a good theory for diffuse scattering from a monolayer of particles, since this is the most likely configuration of the rings based on studies of their dynamics. It will also be important to continue to investigate the many-particle-thick models and see whether particles with anisotropic phase functions can be made to satisfy the radar and microwave observations. Observational work will continue to be important and should provide more constraints for the physical models of the rings. Millimeter wave observations should be made to determine whether the rings emit thermal radiation, as suggested by the observation of Janssen and Olsen (1977), and observations should also be made to see whether the centimeter-wave properties of the rings remain the same at longer wavelengths. In addition to extending the observational work to different wavelengths, it will also be important to continue to observe the rings at centimeter wavelengths to see whether the

brightness temperature of the rings changes as the tilt angle of the rings decreases. Thus, the rings of Saturn will continue to be interesting objects to radio astronomers for several years to come. It will also be important for them to be studied by radio techniques since the observations probably provide the best constraints on models of the particles' size and bulk composition.

REFERENCES

Alexander, A.F.O'D. (1962). The Planet Saturn. (London, Faber and Faber) 474 p.

Altschuler, D.R. and Wardle, J.F.C. (1976). Observations of the flux density and linear polarization of compact extragalactic radio sources at 3.7- and 11.1- cm wavelength. Mem. R. astr. Soc. 82, 1-67.

American Ephemeris and Nautical Almanac (1973-1976). U.S. Government Printing Office, Washington, D.C.

Berge, G.L. and Gulkis, S. (1976). Earth-based radio observations of Jupiter: Millimeter to meter wavelengths. In Jupiter (T. Gehrels, Ed.) Univ. of Arizona Press, Tucson, pp. 621-692.

Berge, G.L. and Muhleman, D.O. (1973). High-Angular-Resolution observations of Saturn at 21.1-centimeter wavelength. Astrophys. J. 185, 373-381.

Berge, G.L. and Read, R.B. (1968). The microwave emission of Saturn. Astrophys. J. 152, 755-764.

Blake, G.M. (1970). Observations of extragalactic radio sources having unusual spectra. Astrophys. Lett. 6, 201-205.

Brahic, A. (1977). Systems of colliding bodies in a gravitational field. I - Numerical simulation of the standard model. Astron. Astrophys. 54, 895-907.

Briggs, F.H. (1974). The microwave properties of Saturn's rings. Astrophys. J. 189, 367-377.

Brouw, W.N. (1975). Aperture Synthesis. In Methods in Computational Physics, V. 14, (Alder, B., Fernback, S., Rotenberg, M., eds.) Academic Press, New York, pp. 131-175.

Carlstadt, J.L. and Mullikin, R.W. (1966). Chandrasekhar's X- and Y- functions, Ap. J. Suppl. 12, 449.

Chandrasekhar, S. (1960). Radiative Transfer. Dover Publications, New York, 393 p.

Cohen, M.H. (1972). Accurate positions for radio sources. Astrophysical Letters 12, 81-85.

Cook, A.F., Franklin, F.A. and Palluconi, F.D. (1973). Saturn's rings-A survey. Icarus 18, 317-337.

Couper, H.A. (1972). Precise optical positions of nine compact radio sources. Astrophysical Letters 10, 121-124.

Cuzzi, J.N. and Dent, W.A. (1975). Saturn's rings: The determination of their brightness temperature and opacity at centimeter wavelengths. Ap. J. 198, 223-227.

Cuzzi, J.N. and Pollack, J.B. (1977). Saturn's rings: Particle composition and size distribution as constrained by microwave observations. I: Radar observations. Submitted to Icarus, now in press.

Cuzzi, J.N. and Van Blerkom, D. (1974). Microwave brightness of Saturn's rings. Icarus 22, 149-158.

Dent, W.A., Aller, H.D. and Olsen, E.T. (1974). The evolution of radio spectrum of Cassiopeia A. Astrophys. J. Letters 188, L11-L13.

Elias, J.H., Ennis, D.J., Gezari, D.Y., Hauser, M.G., Houck, J.R., Lo, K.Y., Matthews, K., Nadeau, D., Neugebauer, G., Werner, M.W., and Westbrook, W.E. 1 mm continuum observations of extragalactic objects. Submitted to Astrophysical Journal.

Esposito, L.W. and Lumme, K. (1977). The tilt effect for Saturn's rings. Icarus 31, 157-167.

Fomalont, E.B. and Wright, M.C.H. (1974). Interferometry and aperture synthesis. In Galactic and Extra Galactic Radio Astronomy (Verschuur, G.L. and Kellermann, K.I., eds.) Springer-Verlag, New York, 256-290.

Goldreich, P. and Tremaine, S. (1977). The velocity dispersion in Saturn's rings. Submitted to Icarus.

Goldstein, R.M. and Morris, G.A. (1973). Radar observations of the rings of Saturn. Icarus 20, 260-262.

Goldstein, R.M., Green, R.R., Pettengill, G.H. and Campbell, D.B. (1976). The rings of Saturn: Two-frequency radar observations. Icarus 30, 104-110.

Goody, R. (1964). Limb-darkening of thermal emission from Venus. Icarus 3, 98-102.

Gulkis, S. and Poynter, R. (1972). Thermal radio emission from Jupiter and Saturn. Phys. Earth Planet. Interiors 6, 36-43.

Hinder, R. and Ryle, M. (1971). Atmospheric limitations to the angular resolution of aperture synthesis radio telescopes. Mon. Not. R. astr. Soc. 154, 229-253.

Högbom, J.A. (1974). Aperture synthesis with a non-regular distribution of interferometer baselines. Astron. Astrophysl. Suppl. 15, 417-426.

Jaffe, W.J. (1977). 6cm radio observation of Saturn. Submitted to the Astrophysical Journal.

Janssen, M.A. (1974). Short wavelength radio observations of Saturn's rings. In The Rings of Saturn (F.D. Palluconi and G.H. Pettengill, eds.) pp. 83-96. NASA SP 343.

Janssen, M.A., Golden, L.M. and Welch, W.J. (1974). Extension of the absolute flux density scale to 22.285 GHz. Astron. and Astrophys. 33, 373-377.

Janssen, M.A. and Olsen, E.T. (1977). A measurement of the brightness temperature of Saturn's rings at 8 mm wavelength. Submitted to Icarus.

Kawata, Y. and Irvine, W.M. (1974). Models of Saturn's rings which satisfy the optical observations. In The Exploration of the Planetary System (Woszczyk and Iwaniszewska, eds.), IAU Symp. 65, D. Reidel Publishing Co., Dordrecht, Holland, pp. 441-464.

Kellermann, K.I. and Pauliny-Toth, I.I.K. (1973). Measurements of the flux density and spectra of discrete radio sources at centimeter wavelengths. IV. The observations at 10.7 GHz (2.8 cm). Astronomical Journal 78, 828-847.

Lumme, K. and Irvine, W.M. (1977). Low tilt angle photometry and the thickness of Saturn's ring. Bull. Amer. Astron. Soc. 9, 521, (abstract).

Muhleman, D.O., Schloerb, F.P. and Berge, G.L. (1976). A radio synthesis map of the Saturn system at a wavelength of 3.71 cm. Bull. Amer. Astron. Soc. 8, 475, (abstract).

Newburn, R.L., Jr. and Gulkis, S. (1973). A survey of the outer planets Jupiter, Saturn, Uranus, Neptune, Pluto and their satellites. Space Science Reviews 14, 179-271.

Pauliny-Toth, I.I.K. and Kellermann, K.I. (1968). Measurements of the flux density and spectra of discrete radio sources at centimeter wavelengths. II. The observations at 5 GHz (6 cm). Astronomical Journal 73, 953-969.

Pilcher, C.B., Chapman, C.R., Lebofsky, L.A., and Kieffer, H.H. (1970). Saturn's rings: Identification of water frost. Science 167: 1372-1373.

Pollack, J.B. (1975). The rings of Saturn. Space Science Reviews 18, 3-93.

Rather, J.D.G., Ulich, B.L., and Ade, P.A.R. (1974). Planetary brightness temperature measurements at 1.4 mm wavelength. Icarus 22, 448-453.

Rieke, G.H. (1975). The thermal radiation of Saturn and its rings. Icarus 26, 37-44.

Smith, J.W. (1970). Precise positions of twenty-eight radio sources. Nature PS 232, 150-152.

Welch, W.J., Forster, J.R., Dreher, J., Hoffman, W., Thornton, D.D., and Wright, M.C.H. (1977). An interferometer for millimeter wavelengths. Astron. Astrophys. 59, 379-385.

Whalley, E. and Labbé, H.J. (1969). Optical spectra of orientationally disordered crystals. III. Infrared spectra of soundwaves. J. Chem. Phys. 51, 3120-3127.